RICE UNIVERSITY

Electrical and Optical Characterization of Molecular Nanojunctions
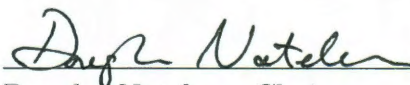
by

Daniel R. Ward

A THESIS SUBMITTED
IN PARTIAL FULFILLMENT OF THE
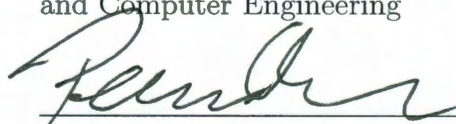REQUIREMENTS FOR THE DEGREE

Doctor of Philosophy

APPROVED, THESIS COMMITTEE:

Douglas Natelson, Chair
Professor of Physics and Astronomy

Naomi J. Halas
Stanley C. Moore Professor of Electrical
and Computer Engineering

Peter Nordlander
Professor of Physics and Astronomy

Houston, Texas

September, 2010

ABSTRACT

Electrical and Optical Characterization of Molecular Nanojunctions

by

Daniel R. Ward

Electrical conduction at the single molecule scale has been studied extensively with molecular nanojunctions. Measurements have revealed a wealth of interesting physics. However, our understanding is hindered by a lack of methods for simultaneous local imaging or spectroscopy to determine the conformation and local environment of the molecule of interest.

Optical molecular spectroscopies have made significant progress in recent years, with single molecule sensitivity achieved through the use of surface-enhanced spectroscopies. In particular surface-enhanced Raman spectroscopy (SERS) has been demonstrated to have single molecule sensitivity for specific plasmonic structures. Many unanswered questions remain about the SERS process, particularly the role of chemical enhancements of the Raman signal.

The primary goal of the research presented here is to combine both electrical and optical characterization techniques to obtain a more complete picture of electrical conduction at the single or few molecule level. We have successfully demonstrated that nanojunctions are excellent SERS substrates with the ability to achieve single molecule sensitivity. This is a major accomplishment with practical applications in optical sensor design. We present a method for mass producing nanojunctions with SERS sensitivity optimized through computer modeling.

We have demonstrated simultaneous optical and electrical measurements of molecular junctions with single molecule electrical and SERS sensitivity. Measurements show strong correlations between electrical conductance and changes to the SERS response of nanojunctions. These results allow for one of the most conclusive demonstrations of single molecule SERS to date. This measurement technique provides the framework for three additional studies discussed here as well as opening up the possibilities for numerous other experiments.

One measurement examines heating in nanowires rather than nanojunctions. We observe that the electromigration process used to turn Pt nanowires into nanojunctions heats the wires to temperatures in excess of 1000 K, indicating that thermal decomposition of molecules on the nanowire is a major problem.

Another measurement studies optically driven currents in nanojunctions. The photocurrent is a result of rectification of the enhanced optical electric field in the nanogap. From low frequency electrical measurements we are able to infer the magnitude of the enhanced electric field, with inferred enhancements exceeding 1000. This work is significant to the field of plasmonics and shows the need for more complete quantum treatments of plasmonic structures.

Finally we investigate electrical and optical heating in molecular nanojunctions. Our measurements show that molecular vibrations and conduction electrons in nanojunctions under electrical bias or laser illumination can be driven from equilibrium to temperatures greater than 600 K. We observe that individual vibrations are also not in thermal equilibrium with one another. Significant heating in the conduction electrons in the metal electrodes was observed which is not expected in the ballistic tunneling model for electrons in nanojunctions this indicates a need for a more completely energy dissipation theory for nanojunctions.

Acknowledgments

This thesis and more importantly the research I've done over the past five years would not be possible without the help and support of several individuals. First I'd like to thank my advisor Dr. Natelson. Without his guidance none of this work would have been possible. He has always shown great enthusiasm for my research and instilled in me the idea that what I am doing is important. I am thankful for his faith in me to do things well outside both our fields of knowledge such as build microscopes. Most of all I am thankful for our numerous discussions on all matters of topics all of which I have greatly enjoyed.

I am grateful to my committee members Dr. Halas and Dr. Nordlander. They are also my coauthors on several publications and were instrumental in other publications. Without access to their equipment, simulations, and discussions it is likely much of this research would never have come to fruition.

I'd like to thank my fellow Natelson lab members both past and present for their help. In particular I'd like to thank Jay Lee for all his help with lithography and keeping me company during late nights at the lab. I'd also like to thank Jeff Worne for putting up with me for the last five years and keeping me company at lunch everyday.

Finally I'd like to thank my mom and dad. Their continued support, both financial and moral, has made this long journey possible. Thank you for the Sunday dinners with vegetables (especially broccoli), without which I would have surely caught scurvy.

Contents

Illustrations

Chapter 1

Introduction

1.1 Preface

This thesis will cover both the electrical and optical characterization of molecular nanojunctions, also known as nanogaps. Molecular nanojunctions have been demonstrated to be excellent tools for studying electrical conduction on the single molecule level[1, 2]. Studying electrical conduction at the single molecule level is motivated by the desire to continually shrink the size of electrical components such as transistors. Already transistor sizes have been reduced in size to tens of nanometers (hundreds of atoms). As further size reduction occurs we are approaching the single molecule limit. Electrical conduction in the single molecule regime can be significantly different than seen in bulk materials due to quantum effects. As such, further reductions in electrical component size pose much greater challenges than just fabrication, as the nature of the component's behavior will change depending on their size.

Electrical conduction in single molecules has been studied with nanojunctions for over a decade[1, 2, 3, 4]. The primary objective of our work has been to take the already well established electrical characterization of nanojunctions and single molecule devices, and incorporate optical characterization methods that we have developed[5] to greatly enhance our knowledge of electrical conduction and energy dissipation in single molecules in nanojunctions.

This thesis is organized into seven chapters. Chapter One will provide an overview

of the necessary background information to understand principles behind the experimental results presented in chapters two through seven. Chapter Two will discuss the use of surface-enhanced Raman spectroscopy (SERS) for optical characterization of molecules in nanojunctions. Chapter Three covers the first experimental demonstration of simultaneous optical and electrical measurements on nanojunctions. Chapter Four will take a slight detour and detail our investigation into the heating of nanowires which, as will be explained in Section 1.6, is of great importance in the fabrication of nanojunctions. Chapter Five will discuss methods for fabricating large arrays of nanojunctions on an industrial scale. Additionally, it will look at optimizations of the nanojunction geometry using finite-element modeling. Chapter Six discusses a combined electrical and optical measurement that provides quantative assessments of the electric field enhancement of bare nanojunctions. Finally Chapter Seven presents measurements demonstrating vibrational and electronic heating in molecular nanojunctions under electrical bias and optical fields.

1.2 Experimental Significance

The primary motivation behind our research has been to improve our understanding of single molecule (SM) electrical conduction. In general, each SM device is unique at the atomic level. The electrodes have slighly different shapes or crystallographic orientations, and the binding and configuration of the molecule of interest is slightly different. As a result, no two devices behave exactly the same. In order to understand these systems as a whole, hundreds of devices are fabricated and tested with the results averaged together to look for general trends in the electrical conduction. We propose to combine electrical measurements with optical measurements that are sensitive to the atomic configuration of the molecule of interest[6]. Currently we lack the

theoretical background to extract the most information possible from the data. However, by demonstrating that the measurement is possible, we hope to encourage more research in this area. Our measurements of energy distribution (temperature) in SM devices under electrical bias reveal that some of the electronic transport communities assumptions about heat dissipation are incorrect[7].

Beyond encouraging additional theoretical work on SM devices, our work has also had significance in field of SERS and optical sensors. We believe we have demonstrated one of the first, if not **the** first, implementation of SM SERS sensitivity that can be conclusively shown without relying on statistical arguments[6]. We have developed a SERS substrate with extremely high sensivity that can be produced on a large scale[5]. As discussed in Section 1.5.3, the field of SERS has many unsettled questions, including exactly how certain Raman enhancements occur. Our nanojunction structures are unqiuely able to address some of these questions due to our ability to electrically tune the system. Additionally, we have demonstrated a method for measuring the electric field enhancement between two electrodes with atomic spacing. These measurements demonstrate the need for more advanced quantum mechanical treatments of the interaction between nanostructures and light[8].

1.3   What is a Nanojunction?

Nanojunctions are metallic electrodes separated by distances ranging from less than an Angstrom to a few nanometers. These structures are typically used for studying the electrical properties of single molecules. In that case the molecule of interest is located in the gap between the two electrodes. Nanojunctions can be made many different ways, including the electromigration of nanowires[1], mechanical break junctions[9], and scanning tunnelling microscopes (STMs)[10]. This thesis will focus explicitly
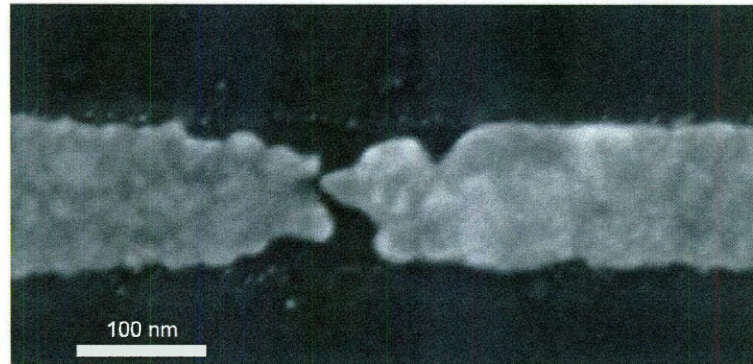
Figure 1.1 : SEM image of Au nanojunction.

on nanojunctions formed via electromigration, but the optical and electrical measurements would likely work for all nanojunctions. A scanning electron microscope (SEM) image of a typical electomigrated gold nanojunction is shown in Fig. 1.1.

Now that we know what a nanojunction is, we have to explain why we use them. The primary reason is that it has been well established that conductance in such structures is dominated by roughly a molecular volume[2, 11, 12, 13, 3, 14, 15, 16, 9, 17, 18, 19, 20, 21, 4, 22]. The reason that conduction occurs in such a small volume is that the tunnelling conduction G in a bare nanojunction (no molecule present) falls off exponentially, as described in Eqn. 1.1, where d is the internuclear distance between closest atoms, d_0 is the size of the metal lattice constant, β is the attenuation factor, and G_0 is the quantum of conductance as described in the next section.

$$G = G_0 \exp[-\beta(d - d_0)] \qquad (1.1)$$

Computer modelling gives values of $\beta = 1.85$ Å^{-1} for Au electrodes which means the conductance drops by $1/e$ for every 1.85 Å that the electrodes separate[8]. Conse-

quently, conduction in bare nanojunctions is dominated by the point in the nanojunction where the atoms are closest. In the presence of a molecule, whose conductance is typically on the order of 0.001 G_0[10], the conductance across the nanojunction is dominated by the molecule for all but the smallest of gaps.

1.4 Electrical Conduction in Single Molecules

Electronic conduction in single molecules is an active field of research. Electron transport in molecules is typically characterized via current-voltage (I-V) measurements. As discussed previously, there are numerous ways to make single molecule electrical devices, but actual electrical measurements can all be generalized to look like the setup shown in Fig. 1.2 where the measurement is either two or three terminal depending on if the device can be gated. In this configuration a molecule is connected to two electrodes which act as a source and drain. A bias is applied to the electrodes and the current through the molecule measured. A bias may also be applied to the gate which can capacitively shift the molecular energy levels relative to the source and drain chemical potentials.

There are multiple conduction mechanisms in molecules, including tunneling and charge hopping as well as vibronic effects[23, 24]. Tunneling conduction is the dominant mechanism in small molecules, and is illustrated by the energy diagrams shown in Fig. 1.3. There are two possible regimes of tunneling conduction: non-resonant and resonant. In non-resonant tunneling (Fig. 1.3A-C), when the junction is unbiased, the Fermi level E_f of the electrodes is the same and the molecule is shown to have two relevant molecular energy levels: the highest occupied molecular orbital (HOMO) and lowest unoccupied molecular orbital (LUMO). When placed under bias, the Fermi levels of the source and drain electrodes are shifted and current flows by
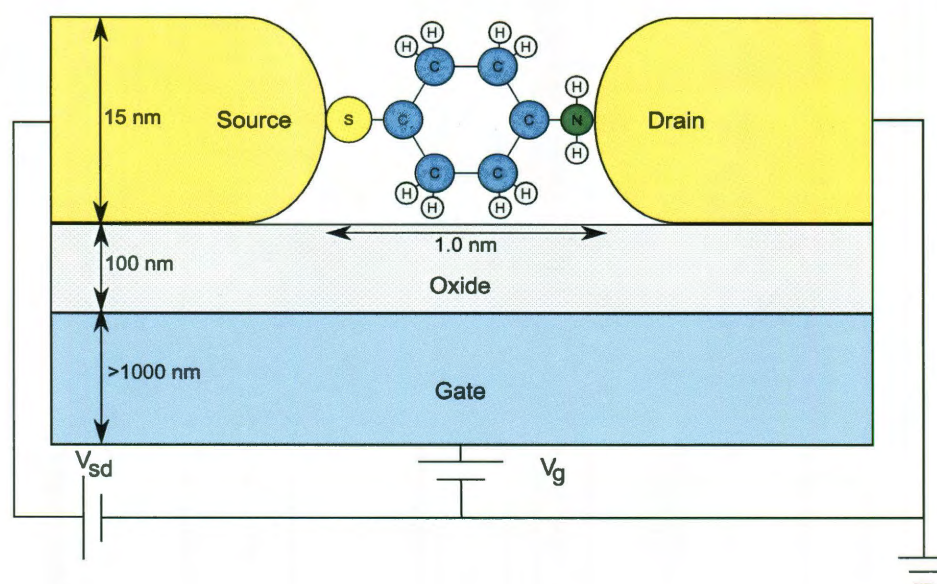
Figure 1.2 : Cartoon depicting a three terminal single molecule electronic device. A molecule is connected to two electrodes which act as a source and drain. A bias is applied to the electrodes, V_{sd}, and the current through the molecule measured. A bias may also be applied to the gate, V_g, which can capacitively shift the molecular energy levels. The drawing is not to scale but reasonable dimensions have been indicated.

tunneling from the source electrode into the LUMO level of the molecule and tunneling to the drain. By shifting the HOMO and LUMO levels relative to the source and drain energy levels via gating, it is possible to change the conductance through the molecule. Resonant tunneling (Fig. 1.3D-F) is similar, but the LUMO level is much closer to the Fermi level of the unbias electrodes. As a bias is applied the LUMO level ends up below E_f of one electrode and due to energy matching of electrons in the electrode with the LUMO energy level enhanced conduction occurs. In resonant tunneling the electrons remain coherent so quantum intereference effects are possible, leading to effects such as negative differential resistance (NDR)[23].

Although elastic tunnelling is the dominant conduction method in molecular junctions, other mechanisms that contribute to conduction can be observed in sufficiently stable molecular junctions. One mechanism of interest in this thesis (although not measured) is vibronic contributions to conduction, either inelastic or elastic. Inelastic contributions to conduction are illustrated in Fig. 1.4A. This process is similar to non-resonant tunneling except that electrons with energy greater than $\hbar\omega_\nu$ can impart $\hbar\omega_\nu$ worth of energy to a vibration during the inelastic tunneling process. This additional process adds another channel for conduction increasing the total current. The cross-section for this scattering process is small however, so the total change in current is difficult to detect. However by carefully measuring the second derivative of the current, d^2I/dV^2, it is possible to observe peaks in d^2I/dV^2 as a function of V_{sd} where the peaks correspond to the vibrational energies $\hbar\omega_\nu$ contributing to enhanced conduction. Plots of d^2I/dV^2 versus V_{sd} are called inelastic electron tunneling spectroscopy (IETS) spectra[24].

Elastic vibronic contributions to conduction are illustrated in Fig. 1.4B. This process is similar to resonant tunneling however the increased conduction is observed
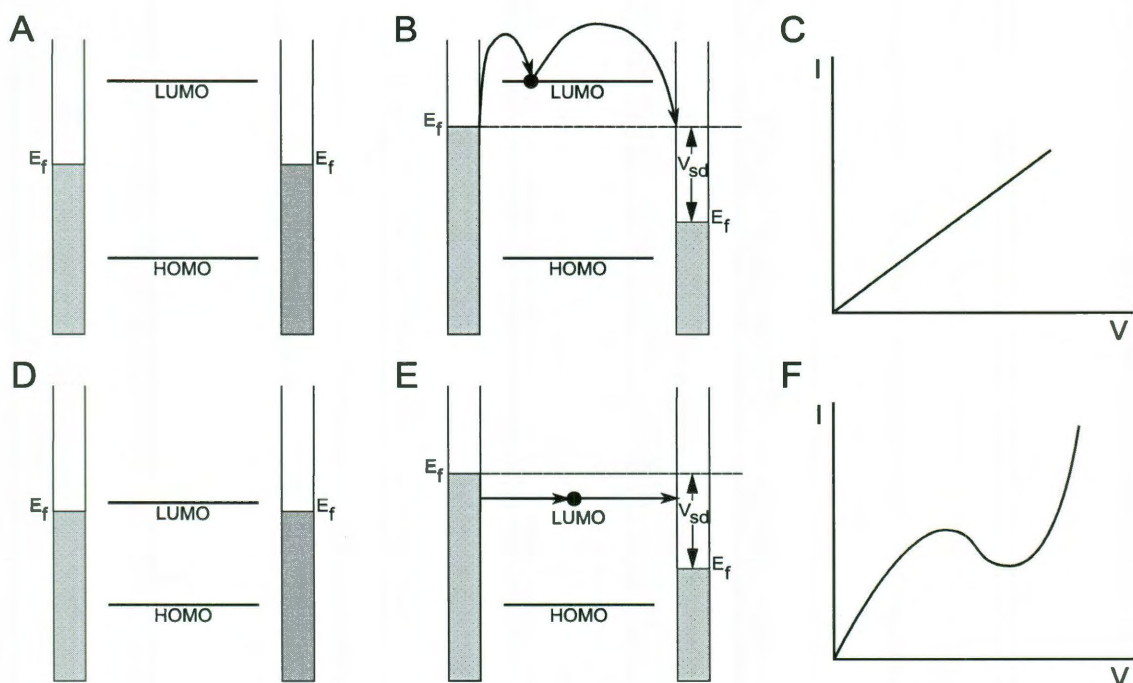
Figure 1.3 : Energy diagram for non-resonant (A-C) and resonant (D-F) tunneling electron transport in molecular junctions. A) Energy diagram for $V_{sd} = 0$. The filled states of the electrodes are indicated in gray. The quantized energy levels of the molelcule are as labeled. The LUMO level is energetically far away from E_f. B) When a bias is applied the filled states of the electrodes change and non-resonant tunneling conduction can occur via the LUMO of the molecule. The position of the HOMO and LUMO relative to the electrodes can be changed together by applying a gate bias V_g. C) Expected IV response for non-resonant tunneling. D) Energy diagram for $V_{sd} = 0$. The filled states of the electrodes are indicated in gray. The quantized energy levels of the molelcule are as labeled. The LUMO level is energetically close to E_f. E) When a bias is applied the filled states of the electrodes change and resonant tunneling conduction can occur via the LUMO of the molecule which is now below E_f of the left electrode. In this process the electrons remain coherent so quantum interference effects are possible. F) Possible IV response for tunneling demonstrating NDR.
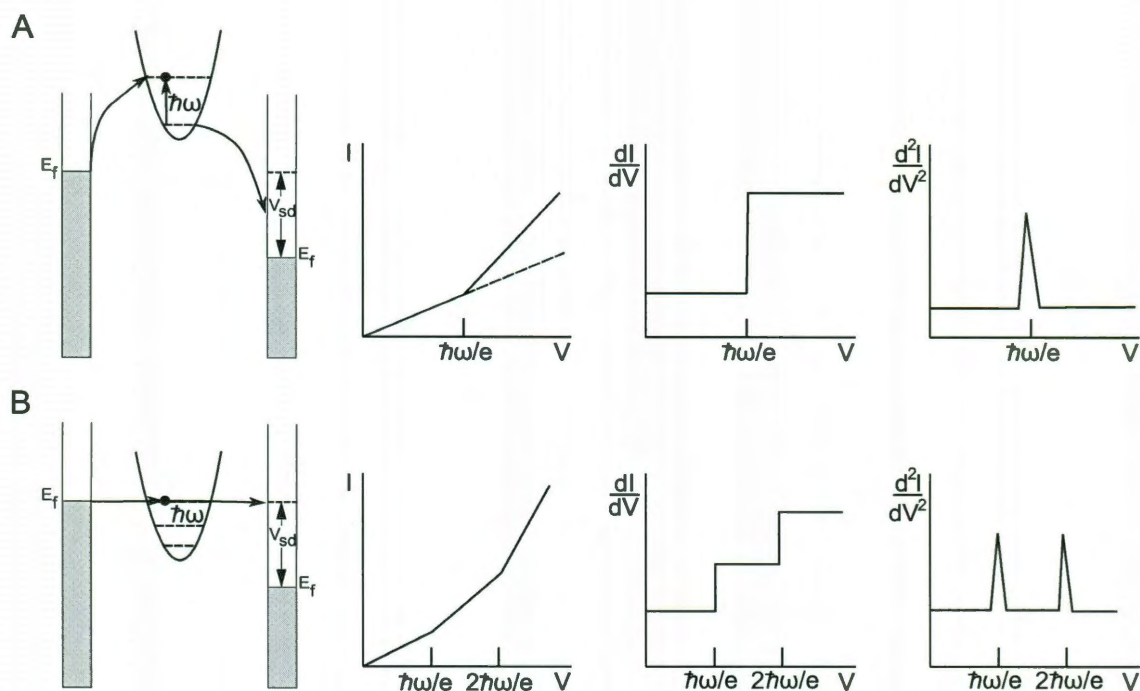
Figure 1.4 : A) Energy diagram for inelastic electron tunneling. When V_{sd} exceeds $\hbar\omega_\nu/e$ inelastic scattering off of a vibration ν can occur increasing the conductance (dI/dV) resulting in a peak in d^2I/dV^2 at $\hbar\omega_\nu/e$. B) Energy diagram for vibronic electron tunneling. Everytime E_f passes through a vibronic energy level a step is seen in conductance. Steps are observed every $\hbar\omega_\nu/e$ step in V.

to occur everytime E_f of the left electrode passes through a vibrational energy level of the LUMO. The resulting effect is peaks in dI/dV every $\hbar\omega_\nu/e$ change in V(assuming the vibrational energy levels are harmonic).

Numerous two-terminal electronic devices has been demonstrated at the single molecule level including diodes, optical switches and electrical switches[23]. Three terminal single-molecule transistors (SMTs) have have also been demononstrated extensively[4].

1.5   Raman and Surface-Enhanced Raman Spectroscopy

1.5.1   Raman Spectroscopy

Raman spectroscopy is a powerful tool for measuring rotational, vibrational, and electronic energy levels in molecules[25]. Raman spectroscopy uses the inelastic scattering of photons off of molecules, called Raman scattering, to measure these energy levels. With regards to Raman spectroscopy, this thesis will focus on vibrational Raman scattering, but Raman scattering from conduction electrons, which will be of importance in chapter 7, shall also be discussed briefly. The following discussion of Raman scattering is specifically for vibrational scattering, but the general idea remains true for all forms of Raman scattering.

When light scatters off molecules it is predominately elastically scattered. This is know as Raleigh scattering, and the incident and scattered photons have the same energy. A small potion of the time, inelastic scattering of the photons will occur, resulting in a scattered photon with different energy than the incident photon. The difference in energy between the incident and scattered photons is equal to the energy of the vibration with which the photon interacted.

Nonresonant Raman scattering occurs when a photon interacts with a molecule, exciting it from the electronic ground state to a virtual state. The molecule will then de-excite from the virtual state and return to the ground electronic state but it may return to a different vibrational energy level. Depending on the initial and final vibrational energy levels, the photon will undergo Rayleigh or Raman scattering as illustrated in Fig. 1.5. In Rayleigh scattering the initial and final vibrational levels are the same, so no change in energy is observed in the scattered photon. In Raman scattering the initial and final vibrational levels are different, yielding a
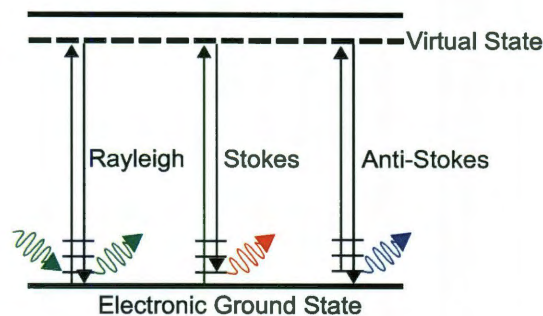
Figure 1.5 : Energy diagram of Rayleigh, Stokes Raman and anti-Stokes Raman scattering. In each case an incident photon excites the molecule to a virtual state that then decays back to some vibrational state emitting a photon in the process. The difference in the initial and final vibrational energy levels determines the energy of the emitted photon.

scattered photon of different energy. If the initial vibrational level is lower than the final vibrational level, the photon is said to have undergone Stokes scattering. If the opposite is true the photon is said to have undergone anti-Stokes scattering. Of the two scattering processes, Stokes scattering occurs more frequently as most vibrations will be in the ground state at typical experimental temperatures.

Raman scattering is a result of how charge in a molecule is rearranged by the incident light. The charge rearrangement manifests itself as an induced electric dipole in the molecule. The ease with which the electric field of light E can induce an electric dipole μ in the molecule is called the molecule's polarizability, α. The three parameters are related by the relationship $\mu = E\alpha$. Classically, if α is constant in time then $\mu(\omega_{in}t) = \alpha E(\omega_{in}t)$ and the induced dipole then oscillates at the same frequency as the incident field ω_{in}. In this event, radiation emitted from the molecule is at the same frequency as the incident radiation, which is Rayleigh scattering. If the molecule has vibrational modes that change the polarizability of the molecule as a function time then $\mu(t) = \alpha(\omega_{vib}t)E(\omega_{in}t)$ where $\alpha(\omega_{vib}t)$ oscillates at the frequency
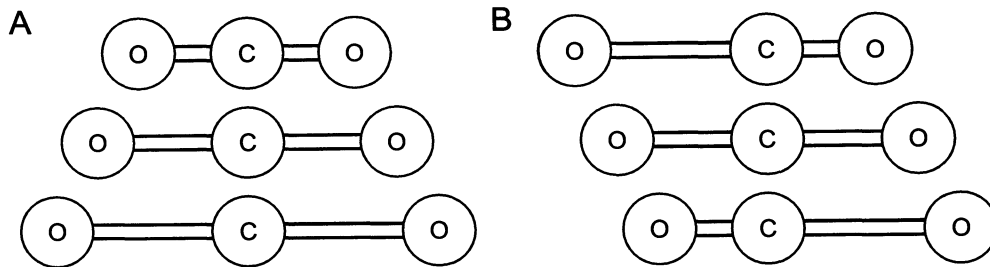
Figure 1.6 : Cartoon of symmetric (A) and anti-symmetric (B) stretches of CO_2. Stretch A is Raman active because the polarizability of the molecule changes as the oxygen atoms move away from the center carbon atom, making it easier to induce an electric dipole. Stretch B is Raman inactive because when the longer bond becomes more polarizable the shorter bond becomes more difficult to polarize resulting in no net change in the polarizability.

of the vibrational mode ω_{vib}. For $E(\omega_{in}t) = E_0\cos(\omega_{in}t)$ and $\alpha(\omega_{vib}t) = \alpha_0\cos(\omega_{vib}t)$ this implies that the induced dipole will oscillate like $\mu(t) = \frac{\alpha_0 E_0}{2}[\cos((\omega_{in} + \omega_{vib})t) + \cos((\omega_{in} - \omega_{vib})t)]$. Radiation emitted from the molecule will then have frequencies of either $\omega_{in} + \omega_{vib}$ or $\omega_{in} - \omega_{vib}$ which are Stokes and anti-Stokes Raman scattering respectively. As shown above, for Raman scattering to occur the polarizability of the molecule must change with time. Examples of vibrations that do and do not permit Raman scattering are shown in Fig. 1.6. Raman spectroscopy is a linear spectroscopy and the emitted intensity scales linearly with incident laser power. A typical Raman spectrum of a fluorinated oligophenylene ethynylene (FOPE) molecule is shown in Fig. 1.7.

Combined anti-Stokes and Stokes measurements can be used to measure the effective temperature of molecules as shown in Eqn. 1.2

$$\frac{I_{vib}^{AS}}{I_{vib}^{S}} = A_\nu \frac{(\omega_{in} + \omega_{vib})^4}{(\omega_{in} - \omega_{vib})^4}\exp(-\hbar\omega_{vib}/k_B T_\nu^{eff}). \qquad (1.2)$$

where I_{vib}^{AS} is the anti-Stokes intensity of a vibration ν, I_{vib}^{S} is the Stokes intensity
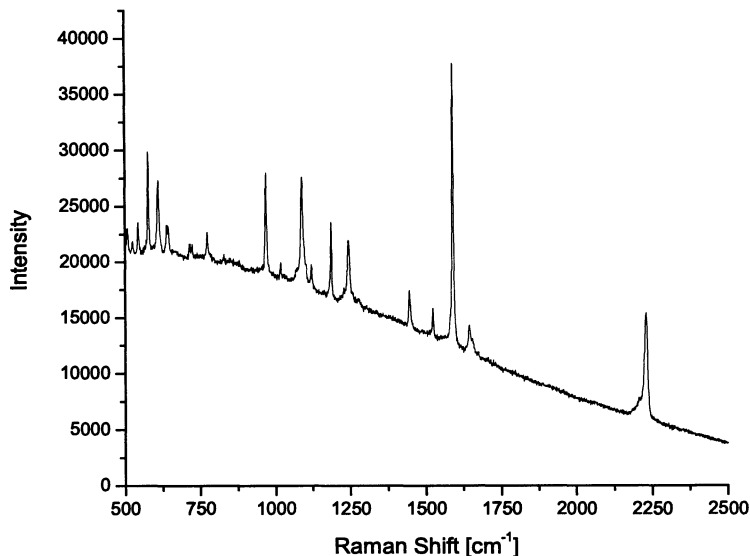
Figure 1.7 : Represenative Stokes Raman spectrum of a fluorinated oligophenylene ethynylene molecule (See Chapter 3) taken with a 785 nm diode laser on a commercial Raman microscope. The smooth background signal underneath the peaks is due to fluorescence.

of the same vibration and A_ν is a coefficient to account for differences in the Stokes and anti-Stokes scattering cross-sections. In solution-phase non-resonant Raman, A_ν is approximately one assuming that vibrational anharmonicity is small[25]. The $\frac{(\omega_{\text{in}}+\omega_{vib})^4}{(\omega_{\text{in}}-\omega_{vib})^4}$ term accomidates for the wavelength dependence of Raman scattering[26].

1.5.2 Plasmons

Before we can discuss surface-enhanced Raman spectroscopy, it is important to understand the idea of plasmons. Plasmons are collective oscillations of electrons relative to the ionic lattice in a metal. Plasmons are excited by the time varying electric field of incident light. When laser light is resonant with the plasmon in the metal, the metal's electrons will oscillate collectively and coherently with the incident radiation.

The resulting changes in electron density of the metal alter the local electric field around the metal. By exciting localized surface plasmons in metallic nanostructures, it is possible to increase the local electric field along the surface by factors greater than one hundred. Due to conservation of energy, the electric field will be enhanced in some locations along the surface and reduced in others.

Although more complicated treatments exist, Mie theory provides a qualitative picture of the origin of plasmons. From Mie theory it can be shown that the total cross-section for absorption and scattering (called extinction, σ_{ext}) in a nanoscale metal sphere in vacuum is given by[27]:

$$\sigma_{ext}(\omega) = \frac{9V}{c} \frac{\omega \epsilon_2(\omega)}{[\epsilon_1(\omega) + 2]^2 + \epsilon_2(\omega)^2} \tag{1.3}$$

where V is the particle volume, c is the speed of light and ϵ_1 and ϵ_2 are the real and imaginary parts of the metal's dielectric function respectively. As indicated σ_{ext} is frequency dependent because the dielectric function $\epsilon_1(\omega) + i\epsilon_2(\omega)$ is frequency dependent. It is clear that in the limit $\epsilon_1 \rightarrow -2$ and $\epsilon_2 \ll 1$, σ_{ext} becomes very large. This is the orign of plasmon resonances. Although other geometric shapes will require different values of ϵ_1 and ϵ_2 the idea of a vanishing denominator in the σ_{ext} remains the same.

Plasmonics has become a very active field of research driven in part by a desire to create plasmonically enhanced sensors. Plasmonically enhanced sensors rely on the locally increased electric field at the surface of plasmonically active metal structures to increase the signal strength for optical spectroscopy. In particular, surface-enhanced fluorescence, IR, and Raman spectroscopies have been studied extensively[28, 29, 30]. Since fluourescence and Raman spectroscopies are often performed at visible wavelengths, it is desirable to use metals with dielectric functions ϵ_1 that are negative at

the frequencies of visible light. Fortunately many metals meet this criteria, including gold, silver, copper, palladium and platnium[31].

1.5.3 Surface-Enhanced Raman Spectroscopy

Surface-enhanced Raman spectroscopy (SERS) is a form of Raman spectroscopy that was first observed in 1974[32] but was not identified until 1977 by Jeanmaire *et al*[33]. Early experiments demonstrated that Raman spectra of molecules adsorbed on roughened metallic electrodes are significantly stronger per molecule than those observed in normal solution-phase Raman spectroscopy. The signal enhancement factors were large, on the order of 10^5 to 10^6. In the following 30 years considerable progress has been made in understanding the origin of the SERS enhancement and in developing SERS substrates to maximize that enhancement[34].

The enhancement of the Raman signal in SERS is typically broken down into two factors: electromagnetic and chemical. The electromagnetic enhancement is attributed to plasmons and is entirely a function of the SERS substrate's geometry and dielectric function. This is the better understood and agreed upon enhancement of the two.

A simple derivation of electromagnetic SERS enhancment is as follows. If the incident field at the nanostructured metal is E_0 then the plasmonically enhanced field will be $E_s = gE_0$ where $g = g(\omega_{in})$ is the average enhancement over the metal surface and is dependent on the frequency of E_0. The emitted Raman field will then be $E_R \propto \alpha_R E_s \propto \alpha_R g E_0$ where α_R is the Raman tensor which originates from the polarizability of the molecule. The emitted Raman field is also enhanced by the nanoparticle by $g' = g'(\omega') = g'(\omega_{in} \pm \omega_{vib})$, now dependent on the Raman emission frequency. Thus the total SERS emitted field is $E_{SERS} \propto \alpha_R g g' E_0$. The intensity

of the SERS signal is then $I_{SERS} \propto |\alpha_R|^2 |gg'|^2 I_0$ where I_0 is the incident intensity. For low energy vibrations where $\omega' \approx \omega$ the enhancements will be similar ($g' \approx g$) and $I_{SERS} \propto |\alpha_R|^2 |g|^4 I_0$. Often SERS is reported to scale like $|E_L|^4$ where E_L is the normalized local incident electric field such that $|E_L|^4 = |\frac{E_s}{E_0}|^4 = |g|^4$. The fourth power dependence on the electric field can result in large SERS enhancements. In this limit, for a local electric field enhancement of $100\times$ the SERS signal will be enhanced by 10^8.

It is important to note that in the case of SERS, α_R is not the solution-phase polarizability. In SERS α_R is the polarizability of the molecule under the influence of its local environment, including the metal onto which it is adsorbed, which can greatly change α_R. In particular, if charge transfer occurs between the metal and molecule, α_R can differ dramatically from that of the isolated molecule, resulting in what is known as the chemical enhancement of SERS. The sensitivity to the local environment does in theory allow SERS to be used as a probe of the molecules conformation relative to the surface.

Chemical enhancement is very difficult to quantify and can have different meanings in the literature, but generally refers to any measured enhancement not accounted for by plasmonics. The origin of the chemical enhancement has not been conclusively demonstrated, but it is believed to be a result of mixing of the electronic and vibration wavefunctions of the molecule and metal, which can can result in charge transfer between the molecule and metal[35, 36].

As discussed previously it is often desirable to measure the ratio of anti-Stokes and Stokes intensities. In the case of SERS, A_ν in Eqn. 1.2, is no longer unity. Resonance effects must be considered. First, there are resonance effects between the laser light and molecule. If the incident photons are energetically close to electronic

transitions in a molecule, that can significantly increase Raman scattering. Second, plasmonic resonances can result in selective enhancement of either the Stokes or anti-Stokes signals. For nanostructures with sharp plasmon resonances, the approximation $g' \approx g$ is no longer valid. It is possible, but difficult, to correct for such effects[37].

Comparisons between SERS and normal Raman spectra show interesting differences. Interaction between the molecule and the metal surface in SERS allow vibrational modes that are typically prohibited in Raman spectroscopy due to either selection rules or $d\alpha_R/dt = 0$. For instance, it has been observed for the molecule *para*-mercaptoaniline that vibrations of a particular symmetry (b_2) that are normally very weak or non-existent in ordinary Raman spectroscopy are present and much stronger in SERS[35].

Another feature not seen in normal Raman but frequently observed in SERS is a strong background signal underneath the Stokes Raman peaks. There are two parts to this background signal: A component that decays superlinearly away from the Rayleigh line and a component that appears as a hump anywhere in the SERS spectrum. The first component falling off away from the Rayleigh peak is a result of Raman on the conduction electrons of the metal and is present even in the absence of molecules[38]. A precise theoretical model for this process remains elusive. The second component is an underlying background that can appear anywhere in the spectrum. This component is only observed in the presence of molecules on the metal surface. Only recently has a theoretical model been proposed that successfully captures the results of experiments[39]. The origin of the signal is a coupling between surface plasmon electrons and electrons in the metal which serves to increase coupling between the metal's electrons and the incident photons. This continuum is significantly enhanced in the precense of molecules that withdraw electrons from the

metal surface.

1.5.4 Single Molecule SERS

When SERS enhancements exceed 10^8, it becomes possible to detect the SERS response of a few or even single molecules. In 1997 Nie *et al.* and Kneipp *et al.* published separate papers detailing the observation of single molecule SERS for molecules assembled on silver colloids[40, 41]. Since then, a variety of SERS substrates, including engineered nanoparticles and lithographically defined metallic structures, have been developed with sensitivity high enough to measure SERS from a single or a few molecules[42, 43, 44].

In general it is difficult to prove that the SERS signal is from a single molecule. In fact, there has been some question as to whether the results from 1997 actually demonstrated single molecule sensitivity[45]. Empirically, two characteristic features of single or few-molecule SERS have been observed. The most prominent feature is spectral intensity fluctuations, where different modes in the Raman spectrum appear to "blink" by turning off and on in time[46, 47]. Blinking is attributed to the rearrangement of the molecule on the substrate surface, resulting in stronger or weaker enhancement of different modes. It is believed that this is indicative of single/few molecule SERS as it is unlikely that a collection of molecules would all change to the same orientation synchronously. In particular it has been observed that vibrational modes with different symmetry tend to blink differently. Fromm *et al.* observed that the a_1 symmetry modes of *para*-mercaptoaniline are stable in time while the weak b_2 symmetry modes tend to blink on and off on the time scale of seconds[44].

Another feature seen in single molecule SERS is spectral diffusion. Spectral diffusion is the shifting of the center frequency of Raman peaks as a function of time

independent of other peaks[47]. The origin of this phenomenon is also believed to be changes in the molecule's orientation and interaction with the SERS substrate. A change in orientation resulting in different interactions between the molecule and substrate could modify the vibrational energy levels of the molecule, resulting in energy shifts in the Raman spectrum. Another possible explanation for spectral diffusion is the presence of polar or charged contaminants near the molecules of interest. The electric field from polar molecules could be sufficiently large to cause vibrational Stark shifting of vibrational modes[48]. Again it, is believed that spectral diffusion is a sign of single/few molecule SERS as it is unlikely that such effects would occur simultaneously for large groups of molecules.

In general, effects like blinking and frequency shifts are attributed to the chemical enhancement part of SERS as the laser intensity and physical structure of the SERS substrate do not change with time preventing the electromagnetic enhancement from changing. Most likely in situations where blinking and frequency shifts are observed, there is base Raman signal provided by many molecules, with a few molecules providing the interesting dynamics in the SERS signal.

In addition to the background signals discussed in the previous section, single molecule SERS measurements typically have a background signal due to surface-enhanced fluorescence[37].

1.6 Electromigrated Nanogaps

Electromigration of nanowires is a technique developed to create nanometer sized gaps between metallic electrodes for use in single molecule electrical measurements[1, 2]. Numerous publications have established that conductance in these structures in dominated by a molecular volume[2, 11, 12, 13, 3, 14, 15, 16, 9, 17, 18, 19, 20, 21, 4,

22]. Electromigration occurs when a sufficiently large electrical bias is applied to a nanowire. Electromigration occurs because of two effects. First the conduction electrons in the nanowire transfer some of their momentum to the metal lattice pushing the atoms apart. This is known as the electron wind force and typically occurs at grain boundaries or other lattice defects. The second cause of electromigration is the electric field across the nanowire applies a force to any charge defects in the nanowire. Although electromigration is not a thermal process, Joule heating does improve electromigration by assisting atomic diffusion. A nanowire, or constriction of any type, is necessary to get sufficient current density to initiate electromigration. Current densities greater than 10^{12} A/m^2 are generally required to begin the process.

There are various methods for performing electromigration, but all of them have the same basic steps. First a bias is applied to the nanowire. The bias is then increased until the device resistance is observed to increase, indicating the onset of electromigration. Then a feedback loop is employed to control the voltage and thus the rate of electromigration until the wire is completely migrated. Total migration has occured once the nanogap conductance is less than a conductance quantum $G_0 = 2e^2/h \approx 3.8 \times 10^{-5}$ S. If the applied voltage is not well controlled, once electromigration begins the gap can be blown tens of nanometers wide making it unsuitable for electrical measurements.

For the experiments discussed in this thesis, electromigration was performed either by hand using a parameter analyzer or using a DAQ controlled by a computer. In either case the procedure was the same, although the computer controlled method has superior feedback control and thus a higher yield of usable nanogaps. The procedure is as follows: a voltage is ramped across the device upto a fixed value V_F and the current through the device measured. This is called an IV sweep. If the IV curve

is ohmic V_F is increased and another IV sweep is made. This process continues until there is a detectable drop in current with increasing voltage, at which point the bias is reduced to zero, V_F is reduced to its original value and the process is repeated until the resistance exceeds the desired value. For experiments performed in air, electromigration is stopped at 3 kΩ and the gap is allowed to self-break until the resistance exceeds $1/G_0$[49]. For experiments performed at 80 K in vacuum in our optical cryostat, the electromigration process was continued until the resistance exceeded 25 kΩ.

Electromigration has been used extensively to prepare electrodes for single-molecule conduction measurements with typical yields of ~10-20% for tunneling gaps inferred to contain individual molecules based on statistics on thousands of junctions[2, 11, 12, 3, 14, 15, 17, 18, 21, 4]. We have observe similar yields in our experiments[6].

1.7 Sample Fabrication

All samples presented in this thesis were fabricated in the same fashion unless noted otherwise. Samples were fabricated on n-type Si with 200 nm of thermal oxide. Nanowires approximately 120 nm wide were defined by e-beam lithography and e-beam evaporation of 0.5 nm Ti and 15 nm of Au. The nanowires are approximately 600 nm long and connected to larger electrical leads and contact pads. After evaporation of the metal liftoff was performed in acetone or chloroform and the nanowires cleaned of organic residue by exposure to O_2 plasma for 1 minute.

Chapter 2

Surface-enhanced Raman spectroscopy in nanogaps

2.1 Introduction

In this chapter I will discuss intial measurements of nanogaps as highly sensative SERS substrates[5]. We successfully demonstrated that electromigrated gold nanogaps exhibit very large SERS signals, with each electrode pair having one well-defined hot spot. Using confocal scanning Raman microscopy we demonstrated the localization of the enhanced Raman emission. The SERS response was consistent with a very small number of molecules in the hotspot, showing blinking and spectral diffusion of Raman lines. Sensitivity was sufficiently high that SERS from physisorbed atmospheric contaminants was detected after minutes of exposure to ambient conditions. The figure of merit for SERS substrates is the Raman enhancement factor. We estimated from experimental data that the Raman enhancement for para-mercaptoaniline (pMA) exceed 10^8. Finite-difference time-domain (FDTD) modeling of realistic structures revealed a rich collection of interelectrode plasmon modes that can readily lead to SERS enhancements as large as 5×10^5 over a broad range of illumination wavelengths.

2.2 Sample Fabrication

Samples were fabricated using the techniques and methodolgy presented in Section 1.7. Electron beam lithography was used to pattern "multibowtie" structures as
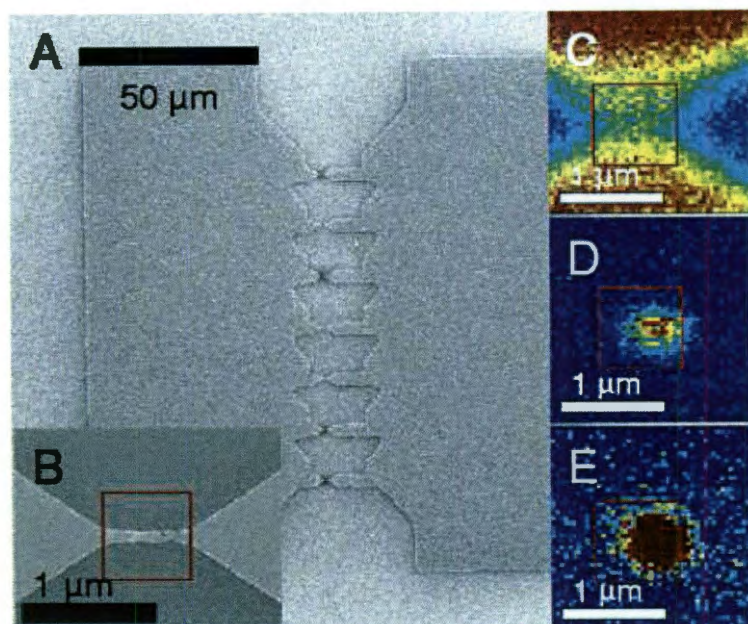
Figure 2.1 : A) Full multibowtie structure, with seven nanoconstrictions. B) Close-up of an individual constriction after electromigration. Note that the resulting nanoscale gap ($<\approx$5 nm at closest separation, as inferred from closer images) is toward the right edge of the indicated red square. C) Map of Si Raman peak (integrated from 500 to 550 cm^{-1}) in device from B, with red corresponding to high total counts. The attenuation of the Si Raman line by the Au electrodes is clear. D) Map of pMA SERS signal for this device based on one carbon ring mode (integrated from 1050 to 1110 cm^{-1}). E) Map of integrated low-energy background (50-300 cm^{-1}) for this device.

shown in Fig. 2.1A. The multibowties were placed in a vacuum probe station, and electromigration at room temperature (Section 1.6) was used to form nanometer-scale gaps in the constrictions in parallel, as shown in Fig. 2.1B. The number of parallel constrictions in a single multibowtie was limited by the output current capacity of our electromigration voltage source. A postmigration resistance of ≈ 10 kΩ for the structure in Figure 2.1A appears optimal.

Electromigrated multibowties have a few important advantages over the single constrictions used in other experiments. Most importantly multiple nanogaps can be created simultaneously. A side benifit of simulatenous electromigration is that its provides its own feedback loop to stop the electromigration process once one constriction becomes more resistive than the others. We observed that the individual constrictions migrate one at a time, however as soon as one begins to migrate its resistance increases reducing the current flow through the constriction stopping the migration process. This feedback mechanism reduces the need for precise operator or computer control of the electromigration process.

Postmigration high-resolution scanning electron microscopy (SEM) shows inter-electrode gaps ranging from too small to resolve to several nanometers. There are no detectable nanoparticles in the gap region or along the electrode edges. On the basis of electromigration of 283 multibowties (1981 individual constrictions), 77% of multibowties had final resistances less than 100 kΩ and 43% had final resistances less than 25 kΩ. We believe that this yield, already high, could be improved significantly with better process control, particularly of the lithography and liftoff.

2.3   SERS Measurements

The optical properties of the resulting nanogaps were characterized using a WITec CRM 200 scanning confocal Raman microscope in reflection mode, with normal illumination from a 785 nm diode laser. Using a $100\times$ objective, the resulting diffraction-limited spot was measured to be Gaussian with a full width at half-maximum of 575 nm. Fig. 2.1C shows a spatial map of the integrated emission from the 520 cm^{-1} Raman line of the Si substrate. The Au electrodes are clearly resolved. Polarization of the incident radiation is horizontal in this figure.

The SERS enhancement of the junctions has been tested using various molecules. The bulk of testing utilized pMA, which self-assembles onto the Au electrodes via standard thiol chemistry. Particular modes of interest are carbon ring modes at 1077 and 1590 cm^{-1}. Figure 2.1D shows a map of the Raman emission from the 1077 cm^{-1} line on the same junction as Figure 1B,C after self-assembly of pMA. This emission is strongly localized to the position of the nanogap. No Raman signal is detectable either on the metal films or at the edges of the metal electrodes. Figure 2.1E shows the spatial localization of the continuum background mentioned above.

Figure 2.2 shows a more detailed examination of the SERS response of the gap region of a typical junction after selfassembly of pMA. Figure 2.2A,B are time series of the SERS response, with known pMA modes indicated. The modes visible are similar to those seen in other SERS measurements of pMA on lithographically fabricated Au structures[44]. Each spectrum was acquired with 1 s integration time, with the objective positioned over the center of the nanogap hotspot. Temporal fluctuations of both the Raman intensity ("blinking") and Raman shift (spectral diffusion), generally regarded as hallmarks of few- or single-molecule SERS sensitivity[50], are readily apparent. Figure 2.2C shows a comparison of the wandering of the 1077 cm^{-1} pMA
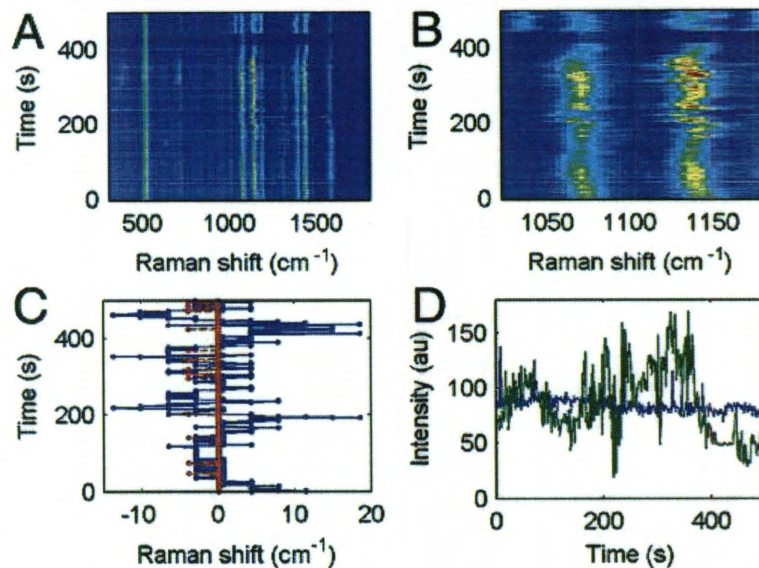
Figure 2.2 : A) Waterfall plot (1 s integration steps) of SERS spectrum at a single nanogap that had been soaked in 1 mM pMA in ethanol. Identified pMA peaks include the ring modes at 1077 cm^{-1} and 1590 cm^{-1}, as well as an 1145 cm^{-1} δCH mode with b_2 symmetry, an 1190 cm^{-1} mode identified as δCH of a_1 symmetry, a mode near 1380 cm^{-1} identified as δCH + νCC of b_2 symmetry, and a mode near 1425 cm^{-1} identified as νCC + δCH of b_2 symmetry. Mode assignments are based on Ref. [35]. B) Close-up of A to show correlated wandering and blinking of 1077 cm^{-1} and 1145 cm^{-1} modes. C) Comparison of 1145 cm^{-1} mode position (blue) with the Si Raman peak (red), which shows no such wandering. The jitter in the Si peak position is 1 pixel in the detector. D) Comparison of 1145 cm^{-1} peak height (green, found by a Gaussian fit to the peak) fluctuations with those of the Si peak (blue).

line with that of the 520 cm^{-1} Raman line of the underlying Si substrate over the same time interval. This demonstrates that the spectral diffusion is due to changes in the molecular environment rather than a variation in spectrometer response. Figure 2.2D shows the variation in the peak amplitudes over that same time interval.

This blinking and spectral diffusion are seen routinely in these junctions. We have observed such Raman response from several molecules, including self-assembled films of pMA, para-mercaptobenzoic acid (pMBA), a Co-containing transition metal complex[51], and spin-coated poly(3-hexylthiophene) (P3HT). These molecules all have distinct Raman responses and show blinking and wandering in the junction hotspots.

2.4 Polarization Depedence

Rayleigh-scattered light from nanogap structures show significant changes upon polarization rotation, while the SERS response is approximately independent of polarization as seen in Fig. 2.3.

A polarization indepent SERS enhancement for nanogaps may be surprising given the starting symmetry of the structure. Electromigration does not however produce prefectly symmetric gaps. The lack of symmetry prevents strong dipole or quadrapole plasmon resonances that typically lead to the large SERS enhancements seen in other plasmonic structures such as nanoparticle dimers. Instead we hypothesize that the enhancement in nanogaps comes from higher order edge plasmons which collectively have no polarization. Such a theory also explains the broadband response of nanogaps as modeled below.

Freshly cleaned nanogaps showed no Stokes-shifted Raman emission out to 3000 cm^{-1}. However, in 65% of clean nanogaps examined, a broad continuum background is seen
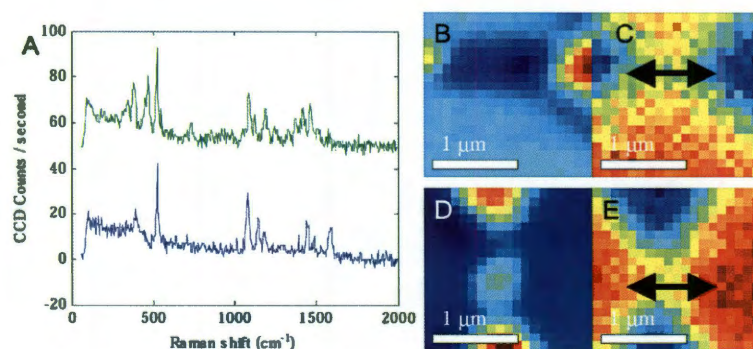
Figure 2.3 : A) Raman spectra at hotspot of bowtie with pMA assembled on surface. The blue spectrum is with polarization at 0 degrees. (direction shown in C). The green spectrum has been shifted 50 counts/s for clarity and is at the same hotspot but with the polarization rotated 90 degrees relative to the substrate (direction shown in D). B) Spatial plot of integrated signal over -40 to 40 cm^{-1} showing the Rayleigh scattering from the center of the device. Red is high intensity blue is low intensity. The large pads are at the left/right. Polarization direction indicated in C. C) Spatial plot of integrated Si signal over 500-540 cm^{-1}. Red indicates Si, blue is Au pads. Polarization direction is indicated by the arrow. D) Spatial plot of integrated signal over -40 to 40 cm^{-1} showing the Rayleigh scattering from the center of the device for the sample rotated 90 degrees relative to B, C. Red is high intensity blue is low intensity. Polarization direction is indicated in E. There is a local maximum in the Rayleigh scattering at the center of the gap. E) Spatial plot of integrated Si signal over 500-540 cm^{-1}. Red indicates Si, blue is Au pads. Polarization direction is indicated by the arrow.

(Fig. 2.4A), decaying roughly linearly in wavenumber out to 1000 cm^{-1} before falling below detectability. This background is spatially localized to a diffraction-limited region around the interelectrode gap and is entirely absent in unmigrated junctions. The origin of this continuum, similar to that seen in other strongly enhancing SERS substrates[43], is likely Raman scattering from electrons in the gold electrodes[52]. A more detailed invisigation into Raman scattering from electrons will be discussed in Section 7.6. In samples coated with molecules, this background correlates strongly with visibility of SERS. No junctions without this background displayed SERS signals. Like the SERS signal, this background is approximately polarization independent. Temporal fluctuations of this background in clean junctions are minimal (Fig. 2.4D), strongly implying that fluctuations of the electrode geometry are not responsible for SERS blinking.

2.5 Concentration Depedence

We have examined SERS spectra for varying supernatant solution concentration during the assembly procedure. Ideally, successive dilutions of the solution should vary surface coverage of the assembled molecules. While molecular coverage on the edges of polycrystalline Au films is not readily assessed, we observe reproducible qualitative trends as concentration is reduced. For pMBA molecules assembled from solutions in nanopure water, we have varied concentrations from 1 mM down to 100 pM. The fraction of junctions showing SERS distinct from carbon contamination remains roughly constant down to concentrations as low as 1 μM. For our volumes and electrode areas, this is still expected to correspond to a dense coverage of 1 molecule per 0.19 nm^2. At concentrations below 1 μM, SERS spectra change significantly, while remaining distinct from those of carbon contamination: blinking occurs more frequently; modes
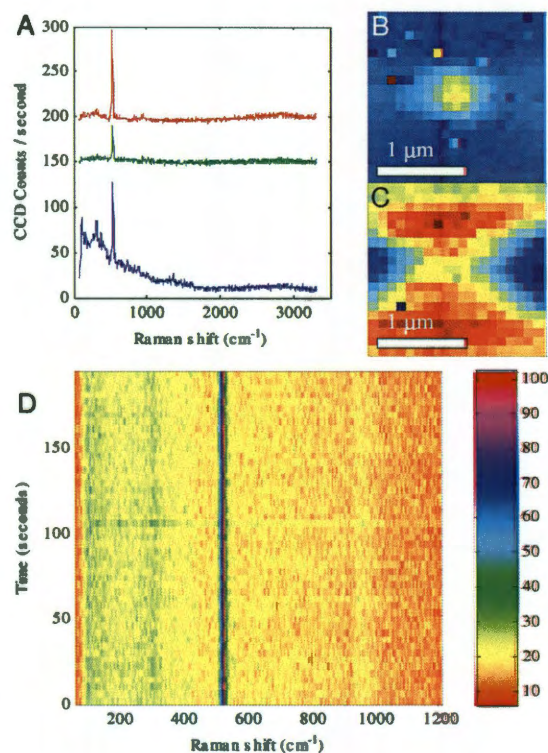
Figure 2.4 : A) Raman spectra at hotspot (blue) of a clean bowtie, Au pad(green), and over Si substrate(red). The continuum is very strong at the hotspot and shows linear slope from 0 to $\tilde{1}500$ cm^{-1}. Also visible are the 300 cm^{-1} peak and 520 cm^{-1} peaks of the Si substrate and a weak peak at 1345 cm^{-1} indicating the onset of atmospheric contamination after approximately 15 minutes of air exposure. Curves have been offset by 150 counts/s (green) and 200 counts/s (red) for clarity. B) Spatial plot of integrated signal over 600-800 cm^{-1} showing the localization of continuum to the center of the device when compared to the Si plot C. Yellow is strong signal; blue is no signal. C) Spatial plot of integrated Si signal over 500-540 cm^{-1}. Red indicates strong Si signal the blue areas show where the Au pads are. D) Time spectra of clean bowtie. The intensity is reported in CCD counts/second. No blinking of the continuum is observed. The lowest wavenumbers are reported to have zero counts/second due to the low pass filter used to block out the laser.

of b_2 symmetry rather than a_1 symmetry appear more frequently; and the molecular peaks can be more than 100× larger than the high coverage case for the same integration times. These observations are qualitatively consistent with the molecules exploring different surface orientations at low coverages, and charge transfer/chemical enhancement varying with orientation. However, the actual coverage at the edges remains unknown.

The concentration of the solution used for assembling molecules on the nanogap surface strongly influences the form of the observed Raman spectrum as well as the rate and intensity of the mode blinking. Raman spectra of pMBA were taken by soaking samples in 2 mL of different concentrations of pMBA. Although for all of these concentrations there are enough molecules in solution to form a monolayer over the bowtie surface, significant differences in the spectra were observed. Fig. 2.5A shows a representative Raman spectrum for pMBA at the nanogap for 1 mM concentrations. The two carbon ring modes at 1077 cm^{-1} and 1590 cm^{-1} are clearly present along with a third peak at 1463 cm^{-1}. The time spectra for this nanogap in Fig. 2.5B. The 1077 cm^{-1} and 1590 cm^{-1} peaks are relatively stable and always present while other modes, such as the 1463 cm^{-1} mode, blink on and off for a few seconds at a time. As the concentration is decreased to 1 μM, the pMBA signal tends to be stronger with more intense blinking. Additionally the 1077 cm^{-1} mode is observed to disappear while the 1590 cm^{-1} mode remains. Additional modes begin to become more visible such as the 1265 cm^{-1} and 1480 cm^{-1} modes seen in Fig. 2.5C. At even lower concentrations such as 1 nM, the pMBA signal is again more intense with even more blinking as seen in Fig. 2.5F (which has been plotted with intensity on a log scale). The 1077 cm^{-1} mode is again unseen while the 1590 cm^{-1} mode begins to fluctuate in intensity even more. The blinking becomes much more intense
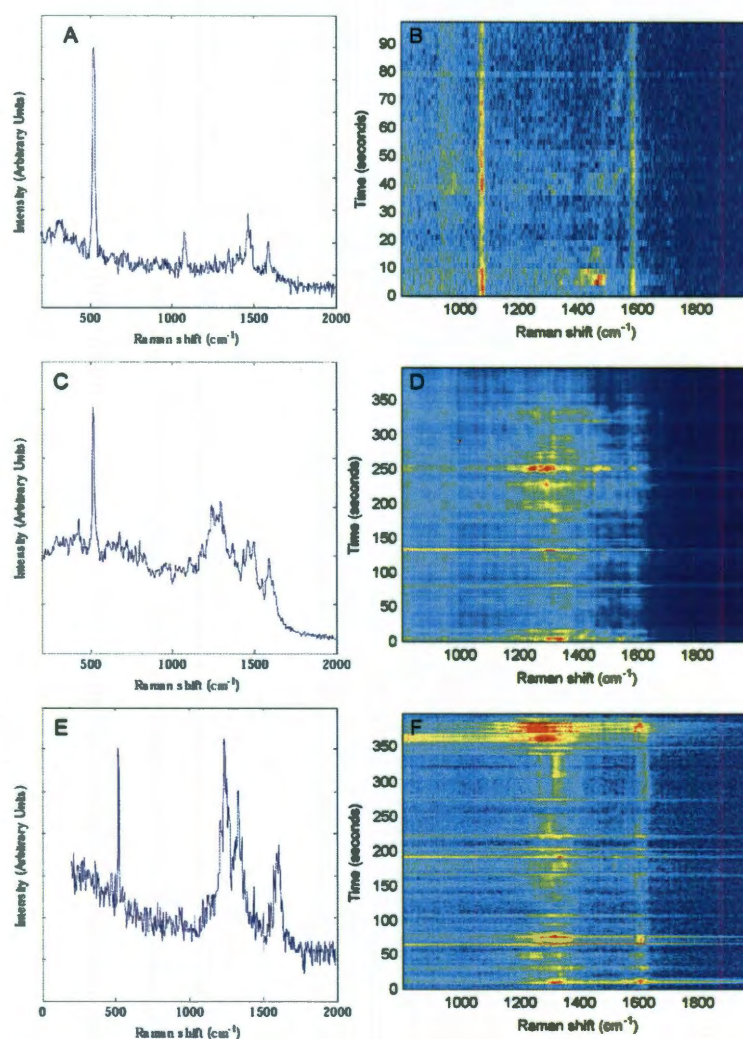
Figure 2.5 : A) Raman from pMBA at 1 mM concentration taken at $t = 10$ s. B) Corresponding time spectrum for 1 mM. C) Raman from pMBA at 1 μM concentration taken at $t = 251$ s. D) Corresponding time spectrum for 1 μM. E) Raman from pMBA at 1 nM concentration taken at $t = 24.5$ s. F) Corresponding time spectrum for 1 nm, plotted on log intensity scale. For all time spectra blue (red) indicates low (high) Raman intensity.

with the intensity of the signal periodically reaching close to ten times the maximum intensity observed for pMBA at 1 μM. We suggest that the increased blinking and larger amplitude signals are a result of the molecules not being as tightly packed on the surface in the 1 μM and 1 nM cases as in the 1 mM case. As a result of looser packing, the molecules are free to explore more surface conformations, including those with more and different charge transfer with the Au surface.

We point out that these pMBA spectra are distinct from those seen in physisorbed carbon contamination on initally clean junctions. These spectra persist at high incident powers and do not show "arrival" phenomena as described in the subsequent section. Furthermore, they are unlikely to originate from photodecomposition of pMBA, since the illumination conditions are identical for all coverages.

2.6 Carbon Contamination Issues

Another indicator of very large enhancement factors in these structures is sensitivity to exogenous, physisorbed contamination. Carbon contamination has been discussed in the context of both SERS and TERS[53, 47, 54]. Our nanogap substrate is sensitive enough to examine such contaminants as seen in Fig. 2.6. While clean junctions with no deliberately attached molecules initially show only the continuum background, gap-localized SERS signatures in the sp^2 carbon region between 1000 and 1600 cm^{-1} are readily detected after exposure to ambient lab conditions for tens of minutes. Nanojunctions that have been coated with a self-assembled monolayer (SAM) (for example, pMA) do not show this carbon signature, even after hours of ambient exposure. Presumably this has to do with the extremely localized field enhancement in these structures, with the SAM sterically preventing physisorbed contaminants from entering the region of enhanced near field.
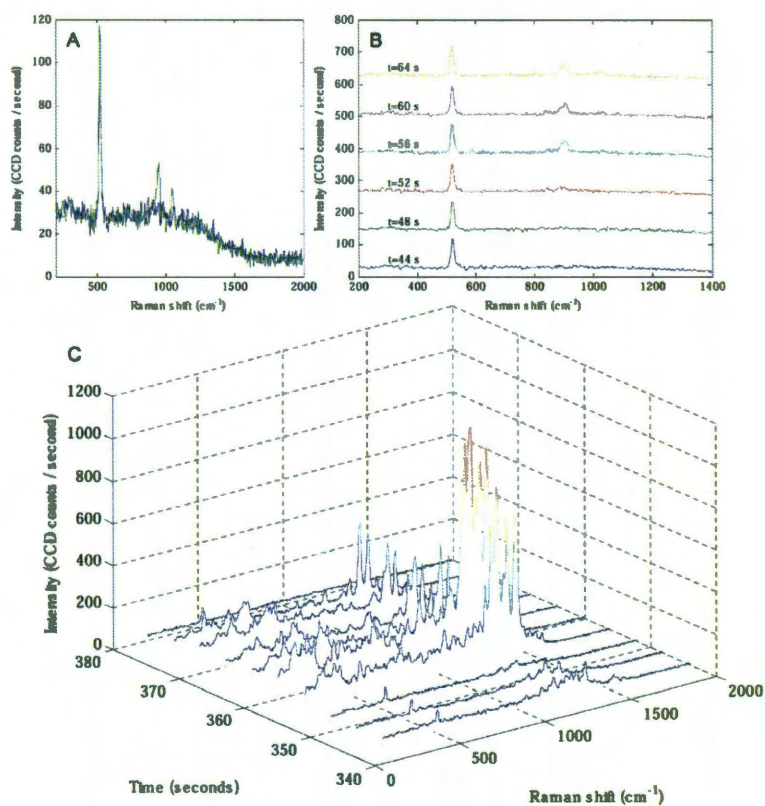
Figure 2.6 : A) Raman spectra for clean bowtie (blue) and clean bowtie after a few minutes exposed to the air (green). This change in the Raman spectrum is indicative of contamination for surface absorbed molecules from the air. B) Raman spectra for a clean bowtie showing the onset of a contaminant signal at 900 cm^{-1} as time progresses. C)Waterfall plot showing the extremely strong blinking observed for adsorbed contamination. The fluctuations are much larger than the those observed for dense coverage of pMA, pMBA, or P3HT. Notice the scale relative to the 520 cm^{-1} Si peak seen at t = 340 s.
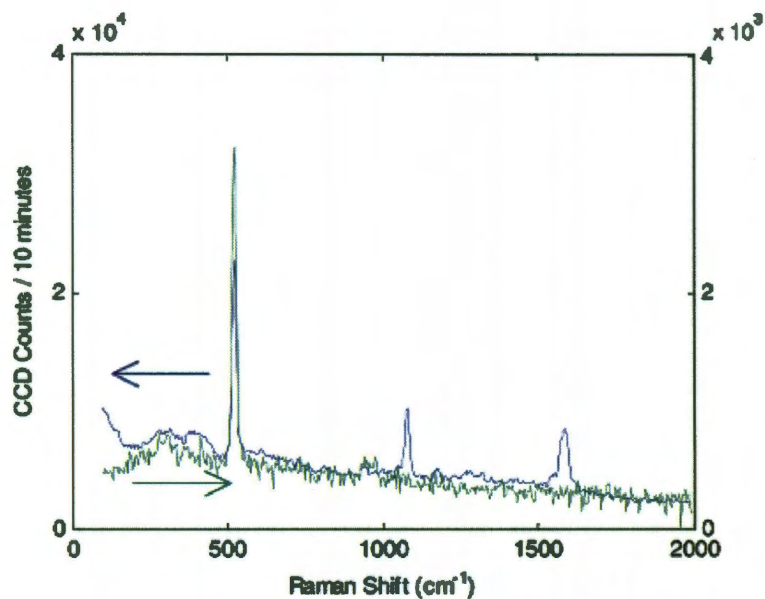
Figure 2.7 : Blue curve (left scale): pMA SERS spectrum at hotspot center of one nanojunction densely covered by pMA, integrated for 10 min at incident power of 700 μW. Green curve (right scale): integrated signal under same conditions on middle of Au pad on the same nanojunction. The feature near 960 cm^{-1} is from the Si substrate. No Raman features are detectable on either the Au pads or their edges under these conditions.

Recently arrived contaminant SERS signatures abruptly disappear within tens of seconds at high incident powers (1.8 mW), presumably due to desorption. SERS from covalently bound molecules is considerably more robust, degrading slowly at high powers and persisting indefinitely for incident powers below 700 μW. SEM examination of the nanogaps shows no optically induced damage after exposure to intensities that would significantly degrade nanoparticles[55]. The large extended pads likely aid in the thermal sinking of the nanogap region to the substrate.

2.7 Raman Enhancement Factor

Estimating enhancement factors rigorously is notoriously difficult, particularly when the hotspot size is not known. Although SERS enhancement volume measurements are possible using molecular rulers[56], this is not feasible with such small nanogaps. Junctions made directly on Raman-active substrates (Si with no oxide; GaAs) show no clearly detectable enhancement of substrate modes in the gap region, suggesting that the electromagnetic enhancement is strongly confined to the thickness of the metal film electrodes. Figure 2.7 shows a comparison between a typical pMA SERS spectrum acquired on a junction with a 600 s integration time at 700 μW incident power and a spectrum acquired over one of that devices Au pads for the same settings. The pad spectrum shows no detectable pMA features and is dark current limited.

Using the data from the device in Fig. 2.7, we estimate the total enhancement in that device. To be conservative, we assume a hotspot effective radius of 2.5 nm with dense packing of pMA, giving $N \approx 100$ molecules. Blinking and wandering suggest that the true N value is much closer to one. The integrated Raman signal over a Gaussian fit to the 1077 cm^{-1} Raman line is 2.0 counts/s/molecule when the incident power is 700 μW. For our apparatus, the count rate from imaging a bulk crystal at the same equivalent power is 4.2×10^{-9} counts/s/molecule, so that we estimate a total enhancement of at least 5×10^8.

To estimate an Raman enhancement it was necessary to understand the effective count rate per molecule of Raman scattering from bulk pMA in our measurement setup. This requires knowing the effective volume probed by the WITec system when the laser is focused on a bulk pMA crystal.

The full-width-half-maximum (FWHM) of the laser spot size was found to be 575 nm. This was determined by measuring the count rate of the Rayleigh scattering

peak (at zero wavenumbers) as a function of position as the beam was scanned over the edge of a Au film on a Si substrate. Averaging 16 such scans, the Rayleigh intensity was fit to the form of an integrated gaussian to determine the FWHM of the gaussian beam. The 575 nm figure is likely an overestimate due to systematic noise in the flat regions of the fit.

For a gaussian beam with intensity of the form $\propto e^{\frac{r^2}{2\sigma^2}}$, the FWHM $= 2\sqrt{2\ln 2}\sigma$. The effective radius of an equivalent cylindrical beam is 2σ, or 346 nm in this case. The effective confocal depth[57] was determined by measuring the 520 cm^{-1} Si Raman peak as a function of vertical displacement of a blank substrate. The effective depth profile was determined by numerical integration of the Si data. The effective volume probed by the beam is 1.92×10^{-12} cm^3. From the bulk properties of pMA, this corresponds to 1.09×10^{10} molecules.

The count rate for the bulk pMA 1077 cm^{-1} line, corrected by the ratio of (Si SERS rate/Si bulk rate) to accomodate for the difference in laser powers, is 46 counts/s, compared with 203 counts/s for the SERS data of Fig. 2.7. This leads to the enhancement estimate of 5×10^8.

2.8 FDTD Simulations

We use FDTD calculations to understand the strong SERS response in these structures and roughly estimate enhancement factors. It is important to note that the finite grid size (2 nm) required for practical computation times restricts the quantitative accuracy of these calculations. However, the main results regarding spatial mode structure (allowing assessment of the localization of the hotspot) and energy dependence are robust to these concerns, and the calculated electric field enhancement is an *underestimate*[58]. Figure 2.8 shows a calculated extinction spectrum and map of
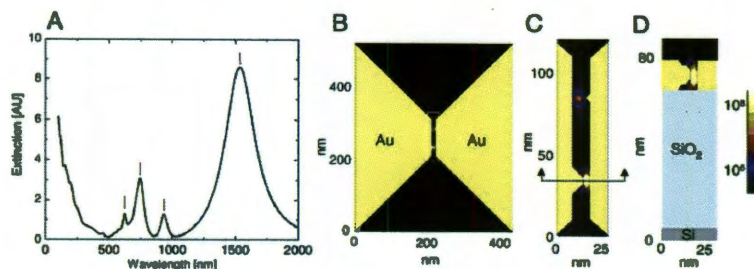
Figure 2.8 : A) FDTD-calculated extinction spectrum from the model electrode configuration shown in B. B) Mock-up electrode tips capped with nanoscale hemispherical asperities, with $|E|^4$ plotted for the 937 nm resonance of A. Constriction transverse width at narrowest point is 100 nm. Gap size without asperities is 8 nm. Asperity on left (right) electrode has radius of 6 nm (4 nm). Au film thickness is 15 nm, SiO_2 underlayer thickness is 50 nm. Radiation is normally incident, with polarization oriented horizontally. Grid size for FDTD calculation is 2 nm. C) Close-up of central region of B, showing extremely localized enhancement at asperities. D) Cross section indicated in C, showing that enhancement in this configuration does not penetrate significantly into the substrate. Predicted maximum electromagnetic Raman enhancement in this mode exceeds 10^8.

$|E|^4$ in the vicinity of the junction. These calculations predict that there should be large SERS enhancements across a broad bandwidth of exciting wavelengths because of the complicated mode structure possible in the interelectrode gap. Nanometer-scale asperities from the electromigration process break the interelectrode symmetry of the structure. The result is that optical excitations at a variety of polarizations can excite many interelectrode modes besides the simple dipolar plasmon commonly considered. For extended electrodes, a continuous band of plasmon resonances coupling to wavelengths from 500 to 1000 nm is expected[59]. This broken symmetry also leads to much less dependence of the calculated enhancement on polarization direction, as seen experimentally. The calculations confirm that the electromagnetic enhancement is confined in the normal direction to the film thickness. Laterally, the field enhancement is confined to a region comparable to the radius of curvature of the asperity.

For gaps and asperities in the range of 2 nm, purely electromagnetic enhancements can exceed 10^{11} approaching that sufficient for single-molecule sensitivity.

2.9 Conclusion

We have demonstrated a SERS substrate capable of extremely high sensitivity for trace chemical detection. Unlike previous substrates, these nanojunctions may be mass fabricated in controlled positions with high yield using a combination of standard lithography and electromigration. The resulting hotspot geometry is predicted to allow large SERS enhancements over a broad band of illuminating wavelengths. Other nonlinear optical effects should be observable in these structures as well.

The extended electrode geometry and underlying gate electrode are ideal for integration with other sensing modalities such as electronic transport which will be discussed in the next chapter.

Chapter 3

Simultaneous measurements of electronic conduction and Raman response in molecular junctions

3.1 Introduction

In this chapter the SERS measurement techniques from Chapter 2 are combined with simultaneous measurements of electronic conduction in gold nanojunctions. The conductance as a function of time is observed to correlate strongly with the SERS signal in 11% of the junctions measured. Conductance changes correlate with sudden changes in the intensity of sets of Raman modes ("blinking") and with spectral diffusion of mode positions. The data suggest that both SERS and conductance changes are most likely due to changes in molecular conformation and binding. The combined data provide a great deal of information about the effect of molecular orientation and environment on both conduction and SERS, although a detailed understanding of this correlated information is indeed a very significant theoretical challenge. The most likely explanation for these results is that single-molecule multimodal sensing is possible, and that mass producible nanogap structures can achieve single-molecule SERS sensitivities. This combined measurement technique also opens the possibility of direct assessment of vibrational pumping and local heating in single-molecule electronic transport which will be dicussed in chapter 7.
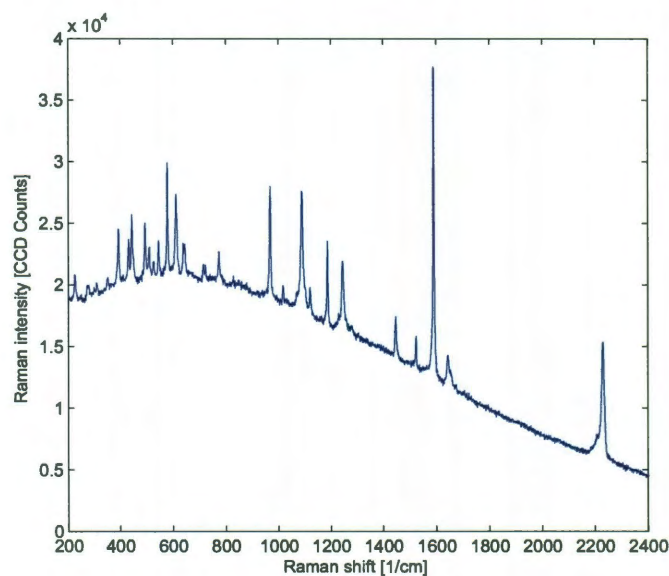
Figure 3.1 : Raman spectrum of bulk FOPE crystal taken in Renishaw Raman microscope at 785 nm. Curvature and offset of spectrum is due to fluorescence.

3.2 Sample Fabrication

Samples were fabricated using e-beam lithography as outlineed in section 1.7. For the devices discussed below the metallic constrictions were approximately 500 nm long and 100-180 nm wide. For devices incorporating para-mercaptoaniline (pMA), samples are immediately placed in a 1 mM solution of pMA in ethanol. Samples are soaked in the pMA solution for 12 to 24 hours as pMA self-assembles on the Au surfaces, followed by an ethanol rinse to remove any excess pMA. We also measured devices using a fluorinated oligophenylene ethynylene (FOPE)[60] that possesses a distinctive Raman spectrum shown in figure 3.1.

Nanogaps were formed in the constrictions via electromigration (Section 1.6) using an automated procedure to form an atomic-scale constriction with a resistance of
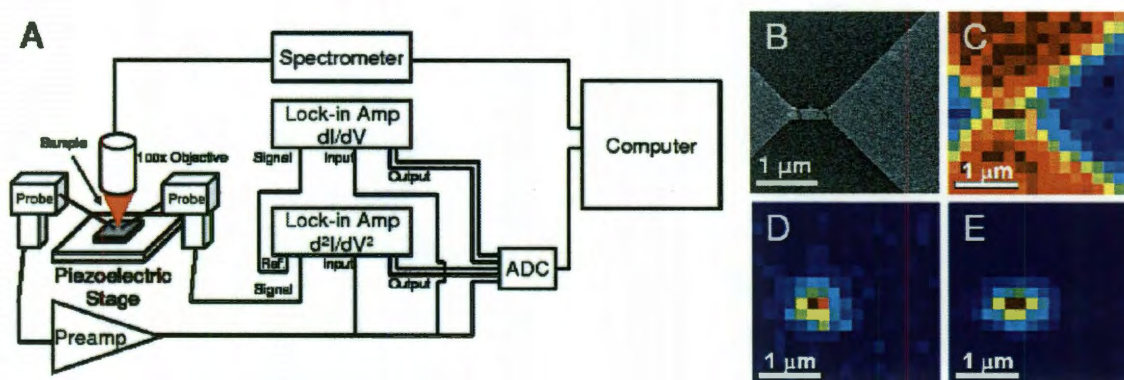
Figure 3.2 : A) Schematic of the electronic measurement. A 100 mV RMS AC signal is sourced by a lock-in into one pad. The AC current and its second harmonic are measured by lock-in amplifiers. The DC current is sampled with a current-to-voltage amplifier at 5 kHz. Raman spectra are synchronously captured with 12 s integrations at an incident 785 nm wavelength laser intensity of about 0.5 mW. B) Scanning electron image of Au constriction with nanogap. The constriction is 180 nm wide with a gap <5 nm in size. C) Map of the substrate Si 520 cm^{-1} peak (integrated from 480 to 560 cm^{-1}) of the device from B. Red corresponds to the highest number of CCD counts and blue represents the fewest counts. The Au pads which attenuate the Si signal are clearly visible. D) Map of the pMA SERS signal from device in B from the a1 symmetry mode at 1590 cm^{-1} (integrated from 1550 to 1650 cm^{-1}), showing that the Raman signal is localized only to the nanogap region. E) Map of integrated continuum signal (due to inelastic Raman scattering from the metal electrodes) from device in B (integrated from 50 to 300 cm^{-1}).

~3 kΩ, which is then allowed to break spontaneously[49]. While the atomic-scale details of each gap are different, gaps with measurable tunneling currents are formed routinely with high yield, and recent advances in *in situ* electron microscopy[61, 62] do, in principle, permit detailed structural examinations of the resulting electrodes. The migration and subsequent electrical measurements are performed *in situ* on the sample stage of the Raman measurement system, in air at room temperature.

3.3 Measurement Setup

Electrical contact to the junction under test is made via micropositionable probes. One digital lock-in amplifier (SRS SR830) is used to source 100 mV RMS at 200 Hz onto one pad, while the other pad is connected to a current-to-voltage converter (either SRS SR570 or Keithley 482). The AC current ($\propto dI/dV$) and its second harmonic ($\propto d^2I/dV^2$) are measured with lock-in amplifiers, while the DC component of the current is sampled at 5.0 kHz. The unusually large AC bias (much larger than necessary to measure differential conductance alone) is required because of an unanticipated complication: the illuminated, molecule-decorated nanogaps can also exhibit significant DC photocurrents due to optical rectification (See Chapter 6). The large AC bias is needed so that the AC current is detectable without the DC current signal overloading the lock-in input stages. We find no evidence that the 100 mV RMS AC bias degrades the nanogap or the assembled molecules.

Optical measurements are performed using a WITec CRM 200 scanning confocal Raman microscope in reflection mode. Devices are illuminated by a 785 nm diode laser at normal incidence with a diffraction-limited spot. A 100× ultra-long working distance objective leaves sufficient room for the micromanipulated electrical probes to be inserted between the objective and sample.

Initially, spatial maps of the underlying Si of unmigrated nanogaps are obtained to facilitate centering of the Raman microscope over the nanogap to within 100 nm. Spatial maps of the integrated pMA Raman signal after electromigration demonstrate the localization of the SERS hotspot (3.2D,E). Raman spectra are taken with 1 s or 2 s integration times while the microscope objective is held fixed over the migrated junctions.

3.4 Evolution of SERS Response during and after electromigration

When the conductance of the junction drops below the conductance quantum, $G_0 \equiv 2e^2/h$, a tunneling gap is formed, and simultaneous conductance and Raman measurements are performed. *In situ* measurements of the optical response of nanogaps during migration are presented in Fig. 3.3. Even prior to complete nanogap formation, partially electromigrated junctions show SERS enhancement of pMA once the resistance exceeds about 1 kΩ. The appearance of SERS indicates that the local interelectrode plasmon modes are now excitable. Crudely, this implies that over an optical cycle the junction acts more like a capacitor than a resistor; that is, the RC time constant of the nanogap is comparable to one optical period. For a 1 kΩ nanogap illuminated at 785 nm this implies an effective nanogap capacitance at optical frequencies on the order of tens of attofarads.

The measured Raman signal strength scales logarithmically with the resistance of the gap until resistances exceed 1-10 MΩ. At higher gap resistances, the Raman signal takes on a roughly constant value with sporadic changes (corresponding to SERS blinking events). This decoupling of electronic transport and SERS at low conduc-
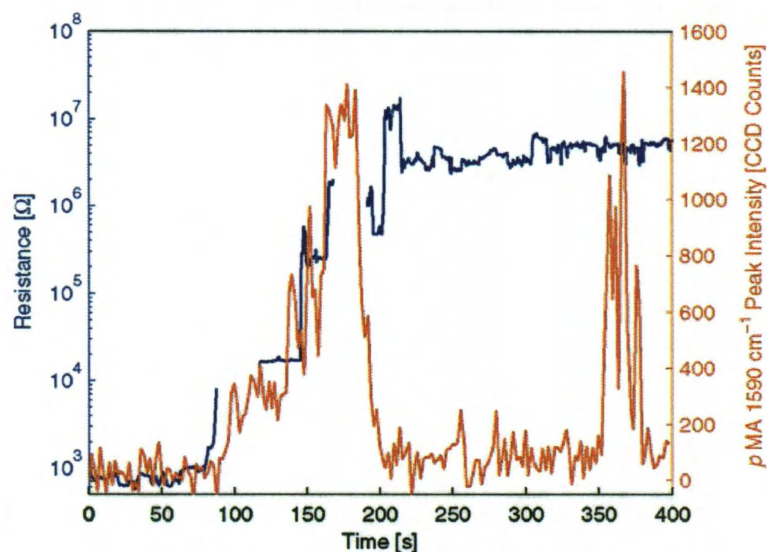
Figure 3.3 : Blue curve (left scale): Resistance as a function of time for a nanogap as it is migrated. Migration is complete when the resistance reaches ~13 k$\Omega \approx (1/G_0)$. Breaks in the curve occur where the gain of the current amplifier was being changed to maintain signal. Red curve (right scale): CCD counts per second in the 1590 cm^{-1} peak (integrated from 1550 to 1650 cm^{-1}) as a function of time for the same device (synchronized with resistance plot). The intensity of the peak increases linearly with the log of the resistance until the resistance reaches around 10$^6\Omega$, at which point the intensity drops significantly and no longer shows correlations with the resistance. Stochastic intensity fluctuations ("blinking") are observed beyond this point.

tances is not surprising *a priori*, since tunneling conductances vary exponentially with gap size, while local plasmonic structure is less sensitive. Blinking events are often not correlated with further changes in junction resistance. This means that molecules are present in a region of strong Raman enhancement, while the molecular-scale tunneling volume dominating interelectrode conductance does not contain molecules that are detectably contributing to the Raman signal.

3.5 Correlated Electrical Conductance and Raman Response

In 17 of 120 junctions using pMA and 4 out of 70 junctions using FOPE, there are strong temporal correlations between the fluctuations in the nanogap conductance and changes in the SERS spectrum. This yield is quantitatively consistent with the yield of tunneling gaps containing single molecules inferred in single-molecule transistor measurements. Examples are shown in Figures 3.4, 3.5, and 3.6. In Figure 3.4A a simple positive correlation between Raman intensity and dI/dV is observed for all Raman modes. In Figure 3.4B another positive correlation between Raman intensity and differential conductance is observed in a different junction. In this case spectral diffusion of the Raman lines occurs but does not correlate significantly with the conduction. In both parts A and B of Fig. 3.4, the amplitudes (count rates) of strong Raman modes have similar relative changes as the differential conductance.

Figure 3.5 is an example of a more complicated relationship between the conductance and the SERS spectrum. While sudden changes in the Raman spectrum are correlated in time with changes in the measured conductance, some increases in Raman intensity correlate with increased conductance, while others correlate with decreases in conductance. Additionally, changes in the mode structure of the Raman spectrum clearly correlate with changes in conductance. In region A the Raman
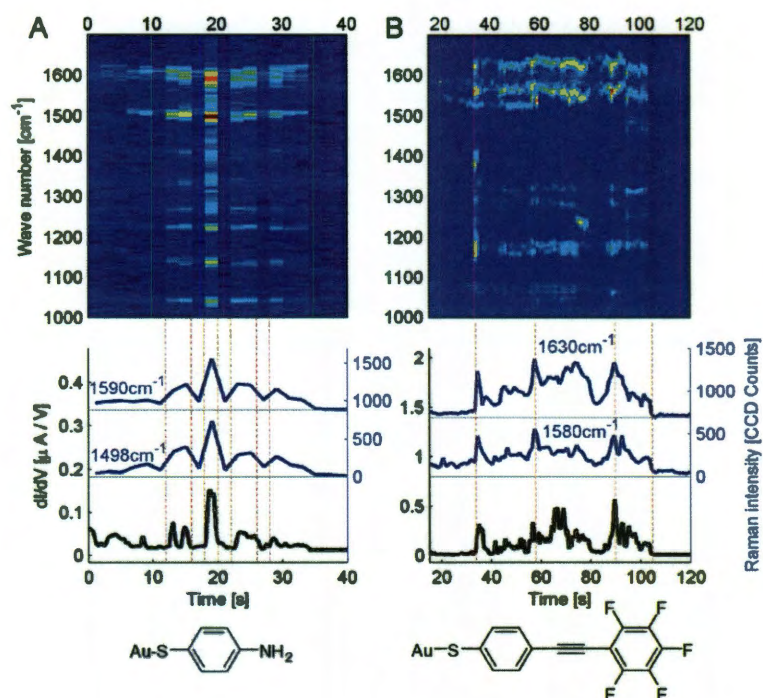
Figure 3.4 : A) Waterfall plot of Raman spectrum (2 s integrations) and positively correlated differential conductance measurements (dark blue = 50 counts; dark red = 160 counts) for a pMA sample. All Raman modes that are visible exhibit this behavior as illustrated by the 1498 and 1590 cm^{-1} modes. The 1590 cm^{-1} mode has been shifted upward on the lower graph with the gray line indicating zero CCD counts. Vertical red lines indicate points of rapidly changing Raman intensity and conduction. Structure of pMA after self-assembly onto Au is shown below. B) Waterfall plot of Raman spectrum (1 s integrations) and positively correlated conductance measurement for a FOPE sample (dark blue = 0 counts; dark red = 250 counts). Strong spectral wondering is observed with no correlation to changes in conductance. Both visible modes at 1580 and 1630 cm^{-1} are positively correlated. The slower response of the Raman spectrum compared to the conductance is due to the relatively long integration time. The 1630 cm^{-1} mode has been shifted upward on the lower graph for clarity. Structure of FOPE after self-assembly onto Au is shown below.
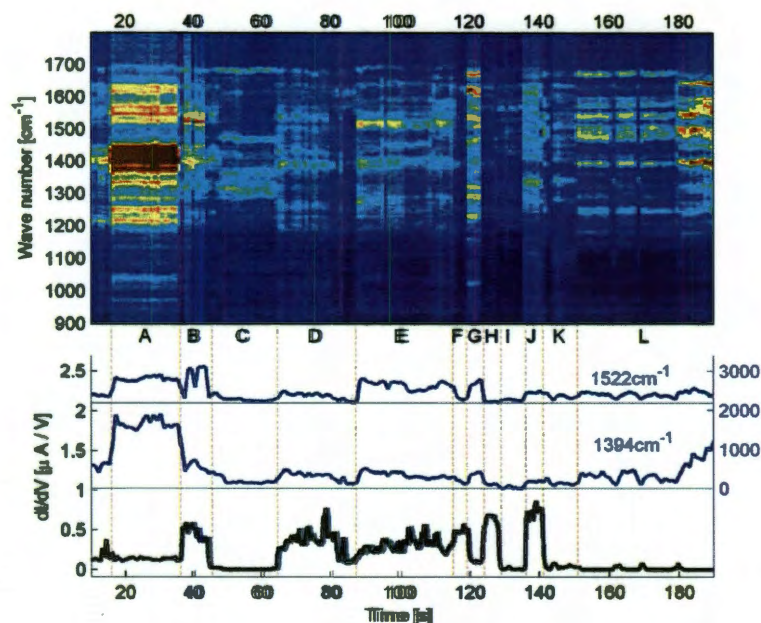
Figure 3.5 : Waterfall plot of Raman spectrum (1 s integrations) and conduction measurements for a pMA sample. The device experiences periods of correlation (regions B, D, E) and anticorrelation (region L) between Raman intensity and conduction. Distinct changes in conduction are observed with every significant change in the Raman spectrum and are indicated by vertical red lines. The modes near 1394 and 1522 cm^{-1} show similar intensity fluctuations except at region B and the end of region L. The color scale (dark blue = 20 counts; dark red = 200 counts) has been set to make as many Raman modes visible as possible. This results in the saturation of the signal at region A which would otherwise resolve into well-defined peaks. The 1522 cm^{-1} mode has been shifted upward on the lower graph for clarity.

spectrum and conductance are constant; when the Raman spectrum changes in region B a three-fold increase in conductance is observed, though overall Raman intensity changes only for certain modes. In region C the spectrum changes yet again, and while a weaker Raman spectrum remains, the conduction drops significantly. In region D the same mode structure seen in B returns and the conduction is similar to that seen in B as well. Regions D and E have positive correlations between Raman intensity and conduction with the lowest conduction observed between D and E where the Raman intensity is also lowest. At F a switch from positive to negative correlation between the Raman intensity and conduction occurs and carries over to regions G and H. At region I a small change in the mode structure is observed correlating with a switch to positive intensity-conduction correlations, continuing through regions J and K. In region L there is a final change in mode structure resulting in negative intensity-conduction correlations exemplified in the three conduction spikes that occur when the Raman spectrum disappears.

An interesting example of a more complicated correlated SERS time spectrum and conductance measurement for a FOPE device is presented in Fig. 3.6. The temporal correlations between SERS and conduction are clear. In region A we observe a stable Raman spectrum and small conductance changes which appear to be correlated with changes in the Raman mode at 1980 cm^{-1}. After a short spike in conductance the conductance and Raman disappear at B. In section C the conductance and Raman spectrum return. This time the conductance is $6\times$ larger than in A and the Raman modes are different. In particular the mode previously seen at 1980 cm^{-1} is now at 1933 cm^{-1}. In region D we see the conductance drop to levels closer to those seen at A and the 1933 cm^{-1} mode from C shifts to 2038 cm^{-1}. During D we see that the conductance momentarily returns to the value seen in section C correlated with a

shift in the 2038 cm^{-1} mode back to 1933 cm^{-1}. In section E we see another shift in position of the 1933 cm^{-1} mode to 2098 cm^{-1} which slowly shifts up to 2122 cm^{-1}. During E the Raman spectrum is seem to once again disappear correlated with a drop in conductivity briefly and the return simultaneously. Finally in F we see the spectrum disappear a final time again correlated with a drop in conductivity. In the bulk Raman spectrum the FOPE molecule only shows one mode above 1700 cm^{-1}, the C$\equiv$C stretch mode at 2228 cm^{-1} associated with the triple bond connecting the two phenylene rings. It is likely that the mode at 2122 cm^{-1} is a manifestation to the 2228 cm^{-1} mode. This mode frequently appears when studying the FOPE devices and is absent in control experiments with pMA or contaminants from the air. The large shift in wave numbers (over 100 cm^{-1} between the bulk and normal and almost 300 cm^{-1} for the greatest shift) indicates significant interactions between the molecule and either the substrate or other adsorbates, and is cause for further investigation.

It should be noted that our spectra are typically dominated by the b_2 symmetry modes of pMA[35], as was seen previously[5]. This is not surprising, as it is well accepted that b_2 symmetry modes experience additional "chemical" enhancements in comparison to a_1 symmetry modes. We often only observe the 1590 cm^{-1} a_1 symmetry peak and not the other expected a_1 mode at 1077 cm^{-1}. Strong spectral diffusion with shifts as large as ± 20 cm^{-1} have also been observed. This surely limits direct comparison to spectra reported elsewhere. However, the measured spectra are quite consistent with one another and are qualitatively different than those seen in "bare" junctions contaminated by physisorbed exogenous carbon[5].

One possible concern could be that changes in metal configuration at the junction are responsible for the fluctuations in tunneling conductance and SERS intensity. This scenario is unlikely for several reasons. First, tunneling conductances depend
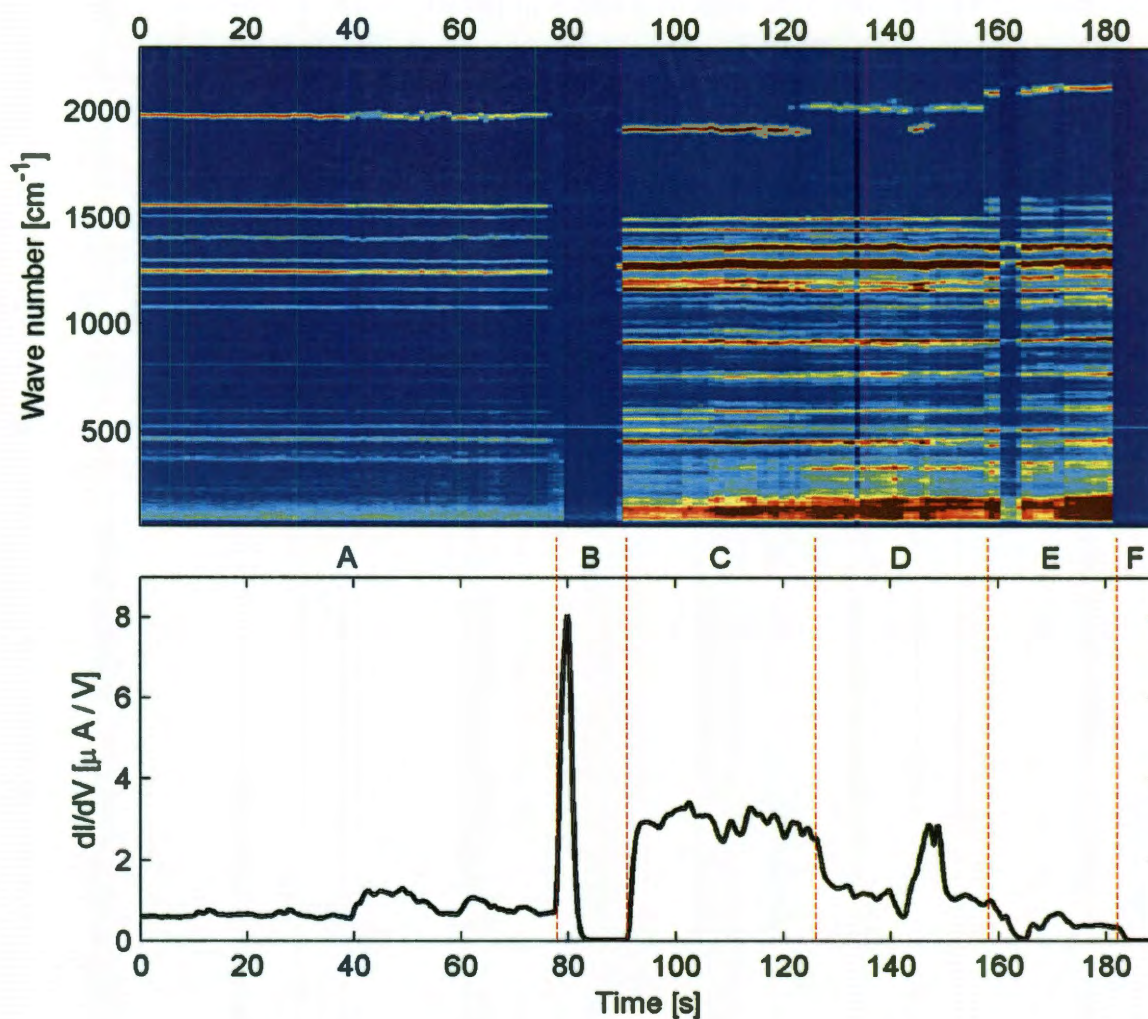
Figure 3.6 : Waterfall plot of Raman spectrum (1 s integrations) and correlated conductance measurements for a single FOPE molecule. The Raman mode observed between 1950 and 2122 cm^{-1} is believed to be for the same 2122 cm^{-1} mode associated with the C≡C stretch of the FOPE molecule. The large spectral shifts observed fro this mode are attributed to interactions between the molecule and its nanogap environment. Clear correlations between teh Raman structure and conductance can be seen. In particular in region B and for part of region E the Raman spectrum is observed to disappear while the conductance drops to zero. Between different regions distanct changes in the Raman spectrum are observed during clear change in conductivity.

exponentially on gap geometry; while dI/dV could change by a factor of ten for a 0.1 nm change in gap separation, it is very unlikely that the electromagnetic enhancement would be as strongly affected. Second, it is not clear how metal rearrangement could explain the observed changes in Figure 3.5; this would require that the gap itself alternately grow and shrink, with some changes in metal geometry giving large dI/dV features with small Raman effects and others vice versa. Finally, during the events in Figures 3.4 and 3.5, the continuum emission at low wavenumbers observed previously due to Raman scattering from conduction electrons in the metal electrodes[5] is constant in time.

The continuum emission is present in junctions without molecules. Note that in devices with molecules, in extremely strong SERS blinks (brief periods of strong Raman emission), some increase in emission at low wavenumbers does occur, though this is much more modest than the percentage changes seen molecule-specific Raman modes. Figures 3.7 and 3.8 are reproductions of the Raman data from Figures 3.4 and 3.5 but with the conductance as a function of time plotted in comparison to the integrated continuum emission (70-100 cm^{-1}). During the major conductance changes and Raman blinking events, the continuum emission changes much less than either the SERS intensity or the conductance. This strongly suggests that the metal configuration at the junction is not changing in time; rather, the changes in SERS intensity and conductance are therefore due to changes in the molecular position, orientation, and chemical environment.

3.6 Laser Heating

On possible cause of changes in the nanogap structure is laser heating. We performed electrical measurements on unbroken constrictions under various illumination condi-
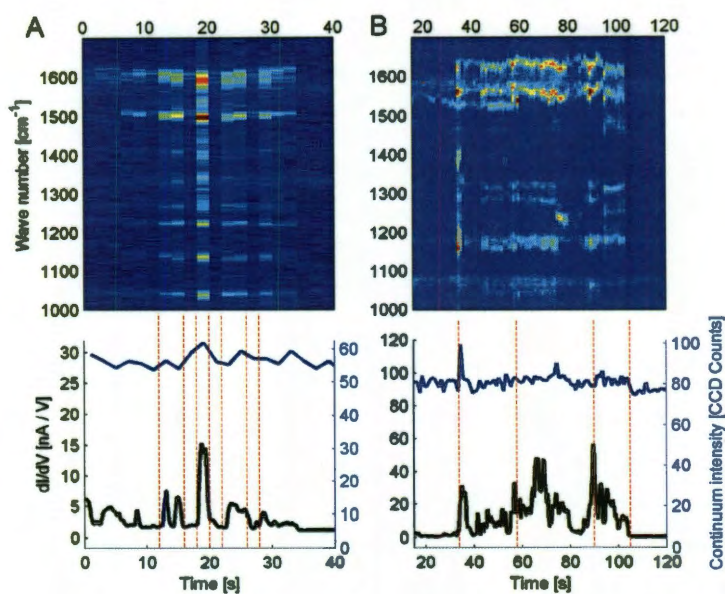
Figure 3.7 : Reproduction of Figure 3.4. Here the low wavenumber continuum intensity (integrated from 70-100 cm^{-1}) is plotted as a function of time. In both A and B the continuum is observed to be relatively constant with fluctuations much smaller than those seen in the Raman modes.
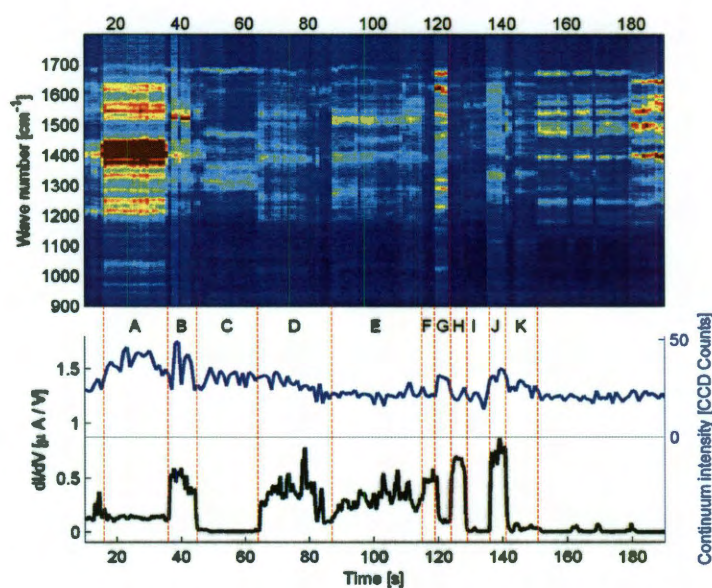
Figure 3.8 : Reproduction of Figure 3.4. Here the low wavenumber continuum intensity (integrated from 70-100 cm^{-1}) is plotted as a function of time. The continuum shows little correlation with the overall conduction especially when compared with the strong correlation exhibited by the active Raman modes. The observed jumps in continuum typically correspond with times when the background of the entire spectrum is elevated relative to very high wave numbers (> 3000 cm^{-1}). This could be the result of continuum generation from the molecule.

tions demonstrate that heating of the electrodes due to the laser is not significant. The inferred change in the electrode temperature at $\sim$0.5 mW laser power was less than 2 K.

To determine the effects of laser heating on nanogaps, unbroken constrictions were illuminated with various laser powers while the resistance was measured as seen in Figure 3.9A. To determine the laser power we measured the number of CCD counts per second in the Si 520 cm^{-1} peak. At higher laser powers irreversible changes to the constriction occur as evident in the dropping resistance of the constriction when the laser power is held constant. We do not believe that such changes in the constriction will dramatically change our estimate of the laser heating. These laser powers are much higher than used in our conduction experiment where we expect about 50 CCD counts per second in the Si peak. From our measurements we determined the resistance of the constriction as a function of laser power as shown in Figure 3.9B using a linear least-squares fit. The final resistance/laser intensity relationship of $R = 1.35 \times 10^{-3} I_{\text{laser}} + 180 \ \Omega$, where R is the resistance in Ohms and I_{laser} the laser intensity in Si CCD counts/second, is based on the average of three different samples. We then took different devices from the same sample chip and heated them in a probe station while measuring their resistance, as seen in Figure 3.9C. A linear fit was performed to determine the resistance as a function of temperature this time averaging over four samples. The final relationship was determined to be $R = 0.11T + 85 \ \Omega$, where R is the resistance in Ohms and T is the temperature in Kelvin. Equating our two relationships we find that the change in temperature per CCD count in the Si peak is 0.012 K. At the laser power used in our conduction experiments (50 CCD counts/second) this lets us estimate a temperature change of 0.62 K due to illumination.
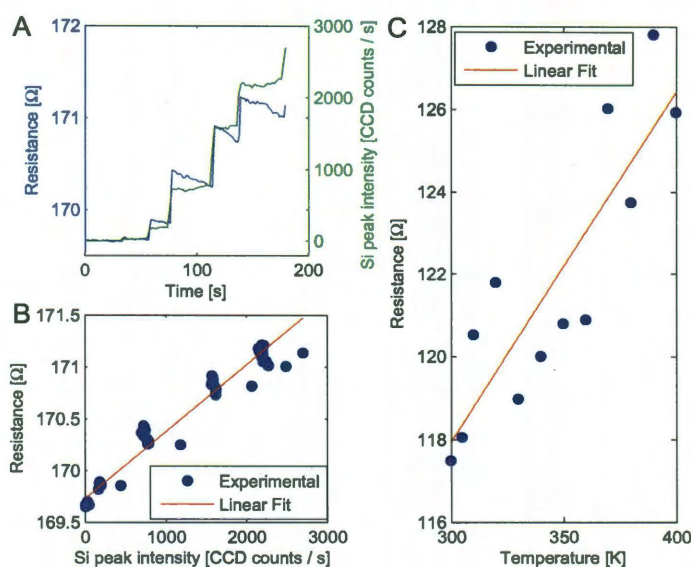
Figure 3.9 : A) Resistance and laser intensity (in Si peak CCD counts/second) for an illuminated constriction as a function of time. It is clear that the resistance scales linearly with laser power. B) Resistance as a function of laser intensity (again in Si peak CCD counts/second) for the same device as in A. The data is well represented by a linear fit of $R = 0.64 \times 10^{-3} I_{\text{laser}} + 170 \ \Omega$ where R is the resistance in Ohms and I_{laser} is the laser intensity in CCD counts/second. C) Resistance as a function of temperature for a different constriction heated in a vacuum probe station. The data is fit to the line $R = 0.085T + 92 \ \Omega$ where R is the resistance in Ohms and T is the temperature in Kelvin.

3.7 FDTD Simulations

Another concern is that changes in tunneling conduction in one part of the junction may alter the plasmon mode structure and affect Raman emission from elsewhere in the junction. Such a scenario could lead to correlations like those in Figs. 3.4 and 3.5 even if conduction and Raman emission are not from the same molecule. Given that the interelectrode conductance affects Raman emission (Fig. 3.3), it is important to consider this possibility. We have performed finite-difference time domain (FDTD) simulations of the optical properties of such junctions to assess this issue, and the results (*vide infra*) effectively rule out this concern. While the finite grid size (1 nm) required for practical computation times restricts the quantitative accuracy of these calculations, the main results regarding spatial mode structure and wavelength dependence are robust, and the calculated electric field enhancements are an *underestimate*[58, 5].

Figure 3.10 shows a comparison of calculated extinction spectra that characterize the plasmonic mode structure of the gap structure shown, for various values of interelectrode conductance connecting the source and drain at the indicated point. The mode structure and enhancement are *unaffected* by conductances smaller than a few G_0. These calculations confirm the interpretation given above for Fig. 3.3: The plasmonic mode structure responsible for enhanced local fields in the nanogap is established once the interelectrode conductance falls well below G_0. Given these FDTD results, the only plausible explanation for such strong correlations in time between conduction and Raman emission is that both processes involve the same molecule or molecules.
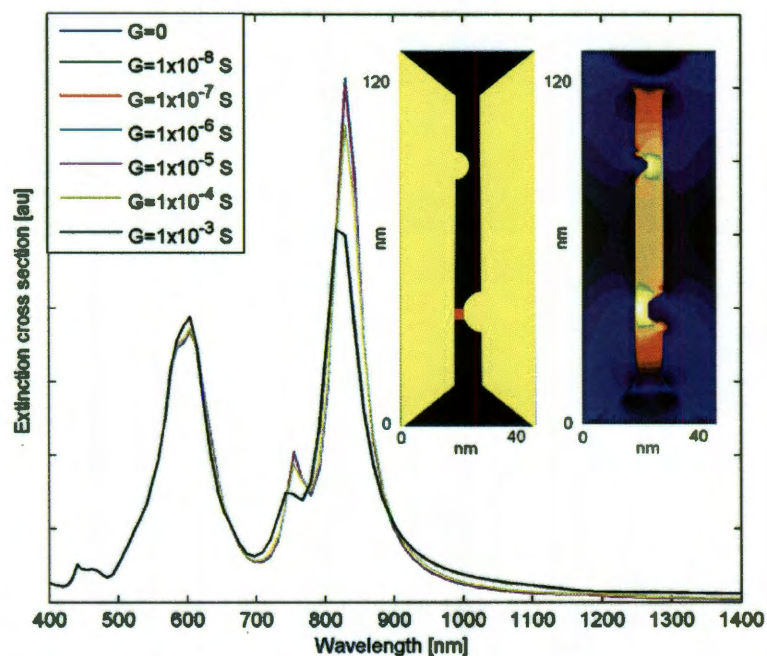
Figure 3.10 : Extinction spectrum calculated using a 1 nm grid size for the structure partially shown in the left inset. The electrodes are modeled as Au, 15 nm thick, sitting on 50 nm thick SiO2 dielectric, with an overall interelectrode gap of 8 nm. The upper and lower protrusions into that gap shown are modeled as hemispheres of radii 4 and 6 nm, respectively. The red square indicates the location of the modeled interelectrode conductance (a volume 2 nm on a side, meant to represent a molecule at the interelectrode gap). The right inset shows a map of $|E|^4$, where E is the local electric field normalized by the magnitude of the incident field (roughly the Raman enhancement factor), for the mode near 825 nm. White corresponds to an enhancement of 10^9. This field map is essentially unchanged until the junction conductance approachs 10^{-4} S $\sim G_0$.

3.8 Conclusion

Conduction in nanogaps is known to be dominated by a tiny volume inferred in single molecule transport and break junction experiments to contain often only one molecule. Molecular movement, changes in bonding, or reorientation of the molecule in the gap results in different tunneling configurations and hence in conductance changes. The complex relationship between conductance and Raman mode structure and intensity is also then natural, since chemical enhancement effects and the appearance of broken symmetry b_2 modes should be strongly affected by changes in molecular configuration on the metal surface. It should also be noted that the measured junction conductances are consistent with the expected molecular conductance range of 10^{-3} to 10^{-4} G_0 measured in a similar molecule by break junction techniques[10].

The detailed SERS mode structure combined with the conductance contains a wealth of information about the bonding, orientation, and local environment of the molecule. With appropriate electronic structure calculations and theoretical estimates of the Raman tensor for candidate molecule/metal configurations, it should be possible to infer likely junction geometries and chemical structure corresponding to each type of Raman spectrum. Such calculations are very challenging even for the conductance distribution alone[63].

These conductance/Raman observations and accompanying calculations demonstrate that electromigrated nanogaps between extended electrodes can achieve enhancements sufficient for single-molecule SERS sensitivity. Given that these structures can be fabricated in a scaleable manner in predefined locations with high yields[5], this may allow significant advances in SERS-based sensing as well as multimodal sensing.

This technique will serve as the basis for future measurements in vacuum as a

function of temperature, interelectrode bias, and gate voltage. It will be possible to address open fundamental issues in SERS, including the nature of chemical enhancement, the mechanism of blinking, and the cause of the large spectral diffusion of Raman lines. Finally as will be discussed in Chapter 7 comparisons of Stokes and anti-Stokes Raman peak intensities as a function of bias across the junction can reveal whether current flow pumps particular vibrational modes out of thermal equilibrium. This would enabling new and detailed studies of nonequilibrium physics and chemistry at the single molecule scale. Comparisons between these results and transport/Raman studies on molecular ensembles[64, 65] should also provide valuable information about the effect of molecular environment on these processes.

Chapter 4

Localized heating in nanoscale platnium constrictions measured using blackbody radiation

4.1 Introduction

In this chapter we look at the electrical heating of metallic nanoconstrictions that occurs during processes such as electromigration (Section 1.6). As discussed in the previous two chapters the resulting electromigrated electrodes are often used for studies of single-molecule electronic conduction[2, 4], with electromigration performed in the presence of molecules of interest. Because of concerns about molecular stability at elevated temperatures, there is much interest in the magnitude of Joule heating during the electromigration process. In particular, high temperatures (>600 K) can induce thermal break down in complex molecules and provide sufficient energy to remove weakly bound molecules from the electrode surfaces. Recently the temperature in these and similar nanostructures has been assessed via the observation of melting of nanoparticles decorating the metal surface[66, 67]. However, this requires special surface preparation and high vacuum electron microscopy, and has a temperature resolution limited by the melting point range of the nanoparticles.

We investigated the heating in nanoconstrictions using a variation of thermal emission microscopy[68, 69] to infer temperature profiles in nanostructures on a length scale of approximately 1 μm. Specifically we examine Pt constrictions using blackbody radiation as a simple method to determining the local heating. The Pt nanowires

are inferred to reach very high temperatures exceeding 1000 K before the onset of electromigration. Optical measurements show good agreement with finite element modeling (FEM) of the heating process. With an appropriate infrared detection system this approach may be applied to other metals without special surface treatments. The results for Pt nanostructures indicate a significant challenge in creating Pt electromigrated gaps suitable for use in single molecule electronic devices.

4.2   Sample Fabrication

Platinum nanowires consisting of 1 nm Ti and 15 nm Pt with widths of approximately 140 nm and lengths ranging from 200 nm to 1200 nm were fabricated using the e-beam lithography as per Section 1.7. Each nanowire was connected via 6 μm wide wires to large contact pads for electrical probing. A typical device is picture in the inset to Figure 4.1.

4.3   Measurements

The blackbody spectrum of heated Pt nanowires was measured in air at room temperature in a confocal Raman microscope with a silicon CCD detector. Samples were heated *in-situ* by applying a bias across the sample using electrical probes. The microscope was aligned over the nanowire structure by positioning the Raman laser spot over the center of the nanowire. Blackbody spectra were collected at fixed bias values with the laser off. Each spectrum was measured by averaging two 15 s integrations. Spatial mappings of the light emission were also acquired by rastering the stage with the nanowire under the microscope. Spatial map spectra were integrated for one to two seconds at each position. Additional spatial maps were taken while using the 785 nm laser to measure the Raman response of the Si substrate. The strong

520 cm^{-1} Si Raman peak is attenuated when the Pt film is over the Si substrate, allowing the physical layout of the nanowire to be determined from the map of the Si peak intensity. The combined Raman/blackbody measurements allow us to map the location of the light emission to the physical position along the wire.

The absolute temperature of the nanowires was determined by fitting the measured spectra to theoretical blackbody emittance per wavelength of the form $M = \frac{2\pi c}{\lambda^4 (e^{\frac{hc}{\lambda kT}} - 1)}$ where M has units of photons/(cm^2-s-μm). The efficiency of the Si CCD in our microscope drops off rapidly at wavelengths exceeding 1 μm. To account for this loss of efficiency the output of the CCD was calibrated using a known 2960 K blackbody source. The blackbody source was imaged by diffusing the source's light with spectralon glass and imaging the surface of the glass. This ensures that the calibration takes into consideration all the losses of the optics along with the CCD efficiency.

Figure 4.1 shows the measured blackbody spectrum after correction for a Pt wire device 1030 nm long and 180 nm wide at different bias voltages. Approximately half the applied voltage is dropped across the wire with the rest dropped in the connections from the contact pads to the wire. The current at 1.90 V was 3.44 mA yielding a current density of 1.3×10^{12} A/m^2. The temperature at the center of each wire is determined by fitting the calibration-corrected spectrum measured at the center of the wire to a perfect blackbody spectrum. The fit has two free parameters, temperature and amplitude; the latter is a measure of how efficiently the microscope can gather and detect photons. Fits are performed over the wavelength range of 650 nm to 950 nm with the region from 770 nm to 805 nm removed to avoid the spectral region affected by the 785 nm holographic beam splitter used for Raman measurements. Due to the exponential decrease in photon counts as temperature is reduced, fits for temperatures below 900 K yield increasingly poor results due to
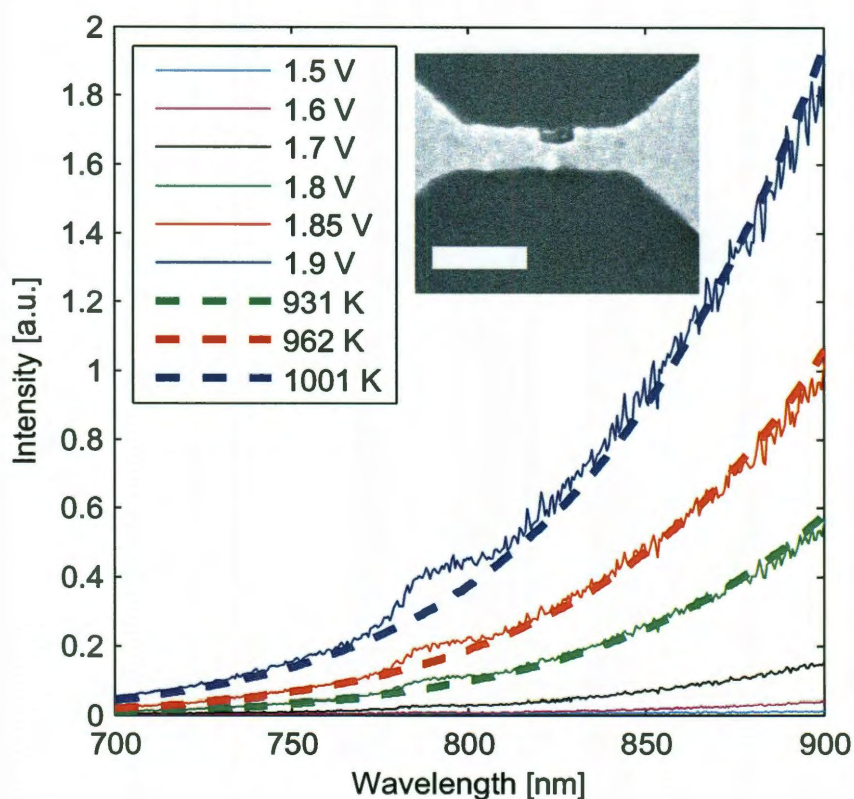
Figure 4.1 : Observed light emission after calibration correction from a 1030 nm long 180 nm wide Pt bowtie at various biases. The three dashed lines indicate theoretical blackbody curves at 931 K, 963 K, and 1001 K which show good agreement with the measurements at 1.80 V (3.32 mA), 1.85 V (3.38 mA) and 1.90 V (3.44 mA) applied bias (current), respectively. Inset: SEM image of a typical Pt wire constriction, 530 nm long and 140 nm wide. The notch in the middel of the wire is the result of partially completed electromigration. In this device current flow was from left to right.

inadequate signal-to-noise. For instance in Figure 4.1B, for temperatures less than 900 K the signal-to-noise ratio is less than one. To assist in analysis we fit the data obtained at the highest voltage first, and then fix the amplitude parameter in fits for the same wire at lower biases. This is a valid method as the amplitude is a measure of the optical system's transmission efficiency and should remain constant as long as the microscope's configuration and sample position in the focal region remain unchanged.

4.4   FEM Simulations

We performed FEM simulations using commercially available software (COMSOL) to verify our results. We model the Pt film using the same dimensions as the actual wires but omitting the large contact pads as they do not provide significant heating due to their relatively low resistance. The contact pads also do not contribute significantly to heat dissipation as verified in our model. The substrate was modeled as 200 nm of thermal oxide on top of a 2 μm thick Si slab, the bottom of which is assumed to be held fixed at room temperature. The substrate thickness was chosen for computational efficiency; we verified that increasing the thickness from 2 um to 5 um or more has no effect on the heating of the wire. Finally where appropriate we model heat transfer from the Pt wire into the surrounding air by modeling the heat transfer coefficient of the film to air to be 5 W/(m^2 K). Bulk values are used for all thermal conductivities and for the electrical properties of the oxide and substrate. We experimentally measured the resistivity of our 15 nm Pt films using the Van der Pauw technique. Additionally we measured the linear temperature dependence of the resistivity from 200 K to 400 K. We experimentally found the resistivity to be $3.9 \times 10^{-7}\Omega$ m and the temperature coefficient α to be 7.19×10^{-4} 1/K where α is defined in the resistivity (ρ) equation $\rho(T) = \rho_{T=T_0}(1 + \alpha(T - T_0))$. For each simu-
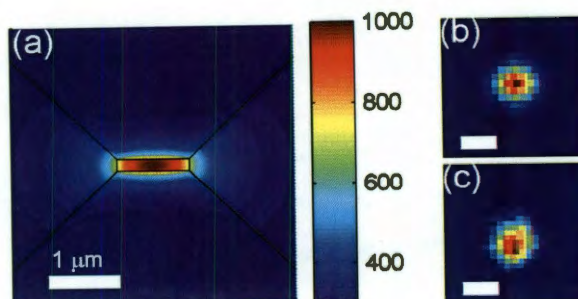
Figure 4.2 : A) Finite element model of temperature profile in a Pt bowtie 1030 nm long and 180 nm wide with a bias of 1.90 V. Heating has clearly been localized to the nanowire region. B) Calculated light emission intensity from modeled bowtie based upon integrated emission from 650 nm to 950 nm assuming a gaussian sensing profile of FWHM 800 nm. Scale bar indicates 1 μm. Color scale ranges from blue (zero intensity) to red (highest intensity). C) Experimentally measured light emission intensity from bowtie. The shape and extent of emission matches predicted emission well. Scale bar indicates 1 μm. Color scale ranges from blue (zero intensity) to red (highest intensity).

lation we record the temperature at the center of the wire at the same sample biases used in our experiment.

Experimental measurements correlate well with the FEM model. Figure 4.2A is the modeled temperature profile for an actual device. Figure 4.2B is a spatial map of the expected integrated emission intensity from 650 nm to 1.00 μm. The emission map is in good agreement with the measured emission for this device as seen in Figure 4.2C. The highest temperatures reported in the model are in agreement with our measured values as shown for two devices in Figures 4.3A, B.

Small deviations between the experimental and model temperatures may also be the result of the convolution of the microscope's sampling area and the true temperature profile. We have measured the spatial sensitivity of our microscope, and it can be well approximated by a Gaussian profile with a FWHM of approximately 500 nm.
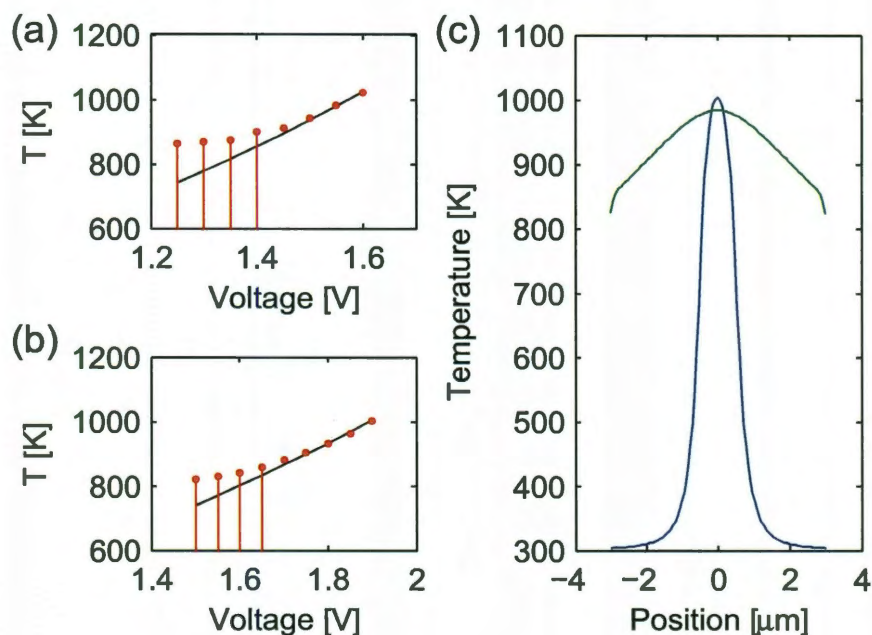
Figure 4.3 : A & B) Inferred temperature (red points) of 680 nm long 140 nm wide and 1030 nm long 180 nm wide Pt wires as a function of applied bias. Error bars indicate 95% confidence interval determined via χ^2 analysis. For lower voltages the temperature can not be experimentally determined. Black lines are simulated temperatures based upon FEM. Inferred and simulated temperatures differ at low temperatures due to the small signal to noise ratio in experimental measurements. C) FEM-based comparison of the true temperature (blue line) at a given point in 1030 nm long Pt wire biased with 1.90 V versus what the observed temperature (green line) would be based upon the convolution of the 800 nm FWHM microscope sensitivity. At each spatial coordinate the resulting spectrum is least-squares curve fit in amplitude and temperature to detemine the observed temperature.

Figure 4.3C is a 1D calculation to find the effective temperature one would expect to measure at each point along a 1030 nm long Pt wire based upon our sensitivity profile. The effective temperature is based upon fitting a blackbody spectrum to the sum of the blackbody spectra from each wire element multiplied by the microscope sensitivity at that element. It should be noted that the actual spectral amplitude drops off significantly when measured off center, as observed in Fig. 4.2B, but the relative wavelength dependence, which allows determination of the temperature, is unaffected. This is beneficial as it makes the measured temperature insensitive to small instrumental shifts away from the wire center. However, these point spread effects also mean the true highest temperature is never measured directly.

The temperatures reached during electromigration in Pt wires are considerably higher than those observed for Au wires[66]. This is sensible, since the refractory nature of Pt would lead one to expect that higher voltages would be required for migration. The comparatively extreme temperatures measured are likely too high for making molecular electronic devices without damaging the molecule. We modeled three possible electromigration scenarios: in air at room temperature, in vacuum at room temperature, and in vacuum with the substrate cooled to 80 K. For the 1030 nm long wire at 1.90 V little change is observed regardless of conditions. Air cooling provides only a small temperature drop from 1004 K to 1001 K. Cooling the substrate has more effect but only reduces the final temperature to 905 K, still above the thermal decomposition threshhold of many organic compounds.

4.5 Conclusion

We note that recent measurements of blackbody emission from Pt nanowire structures with larger aspect ratios have shown evidence of interesting coherence effects.

These include strong polarization of emitted light[70] and pronounced interference effects[71]. We see no evidence for such effects in our structures over the wavelength range examined, with no detectable net polarization of the emitted radiation. This difference likely arises in part because the nanoconstrictions act more like point-like emitters than line-like emitters due to their highly nonuniform temperature profiles.

By standard optical measurement techniques we have used emitted blackbody radiation to characterize the temperature distribution in Pt nanowires before and during the electromigration process. This approach requires no surface treatments or ultra high vacuum equipment, and with suitable infrared optics and detectors may be extended to lower temperatures. We find that the maximum temperatures obtained in Pt nanowires can exceed the decomposition threshold of many organic compounds, reinforcing that care must be taken when using electromigration with molecules in place to fabricate structures for single-molecule electronic measurements.

One implication of this work is that inorder to make Pt nanogap stuctures for SERS we need a fabrication technique that does not require electromigration. One such technique will be discussed in the next chapter.

Chapter 5

Scalable nanogap device fabrication and geometry optimization

5.1   Introduction

In chapters two and three the dimensions of the nanowires used to create molecular nanojunctions were limited to nanowire widths that are easily electromigrated. We empirically determined that nanowires 120 to 150 nm give the best combination of optical response and easy of electromigration. Wider wires are much more difficult to electromigrate resulting in very poor yields of working devices and narrower wires had poor SERS enhancements. In this chapter we discuss an alternative self-aligned fabrication method that uses two lithography steps but does not require electromigration to form nanojunctions. Consequently we are able to select any wire width we desire. In order to optimize the device geometry for maximum electric field enhancement we performed finite element method (FEM) modeling of a simplified nanojunction geometry to determine the optimal nanowire width.

A major advantage of the self-aligned fabrication method is that it can be performed entirely with photolithography making it an ideal candidate for creating SERS substrates with well defined hotspots for fabrication on a massive scale.

5.2 Self-aligned Nanogap Fabrication

The self-aligned fabrication technique was originally developed to create large aspect ratio nanogaps for electrical measurements[72]. The general idea is to lithographically create the first electrode as normal, but during the metal deposition add a thin chrome layer on top. The Cr layer readily oxidizes, and swells during the oxidation process, resulting in the Cr oxide (Cr_xO_y) overhanging the edge of the other metals. The second electrode is then created lithographically with some overlap with the first electrode. When metal is deposited for the second electrode it cannot be deposited right along the edge of the first electrode because the Cr oxide acts as a shadow mask. After the second electrode is deposited, the sample is etched in a Cr etch (CR-7, Cyantek) that removes the Cr oxide and any remaining Cr, leaving behind the two electrodes with a nanogap between them. The process is illustrated in Fig. 5.1 and an SEM image of self-aligned device is shown in Fig. 5.2.

Fabrication of very small ($<$ 5 nm) nanojunctions with the self-aligned technique requires different processing parameters than those used to create large aspect ratio nanogaps. In both cases it is important to avoid electrical shorting between the two electrodes. For the micron long gaps needed for high aspect ratio gaps, this necessitates Cr film thicknesses of at least 20 nm[72]. For our much narrower nanojucntions, we found Cr film thicknesses between 10 and 12 nm to be optimal. Additionally we observed that the Cr film can alter the optical properties of the gold film. Thus, we place a Cr film (of equal thickness) on both electrodes to give uniform optical behavior across the electrodes.

The major advantage presented by the self-aligned fabrication technique is that any width nanowire can be fabricated with a nanojunction in it. This allows us to optimize the geometry for the best electric field enhancement.
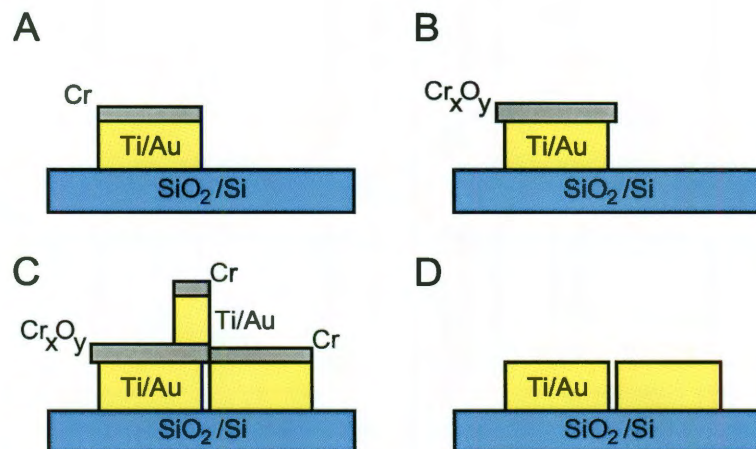
Figure 5.1 : Illustration of the self-aligned fabrication process. A) The first electrode is deposited on the substrate with a Cr cap layer. B) The Cr cap layer swells upon oxidation extending beyond the edges of the Au film underneath. C) The second electrode is deposited with some overlap with the first electrode. A Cr cap is not necessary on this electrode, but does make the optical reponse of the two electrode more uniform. D) The Cr/Cr_xO_y is etched away leaving the gold electrodes separated by a nanogap.
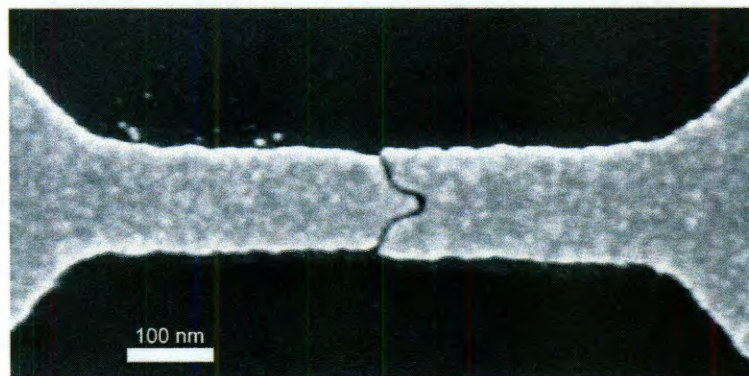
Figure 5.2 : SEM image of a self-aligned nanogap. The nanogap is approximately 5 nm wide and the nanowire is 120 nm wide. The self-aligned nanogap is largely indistinguishable from electromigrated nanogaps in the SEM.

5.3 Geometry optimization with FEM simulations

We performed FEM electrostatic simulations using COMSOL of idealized nanojunction structures to determine the optimal nanowire width as a function of wavelength. The idealized structures are shown in Fig. 5.3. One structure has a completely parallel nanogap 10 nm wide (L_{Gap}) while the other has a 50 nm wide and 5 nm long tip located on the left electrode. The nanowire of the nanojunction was 600 nm long (two 300 nm ($L_{Nanowire}$) long electrodes) with widths ($W_{Nanowire}$) ranging from 100 to 400 nm. The nanojunction was modeled as a 25 nm thick Au film with experimentally measured dielectric properties as a function of wavelength taken from reference [31]. The electrodes of the nanogap were extended back 700 nm (L_{Pad}) and the simulation is contained within a sphere of radius 1.5 μm. The film was suspended in vacuum with no substrate. The structure was illuminated with plane waves perpendicular to the plane of the film and a polarization perpendicular to the gap. The wavelength range tested was 400 nm to 1.5 μm.

For each simulation the resulting electric field distribution was calculated. Field enhancement was calculated as the normal of the resulting electric field divided by the incident plane wave electric field strength. The normal of the electric field was always taken at the center of the nanogap. For the case with the tip in the gap the center was defined as halfway between the tip and the flat edge.

Both simulated structures show strong wavelength and width dependence, as shown in Fig. 5.4. The tipped structure has electric field enhancements approximately twice as large as the tipless structure. We found that at our normal experimental wavelength of 785 nm (actually 800 nm in our simulation) the optimal nanowire width was 250 to 270 nm with electric field enhancement as a function of wire width shown in Fig. 5.5. At $\lambda = 1.0$ μm, the minimum enhancement exceeds the greatest enhance-
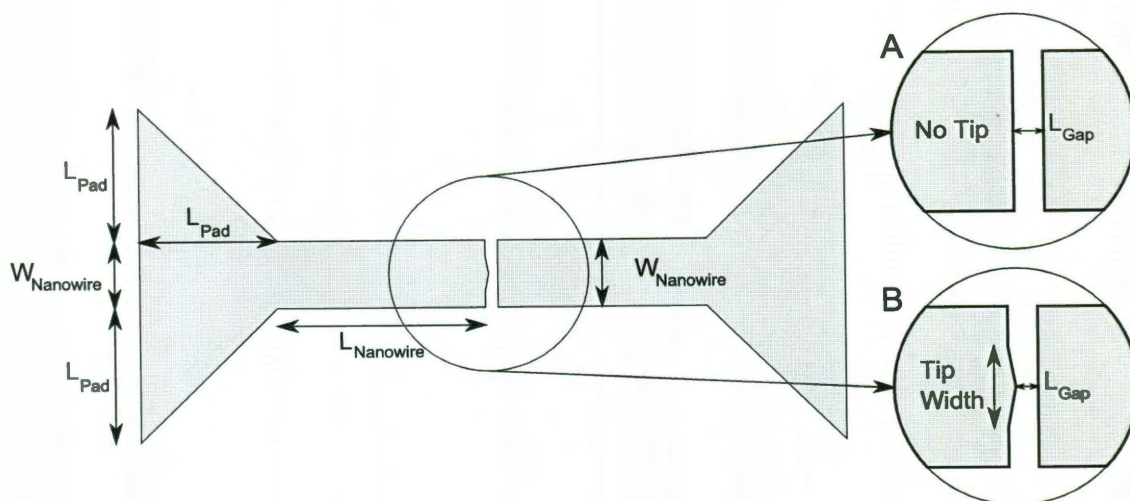
Figure 5.3 : Illustration of simulated self-aligned nanogap structures. The simulated pads were approximately twice as big as drawn. Inset A shows the tipless geometry. Inset B shows the tip geometry where the tip has a fixed width of 50 nm and height of 5 nm reducing W_{gap} to 5 nm. The incident light on the structure is parallel with the nanowire.

ment at 800 nm. The greatest enhancement for any wavelength was found to occur at $\lambda = 1.0$ μm for $W_{nanowire}$ =370 nm wide nanowires with tips. Here the enhancment exceeds 150, indicating a potential SERS enhancment of 5×10^8 consistent with our experimental observations for electromigrated nanogaps[5].

It is important to note that we do not believe that these FEM results give the true electric field enhancement for nanojunction structures; however, we do believe that the general trend of enhancement as a function of wire width is valid. The FEM models make several simplifications of true nanojunctions. First the models are perfectly symmetric with exception of the tip. Second the models all have perfectly sharp edges and corners and perfectly flat films and edges, all of which do not occur in reality. Additionally, the nanogaps modeled here are limited in size to either L_{gap} =10 or 5 nm due to computer memory constraints while meshing the models. In reality
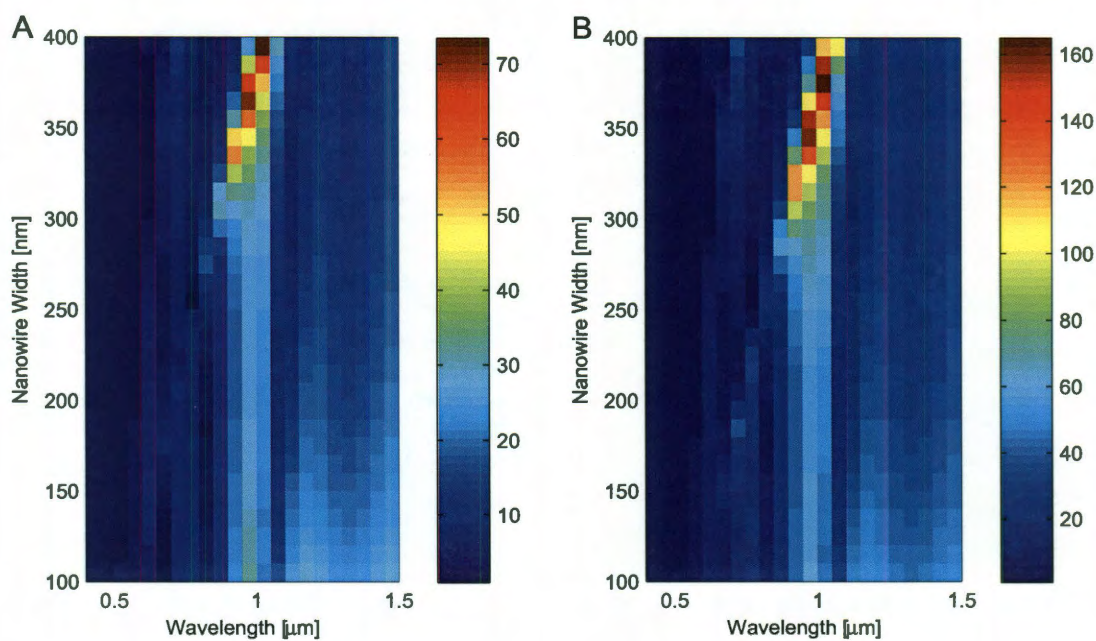
Figure 5.4 : FEM calculations of electric field enhancment as a function of nanowire width and length. A) Electric field enhancement for the tipless nanogap structure. The optimal nanowire width increases with increasing wavelength. The structure has strong electric field enhancements for all widths when the incident wavelength is 1 μm. B) Electric field enhancement for the tipped nanogap structure. The field enhancement shows similar trends to A but is twice as big.
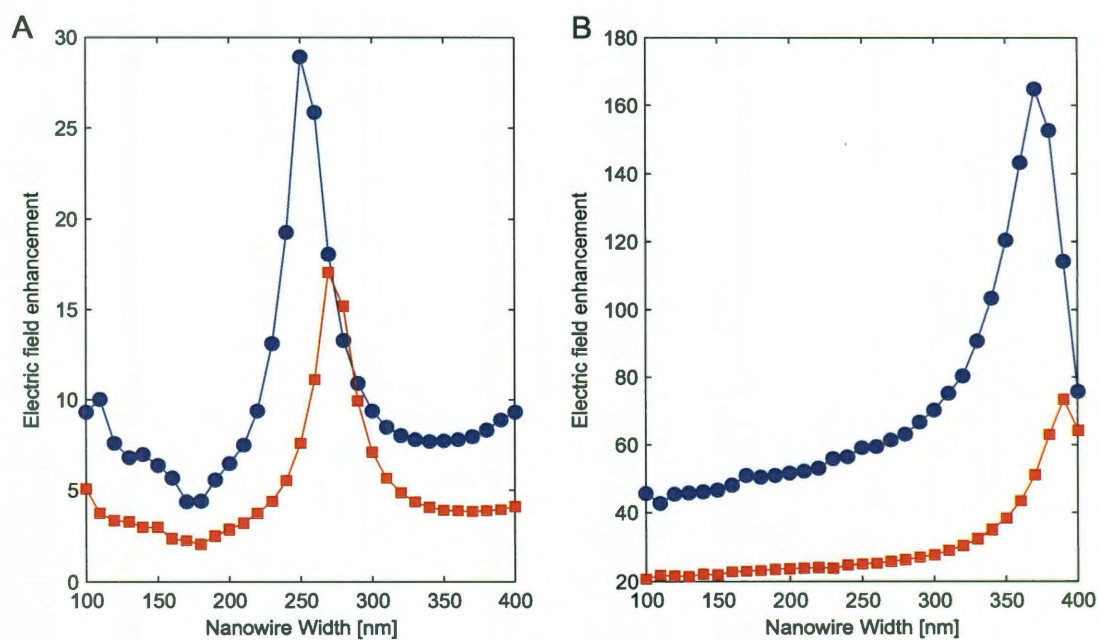
Figure 5.5 : FEM calculations of electric field enhancment as a function of nanowire width for incident wavelengths of 800 nm(A) and 1.0 μm(B). The tipless structure (red) has half the enhancement of the tipped structure (blue). For both structures we observe that adding a tip slightly reduces the optimal nanowire width. The minimum enhancement at 1.0 μm exceeds the greatest enhancement at 800 nm.

the nanojunctions we experimentally test are much smaller.

5.4 Experimental realization

We have successfully fabricated self-aligned nanogaps that can function as strong SERS substrates. Samples were fabricated using standard e-beam lithography techniques. The electrodes were formed by e-beam evaporation of 1 nm Ti, 15 nm of Au and 12 nm of Cr. Between the first and second lithography steps the sample was O_2 plasma cleaned for one minute. After lift-off in acetone samples were placed upside down in Cr etch (CR-7, Cyantek) in a sonicator. Samples were etched for 1 minute and then rinsed in multiple baths of DI water to remove any excess etchant.

The Raman response of the nanogaps was tested using the dye Nile Blue, which has a strong Raman peak at 600 cm^{-1}, dissolved in distilled water. A total of 100 μL of a 10 mM solution of Nile Blue was spin coated onto the surface at 1000 RPM for 1 minute. Afterwards the sample was spun at 4000 RPM for 10 s to remove any beaded up solution on the surface. Samples were tested in a WITec confocal Raman microscope at 785 nm. A spatial map of the Raman response of a self-aligned nanogap is shown in Fig. 5.6. Raman enhancements appear to be comparable to those observed in our earlier work with electromigrated nanogaps[5]. Time spectra taken at the center of the nanogap show less time variation than seen in electromigrated nanogaps indicating that self-aligned nanogaps are probably not single-molecule sensitive, but instead probe a few hundred molecules.

The fabrication process for making self-aligned nanogaps has proven to be extremely sensitive to the ambient conditions during the fabrication process. In particular we believe that the temperature and humidity can affect the swelling of the Cr oxide making it difficult to reproducibly fabricate sub 5 nm nanogaps without
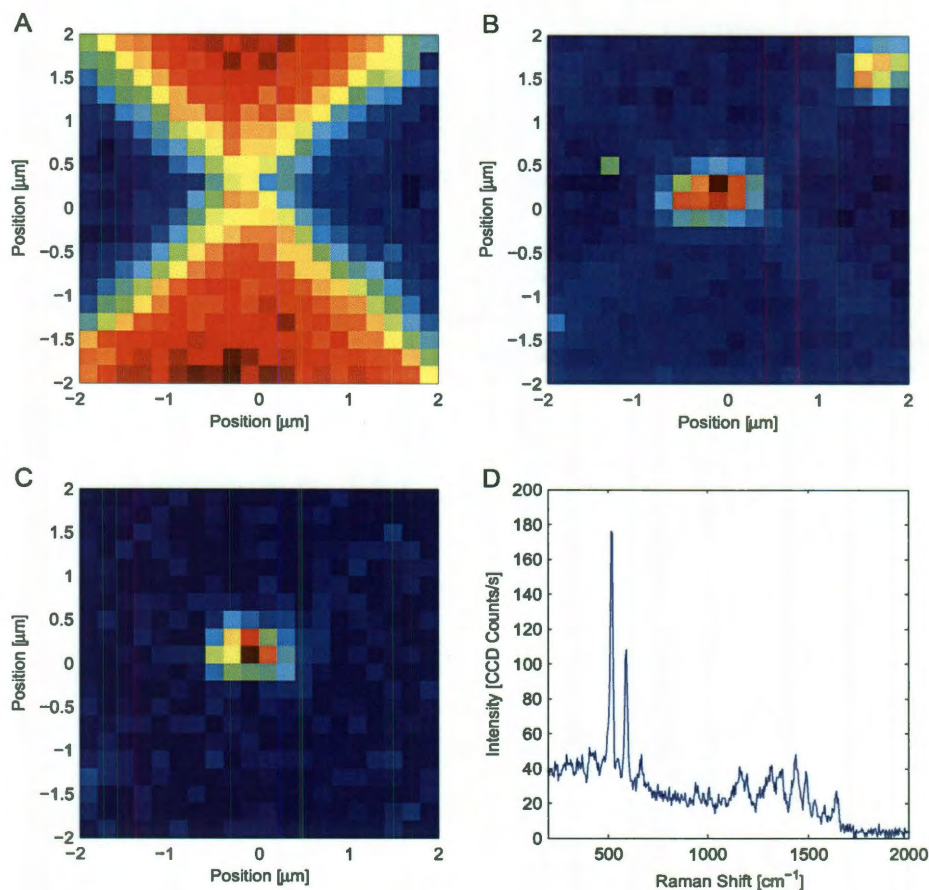
Figure 5.6 : A) Spatial map of the integrated Raman response of the Si substrate of the nanogap structure. Due to attenuation by the Au film the Si signal is weaker where the metal is. Blue indicates low intensity (presence of Au film) and red indicates high intensity (bare Si). B) Spatial map of the integrated Raman response of the continuum signal integrated from 60 to 180 cm^{-1}. As expected the continuum is strongest at the nanogap. The edges of the structure also contribute a barely perceptable continuum signal. C) Spatial map of the integrated Raman response of the 600 cm^{-1} Nile Blue Raman peak integrated from 580 to 620 cm^{-1}. The signal is clearly confined to the nanogap. D) SERS spectrum taken at the center of the nanogap with a 1 s integration time. The tallest peak is the 520 cm^{-1} Si peak. The next peak at 600 cm^{-1} is a known Nile Blue Raman peak. Additional peaks in the carbon finger print region are also present. A clear continuum signal of about 50 counts is present from the Rayleigh line to about 1700 cm^{-1}.

shorts. Due to difficulties in reproducibly fabricating self-aligned nanogaps with high SERS sensitivity we have not confirmed whether the predictions of our FEM model are valid.

5.5 Conclusion

Our FEM simulations have greatly shaped our view of how to improve the sensitivity of our nanogap structures. In the limit of the extremely small nanogaps such as those made by electromigration it is clear that nanowire width optimization in unnecessary as single molecule response can already be achieved[6]. In fact one might argue that increased electric field enhancement might reduce the stability of the system to the point of being to unstable too measure. As an optical sensor, however, nanogaps that are sensitive to multiple molecules may be more desireable. In particular, the ability to greatly reduce or eliminate spectral wandering and blinking would make chemical detection significantly easier while still being sensitive to very low concentrations of the molecule of interest. Our intial attempts at fabricating self-aligned nanogaps focused on making them as similar to electromigrated nanogaps as possible. However, our simulations make it clear that we can increase the nanowire widths to twice the normal width to improve the sensitivity, and at the same time reduce variations in fabrication, as making 250 nm wide wires is more reliable than 120 nm wide wires and requires less delicate alignment.

Some room for improvement remains. In particular simulations of the same nanogap structures under diffraction limited Gaussian illumination may be of interest. In that case a wider nanowire may be less important as the optical field is more centered over the nanogap.

Chapter 6

Optical rectification and field enhancement in a plasmonic nanogap

6.1 Introduction

In chapters 2 and 3 we observed that nanogaps make excellent SERS substrates with single molecule sensitivity. We roughly estimated the SERS enhancement to be 5×10^8 but acknowledged that this an underestimate[5, 6]. Additionally we reported the observation of large photocurrents generated in the nanogaps[73, 6]. Quantitatively measuring these enhancements at the nanoscale has been very challenging. For gold electrodes separated by a sub-nanometer gap, we show unambiguously that nonlinear tunneling conduction leads to optical rectification, producing a DC photocurrent when the gap is illuminated. Comparing this photocurrent with low frequency conduction measurements, we determine the optical frequency voltage and the enhanced optical electric field across the tunneling region of the nanogap, and their dependence on gap size. Field enhancements exceed 1000, consistent with estimates from our surface-enhanced Raman measurements[5, 6, 73]. Our results push the limits of optical antenna performance and characterization. They also highlight the need for more realistic, quantum mechanical modeling of plasmonic optical properties at the nanometer scale, if such active plasmonic structures are to achieve their full potential.

Incident light interacts with the electrons in the metal, exciting plasmons, collective modes of the electron fluid. These plasmons have evanescent electromagnetic

fields that can be vastly larger than the incident radiation field. The largest field enhancements often occur in nanogaps between plasmonically active metal structures[74, 75]. However, it is extremely challenging to assess the enhanced field in such gaps directly. Precise theoretical calculations are also difficult, limited by the need to model electromagnetic response on scales ranging from the free space wavelength, λ, down to $\sim \lambda/1000$.

Electrons can tunnel across the smallest gaps, with a probability that decays exponentially with gap distance. Tunneling can act as an atomically precise probe of distance, as seen in scanning tunneling microscopy (STM). As explained below, nonlinearity in tunneling conduction can convert an optical frequency response of the metal into a DC current. This rectification process, originally proposed as a means of inferring the tunneling time[76], provides experimental access to precisely the quantity of interest: the optical frequency potential difference across the tunneling gap. Measurements of optical rectification in STM have been reported[77, 78], but thermal and surface photovoltage effects[79] complicate interpretation. A successful quantitative study of STM rectification at microwave frequencies was recently performed[79].

Here we demonstrate tunneling rectification at optical frequencies and use it to determine optical frequency voltage differences at the sub-nanometer scale, in gold nanogaps formed by electromigration. Combined with tunneling measurements of the nanogap distance, we then find the (enhanced) optical electric field at the tunneling region in these plasmonic structures. Electromigrated nanogaps have proven to be excellent substrates for surface-enhanced Raman scattering (SERS) [5], with strong evidence [6, 73] for single-molecule SERS sensitivity.

6.2 Theory

Suppose that the DC two-terminal current-voltage characteristics of some object are $I(V_{DC})$, and the conduction mechanism remains valid at some frequency scale 2ω. Then, in the presence of some small AC voltage bias, $V_{AC}\cos(\omega t)$, in addition to V_{DC}, one expects[79]

$$I \approx I(V_{DC}) + \frac{\partial I}{\partial V}|_{V_{DC}} V_{AC}\cos(\omega t) + \frac{1}{2}\frac{\partial^2 I}{\partial V^2}|_{V_{DC}} V_{AC}^2 \cos^2(\omega t) + ... \tag{6.1}$$

$$\approx \left[I(V_{DC}) + \frac{1}{4}\frac{\partial^2 I}{\partial V^2}|_{V_{DC}} V_{AC}^2 \right] + \frac{\partial I}{\partial V}|_{V_{DC}} V_{AC}\cos(\omega t) - \frac{1}{4}\frac{\partial^2 I}{\partial V^2}|_{V_{DC}} V_{AC}^2 \cos(2\omega t) + ...$$

There is a rectified DC current proportional to the nonlinearity of the conductance. As demonstrated[79] using STM and microwave irradiation, one may use a low frequency AC voltage and lock-in amplifier to measure $\partial^2 I/\partial V^2$ using the second harmonic of the AC voltage. Using lock-in techniques to measure the DC current due to microwave irradiation of a known microwave voltage, Tu *et al.*[79] find quantitative agreement between the rectified microwave current and the expectations of Eq. (6.1). *In the limit that this rectification picture is valid,* one may infer the local, radiation-induced V_{AC} by comparing radiation-induced current, I_{photo}, and detailed low frequency characterization of the conductance. In a tunnel junction, the differential conductance, $\partial I/\partial V$, at zero bias can be related to the interelectrode separation through the exponential decay of the conductance with increasing distance, $G \sim \exp(-\beta(d - d_0))$. Here d is the internuclear distance between closest atoms, d_0 is the size of the metal lattice constant, and β is the attenuation factor. The *average local electric field at the closest interelectrode separation*, $V_{AC}/(d - d_0)$, may then be inferred and compared with the incident field known from the incident optical intensity, giving a quantitative measure of the field enhancement due to the metal optical response. Since both V_{AC} and $d - d_0$ are found from tunneling, this is consistent.

It is important to recognize that the vast majority of the instantaneous potential drop between the two electrodes takes place across the vacuum between them; see Supplemental Information for a model calculation that demonstrates this.

A quantum treatment of radiation interacting with a nanoscale junction involves photon-assisted tunneling[80] and has been applied to atomic-scale metal contacts[81, 82]. When a junction is illuminated with radiation of energy $\hbar\omega$, the junction's plasmonic response results in an AC potential, V_{opt} at frequency ω across the junction. Following the Tien-Gordon approach[83], the quantum correction to the DC current induced by the radiation in the limit of small AC amplitudes ($eV_{\text{opt}} \ll \hbar\omega$) is given by

$$I(V_{\text{DC}}, V_{\text{opt}}, \omega) - I(V_{\text{DC}}) = \frac{1}{4}V_{\text{opt}}^2 \left[\frac{I(V_{\text{DC}} + \hbar\omega/e) - 2I(V_{\text{DC}}) + I(V_{\text{DC}} - \hbar\omega/e)}{(\hbar\omega/e)^2} \right]$$

$$(6.2)$$

If the tunneling nonlinearity is small on the voltage scale $\hbar\omega/e$, this expression reduces to Eq. (6.1) with V_{opt} playing the role of V_{AC}. This occurs when the transmittance of the junction $\tau(E)$ is smooth as a function of energy near the Fermi level of the leads, E_{F}, throughout $E_{\text{F}} \pm \hbar\omega$.

6.3 Sample Fabrication

Sample fabrication is described in Methods. Nanogaps are formed in the Au constrictions via electromigration[1]. The electromigration process is stopped once the zero bias DC conductance of the gaps is less than $2e^2/h \equiv G_0$. Typical conductances in this experiment are on the order of 0.6 G_0 to 0.016 G_0 indicating average gaps, $d - d_0$, ranging from 0.03 nm to 0.23 nm. Figure 6.1B shows a SEM image of a representative nanogap. Optical and electronic measurement details are also discussed in Methods. The illumination wavelength is 785 nm, with a peak intensity of 22.6 kW/cm^2, and
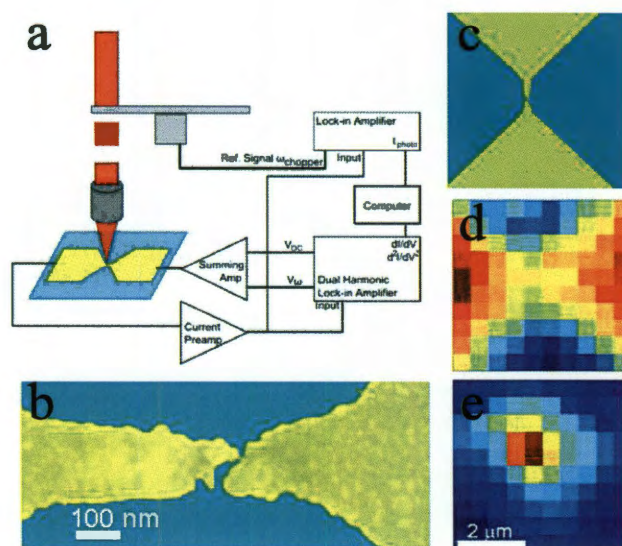
Figure 6.1 : Measurement approach and layout. A) Schematic of electrical charac-
terization measurement. B) Colorized SEM image of typical nanogap device. The
actual tunneling gap is not resolvable by SEM. C) Larger SEM view of electrodes and
nanogap. D) Spatial map of Si Raman line. Blue indicates lower Si peak intensities,
thus indicating the location of the Au electrodes. E) Spatial map of photocurrent for
the same device as in C, D. The color bar runs from red (20 nA) to blue (0 nA). The
photocurrent is clearly localized to the nanogap, to within optical resolution. Panels
C, D, and E are all on the same scale.

measurements are performed in vacuum at 80 K.

Samples are fabricated using standard electron-beam lithography techniques to define metal (1 nm Ti/15 nm Au) constrictions 100 nm in width and 600 nm in length between larger contact pads, on highly doped n-type Si substrates covered with 200 nm of thermally grown SiO_2. After cleaning in oxygen plasma, devices are wirebonded to a chip carrier, installed in a microscope cryostat, and cooled to 80 K.

6.4 Measurement Setup

After electromigration the sample is illuminated with a 785 nm laser focused to a gaussian spot with FWHM 1.9 μm and a peak intensity of 22.6 kW/cm^2. The laser is rastered over the sample surface and the Raman response of Si substrate is measured at 520 cm^{-1}. The Au electrodes attenuate the Si Raman emission, allowing precise mapping of the nanogap structure as shown in Fig. 1D. Once the nanogap is located via the Si Raman map, the laser is centered over the gap. The laser polarization is aligned along the original constriction.

The sample is electrically characterized via the apparatus presented in Fig 6.1A using two lock-in amplifiers and a current amplifier. The first lock-in amplifier applies an AC excitation ($V_{AC} \cos \omega_1 t$) to the sample at $\omega_1 = 2.0$ kHz and simultaneously measures the first ($\propto \partial I / \partial V$) and second harmonic response ($= \frac{1}{4} V_{AC}^2 \partial^2 I / \partial V^2$) of the nanogap to this excitation. There is no measurable change in either of these responses when the laser illumination is added or removed. The first harmonic response is essentially in phase with the ω_1 reference. The second harmonic response is phased relative to the $2\omega_1$ reference by 180 degrees as defined by the lock-in, such that the integrated $\partial^2 I / \partial V^2$ signal gives back the $\partial I / \partial V$ signal. The second lock-in amplifier is referenced to (and in phase with) an optical chopper at $\omega_{chopper} = 232$ Hz and

measures the current generated due to the radiation (I_{photo}). A summing amplifier is used to add a DC voltage V_{DC} to V_{AC}. With this arrangement, $I(V_{\text{DC}})$, $\partial I/\partial V$, $\partial^2 I/\partial V^2$, and I_{photo} as a function of V_{DC} can be measured simultaneously.

6.5   Optical Rectification Measurement

The DC $I - V$ characteristics of the samples after electromigration are weakly non-linear, with no sharp features, as expected for clean vacuum tunnel junctions. These junctions, ideally devoid of molecules, show *no* molecular surface-enhanced Raman scattering signal[5, 6], as expected. Figure 6.2 shows representative $\partial^2 I/\partial V^2$ vs. V_{DC} curves and simultaneously recorded I_{photo} vs. V_{DC} data for three different samples, acquired with the beam fixed over the nanogap. For each set of curves shown, the amplitude of V_{AC} has been set such that $\frac{1}{4}V_{\text{AC}}^2 \partial^2 I/\partial V^2$ and I_{photo} are the same amplitude. The fact that I_{photo} is directly proportional to $\partial^2 I/\partial V^2$ consistently over the whole DC bias range, including through the V_{DC} where both change sign, strongly implies that the photocurrent originates from the rectification mechanism. In this case, when $\frac{1}{4}V_{\text{AC}}^2 \partial^2 I/\partial V^2 = I_{\text{photo}}$, this implies $V_{\text{AC}} = V_{\text{opt}}$, where V_{opt} is the amplitude of the optically induced potential difference between the two electrodes that oscillates at $\omega/2\pi = 3.8 \times 10^{14}$ Hz. When the rectification mechanism is responsible for the photocurrent, comparison with low frequency electrical measurements gives a means of quantitatively assessing the plasmon-induced potential difference across the nanoscale interelectrode gap. As a consistency check, we have mapped the optically rectified current, I_{photo}, at fixed V_{DC} (while monitoring I, $\partial I/\partial V$, and $\partial^2 I/\partial V^2$, to ensure junction stability during the mapping procedure). As shown in Figure 6.1E, I_{photo} is only produced when the gap itself is illuminated.

Previous tunneling optical rectification experiments have been hampered by ther-
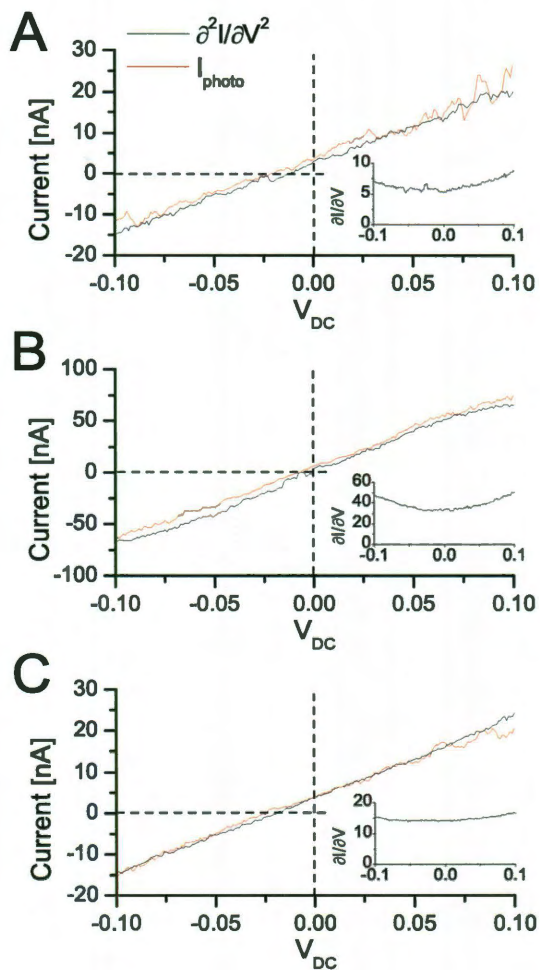
Figure 6.2 : Demonstration of optical rectification. A-C) Photocurrent (I_{photo}) and $\frac{1}{4}V_{AC}^2 \partial^2 I/\partial V^2$ as a function of V_{DC} for three different samples. Insets: Conductance in units of $\mu A/V$ for each device. Gap distances from tunneling measurements are 1.4 Å, 0.44 Å and 0.92 Å. Inferred V_{opt} values are 30 mV, 25 mV, and 33 mV, with uncertainties of 10%. Inferred electromagnetic fields are 2.1×10^8 V/m, 5.7×10^8 V/m and 3.6×10^8 V/m yield field enhancements of 718, 1940, and 1230, respectively.

mal voltages and thermal expansion. There is no reason to expect thermal voltages in our experiment since the device is a comparatively symmetric design, and with a centered laser spot there should be no temperature gradient between the electrodes. The macroscale unilluminated parts of the electrodes also act as thermal sinks. Differential thermal voltages caused by asymmetry of illumination would show up as systematic trends in I_{photo} as a function of laser position, and Figure 6.1E shows no such trends. Thermal expansion should be irrelevant, since the electrodes are intimately mechanically coupled to the substrate, with essentially no unsupported electrode material. To check for thermal effects, we looked for changes in $\partial I/\partial V$ at $\omega_{chopper}$, since any laser-induced expansion should modulate the interelectrode gap and thus the conductance. No measurable effect was found to better than the 10^{-4} level.

Optical rectification is further supported by measurements of I_{photo} vs. incident laser power. In Figure 6.3 we see the expected linear dependence. The best fit line has a slope of 0.37 nA/(kW/cm^2). Further, as expected, V_{DC} can be selected such that $\partial^2 I/\partial V^2$ is zero (not always at $V_{\text{DC}} = 0$), and at that bias I_{photo} measurements show no detectable current.

6.6 Transmission calculations

The validity of the rectification picture is not completely obvious for this system *a priori*. Detailed calculations of the transmission as a function of energy, as shown in Figure 6.4, demonstrate that for this particular material and illuminating wavelength, corrections to the classical rectification picture should be relatively small. At higher DC biases (> 100 mV, not shown), we do often observe deviations of the photocurrent from the measured $(1/4)V_{\text{AC}}^2\partial^2 I/\partial V^2$.
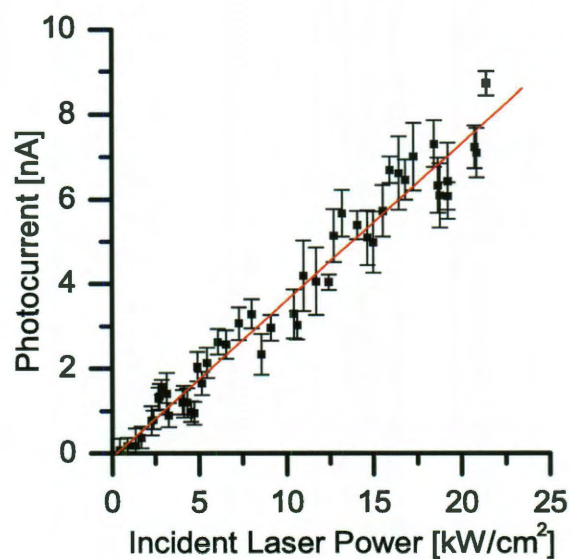
Figure 6.3 : Laser power dependence of optically rectified photocurrent, I_{photo}. The dependence is described by a linear power dependence with a slope of $0.37 \, \text{nA}/(\text{kW}/\text{cm}^2)$. Error bars indicate one standard deviation of the I_{photo} measurements at each laser power. The linear power dependence was found by a weighted least squares fit.
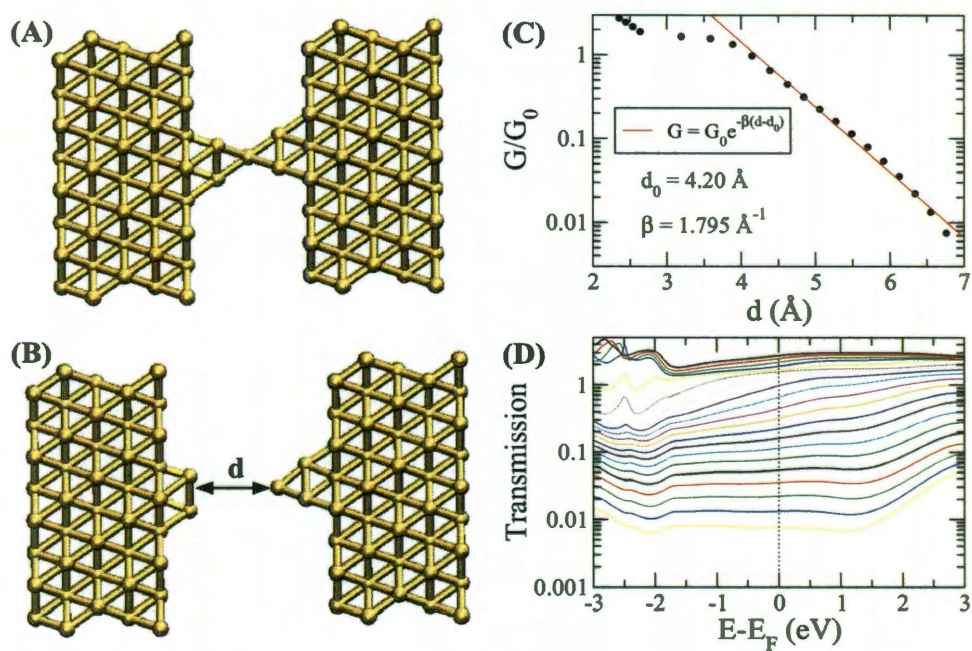
Figure 6.4 : Theoretical basis for validity of rectification. A) Geometry considered in the theoretical analysis of the distance dependence of the linear conductance. We start with a single-atom contact grown along the $\langle 111 \rangle$ direction. B) Stretched geometry with a distance d between the gold tips. C) Calculated linear conductance as a function of the interelectrode distance (full circles). The solid line shows the fit to the exponential function $G = G_0 \exp[-\beta(d - d_0)]$. The fit parameters are indicated in the graph. D) Zero-bias transmission as a function of the energy for the different geometries of panel (C).

To infer the nanogap size from the conductance measurements, we have performed theoretical simulations of the breaking process of gold atomic contacts. In these simulations, we have used density functional theory to determine the geometry of the junctions as well as to compute the transport properties within the Landauer approach, as detailed in Ref. [84]. In this approach the low-temperature linear conductance is given by $G = G_0\tau(E_F)$, where $\tau(E_F)$ is the transmission of the contact evaluated at the Fermi energy, E_F. To simulate the rupture of the gold nanowires, we start out with a single-atom contact (*e.g.*, Figure 6.4A). We separate the electrodes stepwise, re-optimize the geometry in every step, and compute the corresponding conductance. As in Figure 6.4C, in the relevant range, the linear conductance decays exponentially with an attenuation factor of $\beta \approx 1.8$ Å^{-1}. Extensive simulations (Supplementary Information) show that this exponent varies within 10% depending on the geometry of the contact.

Using $\beta = 1.85$ Å^{-1} (averaged over different junction structures), the interelectrode gap, $d - d_0$, can be found from the measured $\partial I/\partial V$. With this and the inferred V_{opt}, the enhanced electric field local to the tunneling gap may be determined. The experimental uncertainty in V_{opt} is approximately 5%, based on the comparisons shown in Figure 6.2. The experimental uncertainty in the tunneling conductance at zero bias is $\sim 1\%$. The dominant uncertainty in the inferred interelectrode separation is systematic, due to variation of β with morphology of the metal surfaces. Assuming that $d - d_0$ is the appropriate scale for computing the local electric field, for the samples in Figure 6.2, the optical electric fields (RMS) are 2.1×10^8 V/m, 5.7×10^8 V/m, and 3.6×10^8 V/m, respectively. Based on gaussian beam shape and incident power, the free-space incident RMS field is 2.9×10^5 V/m. Therefore we determine local enhancement factors of the electric field to be 718, 1940, and 1230. These

very large enhancements exceed expectations from idealized FDTD calculations[5] for wider gaps, and are consistent with observations of single-molecule Raman emission in such junctions [6, 73]. At sufficiently high electric field strengths the gap geometry can become unstable. We believe that this is the reason why $I - V$ curves of some devices exhibit instabilities. In the absence of the optical field or at considerably reduced incident laser fluences, the $I - V$ curves are very stable.

Our calculations clarify why the classical rectification formula works in our case. The transmission function (Figure 6.4D) of these gold contacts shows only a weak energy dependence around the Fermi energy in the interval $[E_F - \hbar\omega, E_F + \hbar\omega]$. This indicates that the quantum result of Eq. (6.2) reduces to the classical rectification formula of Eq. (6.1). This smoothness is because transport in gold contacts is dominated by the s atomic orbitals, with a relatively flat density of states. Similar physics should therefore be expected in other s-valent metals, such as Ag.

In several devices, conductance decreased over the course of hours of measurements, as the metal electrodes rearranged themselves, allowing us to track variations in V_{opt} (and inferred enhanced electric field) as a function of interelectrode separation (Figure 6.5). Despite device-to-device variability, the general trend shows increasing enhancement with decreasing $d - d_0$. This trend is slower than $1/(d - d_0)$ and weaker than classical expectations[85]. Such a comparatively weak increase in enhancement at low $d - d_0$ is qualitatively consistent with calculations that examine quantum tunneling corrections to plasmonic enhancements in nanoparticle dimers[85, 86]. However, those calculations predict an actual *decrease* in enhancement when $d - d_0$ is small enough that interelectrode conductance is strong enough to short out the nanogap plasmons. From our data and previous observations[6], this decrease in enhancement does not happen in gold nanojunctions until interelectrode conductance exceeds G_0.
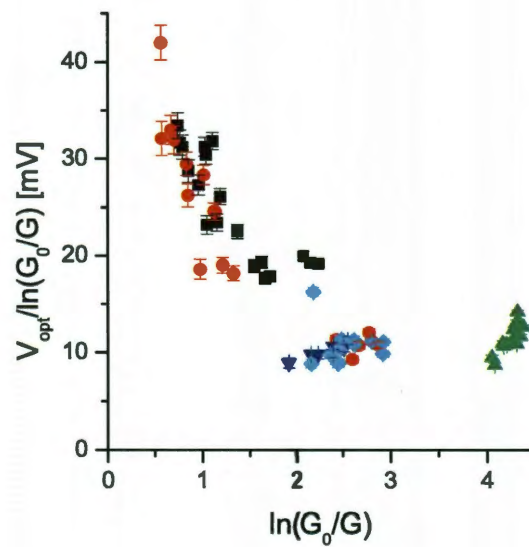
Figure 6.5 : Field enhancement at the tunneling region as a function of electrode separation. Data for five devices, obtained as the nanoscale gap geometries evolved over the course of many successive measurements at 80 K. The experimentally accessible parameters $(V_{opt}, \log G)$ are plotted; conversion into inferred electric field and interelectrode separation are based on $\beta = 1.85$ Å^{-1} and the assumption that $d - d_0$ is the relevant scale over which V_{opt} is dropped. Error bars indicate the statistical uncertainty in V_{opt} and $\log G$.

Our measurements highlight the need for detailed, realistic theoretical treatments of these nanostructures, incorporating optical interactions, quantum effects, and dynamical screening.

6.7 Conclusion

The ability to determine optically induced potentials and fields with quantitative accuracy has significant ramifications for the use of plasmonic nanostructures as optical antennas, substrates for surface enhanced spectroscopies for chemical and biological sensing, and platforms for photocatalysis. Extending these measurements into new materials, different wavelengths, and different incident polarizations will give insights into the coupling of external radiation, local plasmons, and motion of tunneling electrons.

Chapter 7

Vibrational and electronic heating in molecular nanojunctions

7.1 Introduction

In this final chapter we look into taking the measurement techniques of Chapter 3 and use them to investigate molcules in nanojunctions at steady-state when driven from equilibrium by incident light, or by the flow of an electronic current. When driven out of equilibrium the junction's vibrational and electronic degrees of freedom are, in general, no longer described by a single temperature[87, 88, 89, 90, 91, 92]. Obtaining information about the steady-state vibrational and electronic distributions in situ is extremely challenging. Here we use simultaneous measurements of surface-enhanced Raman emission and electronic conduction in single-molecue junctions[6] to determine effective vibrational and electronic temperatures as a function of junction bias voltage. AntiStokes/Stokes ratios for molecular Raman modes[93, 94] demonstrate vibrational pumping by both optical excitation and dc current, with effective temperatures exceeding several hundred Kelvin. AntiStokes continuum electronic Raman emission[34, 95] is analyzed using a simple model, and electronic effective temperatures are also found to increase by as much as a factor of three at bias voltages of a few hundred mV. While the precise effective temperatures inferred for the ions and the electrons are model-dependent, the trends of effective temperatures as a function of bias conditions are robust. These measurements provide previously inaccessible

information about heat generation and dissipation in molecular-scale junctions.

The question of dissipation and heating in nanoscale structures is of critical importance. When an electronic bias, V, is applied to a nanoscale junction, the electronic distribution is driven out of equilibrium, with "hot" electrons being injected from the source electrode into empty states eV above the Fermi level of the drain electrode. The electronic distribution rethermalizes on a distance scale set by the inelastic mean free path for electron-electron scattering. The much-utilized Landauer-Büttiker approach assumes that dissipative processes and heat generation are spatially removed from the junction region, so that the electronic distributions in the source and drain may be characterized by identical temperatures[96]. On longer time and distance scales, the electron system transfers energy to lattice vibrations via electron-phonon scattering. When a nanoscale junction contains one or more molecules, inelastic processes can also take place that transfer energy from the electrons to local molecular vibrational modes[97, 2]. In the presence of incident optical radiation, the situation is even more complicated[98] Direct absorption of light produces electron-hole excitations in the metal electrodes with energies as large as those of the incident photons, $\hbar\omega$. Likewise, the decay of plasmon excitations in the metal similarly produces hot electrons and holes. Raman scattering processes and hot electrons can excite local vibrational modes, even in the absence of any bias-driven processes[94].

Directly accessing the electronic and vibrational distributions in a nanoscale junction is extremely difficult. Like others before us,[89, 90, 91, 93] in this work we make the assumption that one may parametrize these (generally complicated) electronic and vibrational distributions by effective temperatures. Previous experiments have attempted to use the stability of mechanical break junctions as a proxy for an effective ionic (vibrational) temperature[99, 91, 100].

Raman spectroscopy, the inelastic scattering of light, can allow more direct access to energy distributions. The ratio, I_ν^{AS}/I_ν^{S}, of the intensities of antiStokes (I_ν^{AS}) and Stokes (I_ν^{S}) Raman responses for a particular vibrational mode (ν) yields information about the steady-state vibrational populations. Knowing that this ratio in equilibrium is set by a Boltzmann factor, we can define a mode's effective temperature via:[101, 93]

$$\frac{I_\nu^{AS}}{I_\nu^{S}} = A_\nu \frac{(\omega_L + \omega_\nu)^4}{(\omega_L - \omega_\nu)^4} \exp(-\hbar\omega_\nu/k_B T_\nu^{eff}). \qquad (7.1)$$

Here ω_L is the frequency of the incident laser and $\hbar\omega_\nu$ is the magnitude of the Raman shift. A_ν is a correction factor that accounts for the ratio of the antiStokes and Stokes cross-sections. Ordinary Raman spectroscopy has been employed to examine current-driven vibrational heating in nanotube[101] and graphene[102] devices.

In surface-enhanced Raman spectroscopy (SERS), local surface plasmons can enhance Raman response by many orders of magnitude, chiefly via optical antenna effects due to surface plasmons[34]. In this case, A_ν also accounts for differences in the Raman enhancement between the AS and S frequencies. Recently, surface-enhanced Raman spectroscopy (SERS) was employed to examine vibrational effective temperatures[93] in silver junctions containing many molecules, with some evidence of current-induced changes in vibrational temperatures. As in those experiments, we assume that A_ν does not vary significantly with bias conditions.

Even in the absence of bias-driven processes, T_ν^{eff} values greater than the ambient temperature, T, are possible due to optical pumping processes. If the Stokes process occurs faster than the molecule is able to relax vibrational energy to the bulk substrate, the excited vibrational population will exceed the equilibrium average. Moreover, sufficiently energetic electrons due to optical processes in the metal can couple to local molevular vibrational modes. In the absence of other processes, I_ν^{AS} is expected to scale quadratically with incident laser intensity, while I_ν^{S} scales linearly

as usual[94].

Nanojunction devices open the possibility of observing bias-driven vibrational pumping due to tunneling electrons via AS/S SERS measurements, as suggested theoretically[98] and experimentally[101, 93, 102]. Cross-sections for electron-vibrational pumping are expected to differ from mode to mode, as are the relaxation rates of those modes to the bulk substrate. In general, one must also be concerned about intra-molecular vibrational relaxation as well, which would tend to push all modes toward a single effective temperature.

Finally, in SERS systems with strong enhancements, a diffuse continuum of Raman scattered light is observed due to Raman scattering by the conduction electrons in the nanostructured metal[103, 74, 34, 95, 39]. Stokes scattering takes place through the creation of electron-hole excitations, while antiStokes scattering requires the presence ofexcited electrons above the Fermi level of the metal. Conservation of crystal momentum kinematically limits the accessible Raman shifts, with disorder and the surface playing a critical role[103, 95]. There is no complete theoretical treatment that is agreed to describe the full shape of the electronic continuum[39]. However, the AS Raman response at some shift ϵ is expected[95] to be proportional to the joint density of states (JDOS) for electrons at energy $\epsilon + E_{\mathrm{F}}$ and holes at energy E_{F}. Taking the kinematic restriction and the band densities of states to be slowly varying over the AS shift range of interest, and neglecting any resonance effects, we expect

$$I_e^{\mathrm{AS}}(\epsilon) \propto \int f(E + \epsilon, T_e^{\mathrm{eff}})(1 - f(E, T_e^{\mathrm{eff}}))dE = \frac{\epsilon}{e^{\epsilon/k_{\mathrm{B}}T_e^{\mathrm{eff}}} - 1}, \qquad (7.2)$$

where the integral is over the conduction band, $f(E, T)$ is the Fermi-Dirac function, and T_e^{eff} is an effective temperature for the conduction electrons. Only Raman emission from the electrons that are proximate to the SERS "hotspot" is readily detected, since that emission is appropriately enhanced.

7.2 Sample Fabrication

Samples were fabricated as per Section 1.7. The nanowires defined by e-beam lithography were approximately 120 nm wide and consisted of a 0.5 nm Ti adhesion layer and 15 nm of Au. The nanowires are approximately 600 nm long and connected to larger electrical leads and contact pads. After cleaning samples were soaked in the molecules of interest either a three-ring oligophenylene vinylene terminated in amine functional groups (OPV3) or 1-dodecanethiol. Soaking was performed in either 0.1 mg/mL OPV3/THF or 10 mM 1-dodecanethiol in ethanol for 24 hours to form a self-assembled monolayer on the Au surface. After assembly samples were wire bonded to a ceramic chip carrier and placed in an optical cryostat. Samples were then cooled to 80 K in vacuum.

Nanogaps were formed in the nanowires via the electromigration(Section 1.6. Gap formation was performed with an automated computer program which stopped the electromigration process once the electrical conduction dropped below $2e^2/h$. The final nanogap conductances in this experiment range from 0.5 G_0 to 0.01 G_0, where $G_0 \equiv 2e^2/h$ is the quantum of conductance. This conductance is higher than that expected for an idealized gap bridged by such a molecule attached to both electrodes[10]. It is much more likely that direct metal-metal tunneling contributes significantly to the total conductance, and that the molecule is not neatly bridging the gap[104]. An image of a typical nanogap is shown in Figure 7.1A.

7.3 Measurement Setup

After electromigration optical measurements are performed by illuminating the sample surface at 785 nm with a Gaussian laser beam with a spot size of 1.9 μm, incident
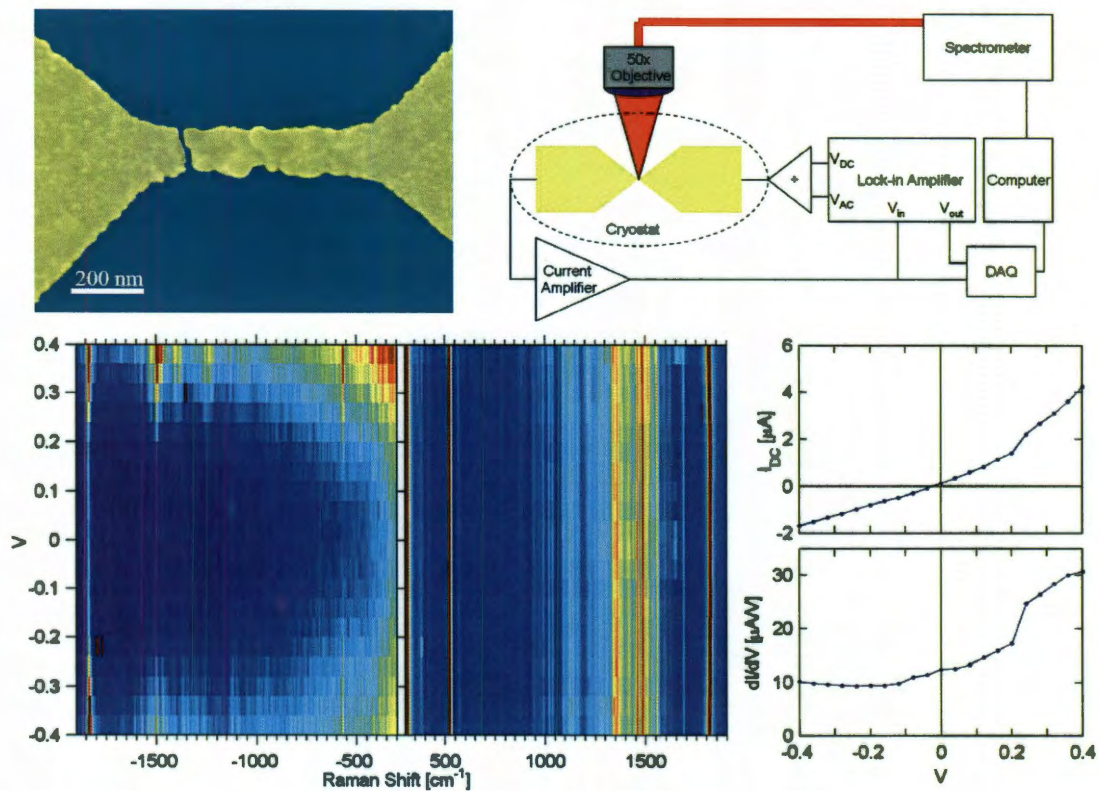
Figure 7.1 : A) SEM false color image of a typical nanogap. B) Schematic of electrical and optical measurement. C) Waterfall plot of Raman response of an OPV3 junction as a function of DC bias, V. Color scale ranges from blue (0 counts) to red (200 counts for antiStokes, 5000 counts for Stokes). The antiStokes spectrum shows strong dependence on V while the Stokes side is relatively constant as a function of bias. The strong Stokes peak at 520 cm^{-1} is from the silicon substrate. D) Simultaneously measured current and differential conductance as a function of V.

intensity of 23 kW/cm^2, and polarization aligned along the nanowire. The laser beam was rastered over the sample and a spatial map of the Raman response of the Si substrate was measured at 520 cm^{-1} as described in reference [6]. The Au electrodes of the nanogap attenuate the silicon signal allowing precise positioning of the laser over the nanogap. The SERS signal of the nanogap is then measured. The SERS signal can also be spatial mapped to confirm that it originates from the nanogap. The spectra are all corrected to adjust for the spectral sensitivity of the system over the measured wavelength range by calibrating to a known blackbody source (T=2960 K). Integration times for SERS spectra range from 5 s to 10 s depending on signal strength.

Electrical measurements of the nanogap are performed using a current amplifier and lock-in amplifier as illustrated in Figure 7.1B. The lock-in amplifier applies a 10 mV AC signal to the sample and measures the first harmonic response (dI/dV). A summing amplifier is used to add a DC signal (V) to the lock-in signal allowing the current amplifier to measure I$_{DC}$. In this configuration both I and dI/dV can be measured simultaneously as functions of V.

Simultaneous optical and electrical measurements provide a wealth of information, as seen in Figure 7.1C, D, E. For this sample we can observe optical and electrical pumping of individual vibrations of OPV3. We can also observe apparent heating of the electrons as evidenced by the rise in low wavenumber antiStokes continuum with increasing magnitude of bias voltage. For simplicity in presentation, we will discuss the effective temperature analysis in terms of optical vibrational pumping, electrical vibrational pumping, and electron heating seperately from one another.
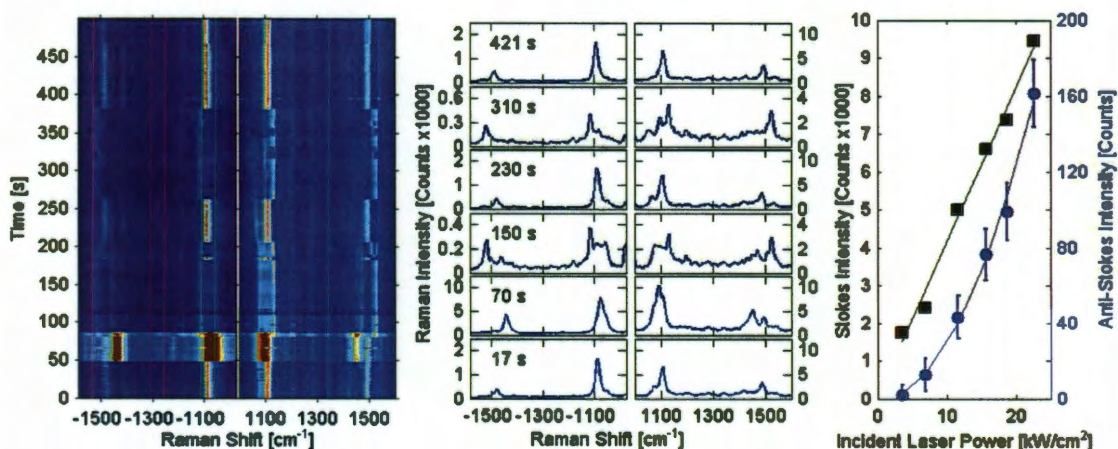
Figure 7.2 : A) Raman response of a dodecanethiol junction as a function of time under zero bias. Blue indicates 10 (100) counts and red indicates 2000 (8000) counts for antiStokes (Stokes) sides. The junction switches stochastically between several stable configurations, each with characteristic spectra that exhibit strong optical pumping of vibrational modes at 1099 cm^{-1} (C-C stretch) and 1475 cm^{-1} (CH_2 or CH_3 deform). B) Spectra from given time slices in A. We note that the higher energy peak spectrally diffuses between 1475 cm^{-1} and 1525 cm^{-1} and the lower energy peak between 1099 cm^{-1} and 1110 cm^{-1}. The temperature of the 1099 cm^{-1} mode in Kelvin is 769, 1722, 532, 754, 512, 775 with increasing time. The temperature of the 1475 cm^{-1} mode in is 701, 815, 658, 729, 648, 746. We note that at 70 s a vibration at 1450 cm^{-1} is observed at 2161 K. All temperatures have an uncertainty of $\pm$ 10 K. C) Power dependence of Stokes (black) and antiStokes (blue) signal taken from a different device also showing optical pumping. As expected, in the optical pumping regime the Stokes signal is linear (solid line) in laser power while the antiStokes signal increases quadratically (solid line) in laser power. Error bars indicate uncertainty in signal due to read and shot noise in CCD.

7.4 Optical pumping of vibrations

Optical pumping of vibrations ($T_\nu^{\text{eff}} \neq T$ at $V_{DC} = 0$) was observed in nanogaps for both test molecules. Figure 7.2A shows the evolution of the Raman response of a dodecanethiol junction as a function of time. Several different discrete spectral configurations are observed, as seen on the Stokes side of the spectrum. For each of these configurations, we observe the same two modes (1100 cm^{-1} and 1490 cm^{-1}) in the antiStokes spectrum, but with varying intensities. Effective temperatures are inferred using Equation 7.1, assuming the Raman enhancement is frequency independent and the cross-sections for Stokes and anti-Stokes scattering are equal ($A_\nu = 1$). Effective temperatures range from 300 K to greater than 2000 K, demonstrating that vibrational populations may be driven far from equilibrium via optical excitation alone. The simplest explanation for the observed simultaneous changes in spectrum and effective temperatures is that the molecule(s) in question undergo conformational changes relative to the Au electrodes. Such changes in conformation can affect SERS enhancement, vibrational relaxation times, and electronic coupling between the molecule and electrodes. Any of these changes could result in different pumping rates. Note that the two modes presented here are not in equilibrium with one another, with an effective temperature difference of more than 300 K between them. As shown in Figure 7.2C, we observe a quadratic dependence of the antiStokes signal on incident power, as expected in the optical pumping regime.

An example of optical vibrational pumping in OPV3 is shown in Figure7.3. We observe several discrete spectral configurations. Each configuration has varying levels of optical pumping, with the most noticable change occuring at 150 s, when several lower energy vibrations appear in the antiStokes signal.
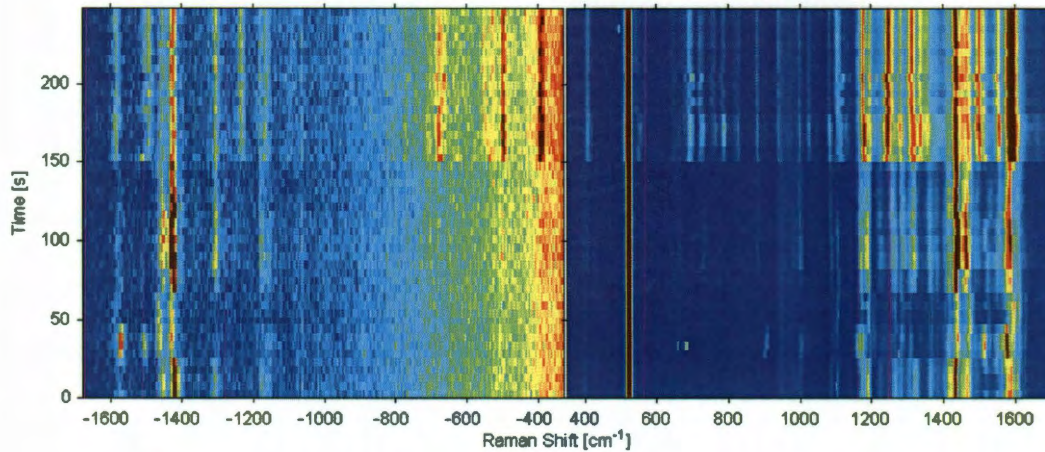
Figure 7.3 : Raman response of an OPV3 junction as a function of time under zero bias. Blue indicates 0 counts and red indicates 100 (8000) counts for antiStokes (Stokes) sides. Integration time is 1 s. The junction switches stochastically between several stable configurations, each with characteristic spectra that exhibit strong optical pumping of different vibrational modes.

7.5 Electrical pumping of vibrations

Under DC bias we observe strong electrical pumping of specific vibrational modes in both OPV3 and dodecanethiol. We present data sets that show certain characteristic behaviors; additional examples are given in Supplemental Information. Figures 7.4A and D show the bias dependence of T_ν^{eff} for different modes for two different devices with OPV3 assembled on them. In both cases we observe an approximately linear increase in T_ν^{eff} with increasing $|V|$. For the sample in Figure 7.4A-C we are signal limited below $V = 0.2$ V and observe no measureable antiStokes signal above our detector noise floor. There is a voltage asymmetry in conductance and T_ν^{eff} between the positive and negative sweeps. On the positive V side, the 1625 cm^{-1} mode is only slightly lower in effective temperature than the 1317 cm^{-1} mode, while on the negative V side, the effective temperature difference is considerably larger. This dichotomy is

Figure 7.4 : A) Effective vibrational temperature as a function of V for two OPV3 modes: 1317 cm^{-1}(red) and 1625 cm^{-1}(blue). Error bars indicate uncertainty in temperature due to anti-Stokes amplitude measurements. Inset) IV curve for this device. B) Raman response of this device as a function of V. Blue indicates 10 (2500) counts and red indicates 250 (10,000) counts for anti-Stokes (Stokes). C) Sample spectra for given voltage. All Stokes and anti-Stokes are plotted on the same scale. Full amplitude corresponds to 235 (10,000) counts for anti-Stokes (Stokes). D) Effective vibrational temperature as a function of V for three OPV3 modes: 1815 cm^{-1}(black), 1480 cm^{-1}(red) and 562 cm^{-1}(blue). Error bars indicate uncertainty in temperature due to anti-Stokes amplitude measurements. Simultaneous optical and electrical vibrational pumping are observed for the 1810 cm^{-1} mode as T_{eff} is much greater than 80 K at $V = 0$. E) Raman response of this devices as a function of V. Blue indicates 0 counts and red indicates 200 (5000) counts for anti-Stokes (Stokes). F) Sample spectra for given voltage. All Stokes and anti-Stokes are plotted on the same scale. Full amplitude corresponds to 350 (10,000) counts for anti-Stokes (Stokes).

reproduced on multiple voltage sweeps on this device. One reasonable explanation for this sort of mode-to-mode variation and voltage asymmetry is that the molecule's electronic coupling is different for the two electrodes, so the effective cross-sections for electron-vibrational pumping depend on the direction of current flow. Such an explanation has been suggested for asymmetries observed in vibration-mediated inelastic electron tunneling spectroscopy[105]. Figure 7.4B also shows another feature that we observe with some regularity in such junctions: a systematic shift in energy of about 15 cm^{-1} is observed for most (Stokes) vibrational modes as a function of V. This is an example of a Raman Stark shift[48]. Finally, a decrease in overall Raman intensity is observed on the positive bias sweep. We attribute this to slow drift of the laser spot over the sample this should not affect the phonon temperature since we are not in a detectable optical pumping regime.

For the device shown in Figure 7.4D-F, both electrical and optical vibrational pumping are observed. The clear 1815 cm^{-1} AS mode has measurable AS signal at zero bias, with a temperature more than 300 K above the substrate temperature. Until V exceeds $\hbar\omega_\nu$, no increase in T_ν^{eff} is observed, as expected. Once V exceeds this threshold, once again an approximately linear increase in T_ν^{eff} is observed with increasing V. These observations are consistent with theoretical treatments of electron-vibrational scattering during off-resonant conduction[90, 106]. We do not observe any signs of vibrational cooling at high biases[89, 93]; nor do we see $T_\nu^{\text{eff}} \sim \sqrt{V}$ at lower biases, as would be expected for cooling of the local modes via relaxation to bulk 3d phonons[89]. This suggests that local vibrational relaxation to the substrate takes place via other means, such as coupling to phonons of reduced dimensionality.

Again we observe an asymmetry in conductance (Figure 7.1E) and T_ν^{eff} between the positive and negative sweeps. The vibrations at 1480 cm^{-1} and 562 cm^{-1} show
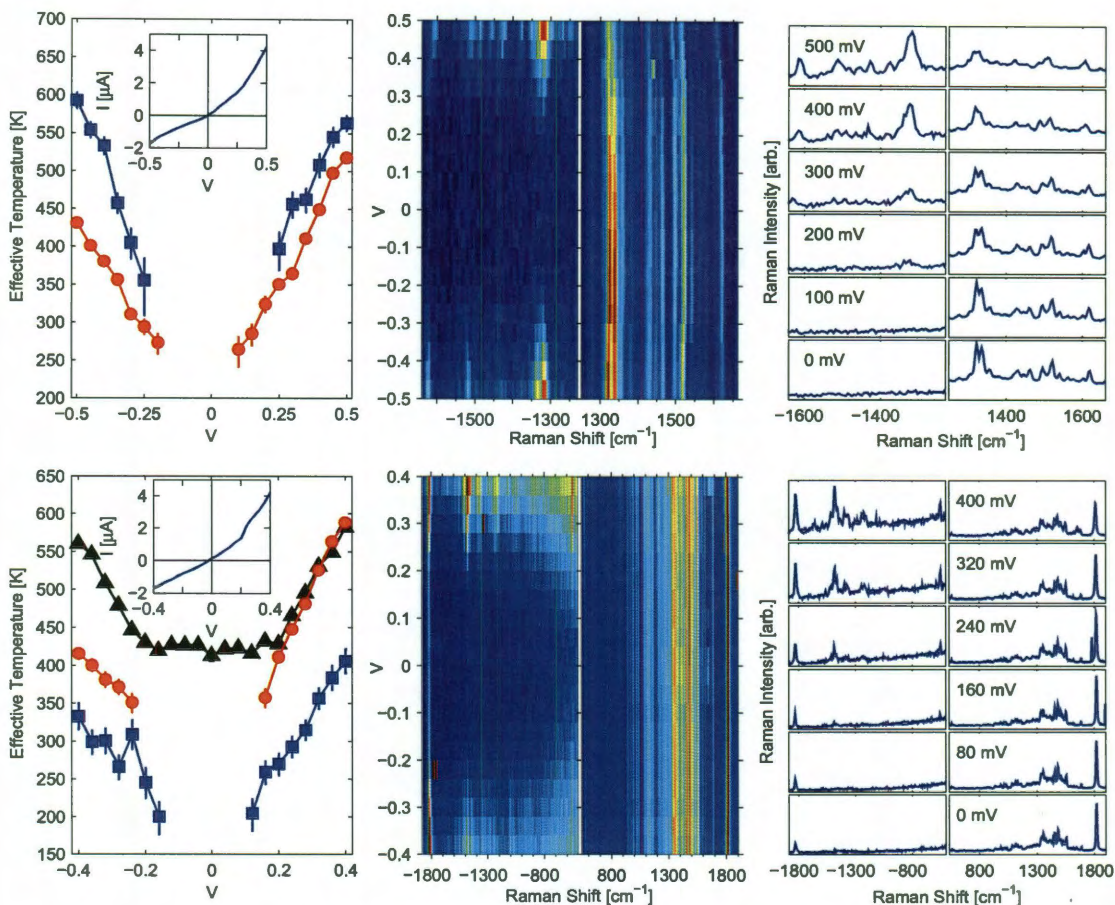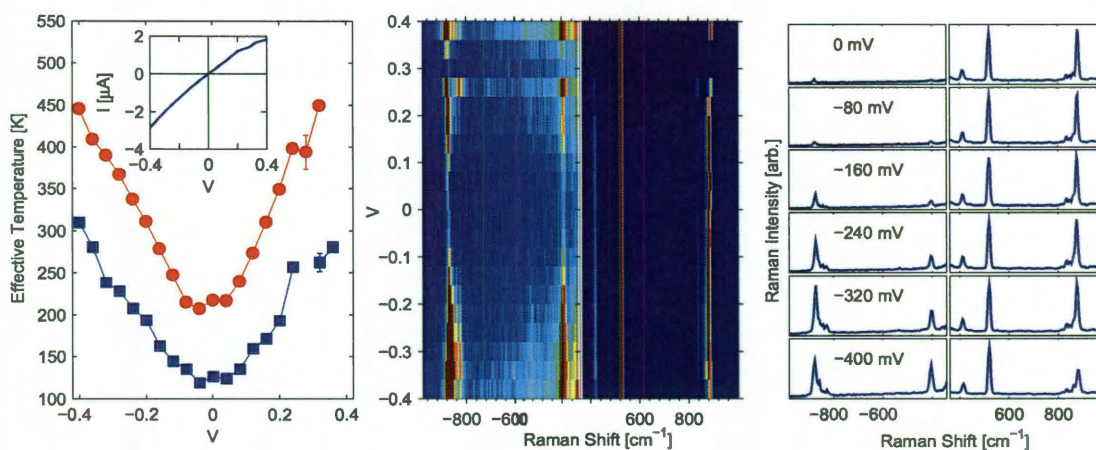
Figure 7.5 : A) Effective vibrational temperature as a function of V for two OPV3 modes: 880 cm^{-1}(red) and 410 cm^{-1}(blue). Error bars indicate the uncertainty in inferred effective temperature due to the statistical limitations of the antiStokes amplitude measurements. Inset) IV curve for this device. B) Raman response of this device as a function of V. Blue indicates 10 (2500) counts and red indicates 250 (10,000) counts for antiStokes (Stokes). The strong Stokes peak at 520 cm^{-1} is from the Si substrate. C) Sample spectra for given voltage. All antiStokes (Stokes) spectra are plotted on the same scale. Full amplitude corresponds to 1200 (18,000) counts for antiStokes (Stokes).

a strong asymmetry similar to the conductance but the 1815 cm^{-1} mode shows very little asymmetry. Again this suggests that effective-cross sections for electron-vibrational pumping are different on a per vibration basis.

An additional example of electrical vibration pumping in OPV3 is shown in Figure 7.5. The two modes observed 880 cm^{-1} and 410 cm^{-1} have temperature differences of almost 150 K at $V = 0.4$ V. This device also exhibited optical pumping of both modes resulting in zero bias temperatures of 220 K and 120 K respectively. As expected both modes to not show any electrical pumping until V exceeds the vibrational energy. At 280 mV a sharp change in conductance is observed and no pumping is observed. The conductance changes again at 320 mV and pumping is observed but with less

AS intensity than previously. This is strong evidence the importance of the local environment to pumping cross-sections.

7.6   Heating of conduction electrons

In Figure 7.6 we examine heating of the electrons as a function of V. Effective temperatures are found by fitting the AS continuum spectra to Equation 7.2. An overall amplitude is fit at $V = V_{\mathrm{max}}$ and held fixed for other bias voltages, leaving only one free parameter, T_e^{eff} to fit as a function of V. Representative spectra and fits are shown in Figures 7.6C, F. Error estimates for T_e^{eff} correspond to a doubling of χ^2 from the best fit. In Figure 7.6A we see a roughly 150 K change in temperature over a 400 mV change in bias. There is a significant asymmetry in both the temperature and current as a function of V. One possible explanation for the asymmetry in temperature is that only one electrode gets hot at a time depending on the direction of current flow and the thermal coupling to the bulk electrode is different for each side of the nanogap. An increase of T_e^{eff} roughly linear in V is consistent with a general argument based on steady state heat flow in the electron system[89].

An additional example of electrical heating is shown in Figure 7.7. This sample had more symmetric $I-V$ curves and power dissipation than other samples presented. The effective temperature is observed to be more symmetric as well when considering the size of the error bars.

The observation of effective electronic heating with bias in molecular-scale tunnel junctions is important. While it is expected on general grounds[89], the Landauer-Büttiker approach to conduction, commonly used to model such junctions, does not account for such an effect. Additional experimental consequences would be expected, including broadening of inelastic electron tunneling spectra at high biases under sim-
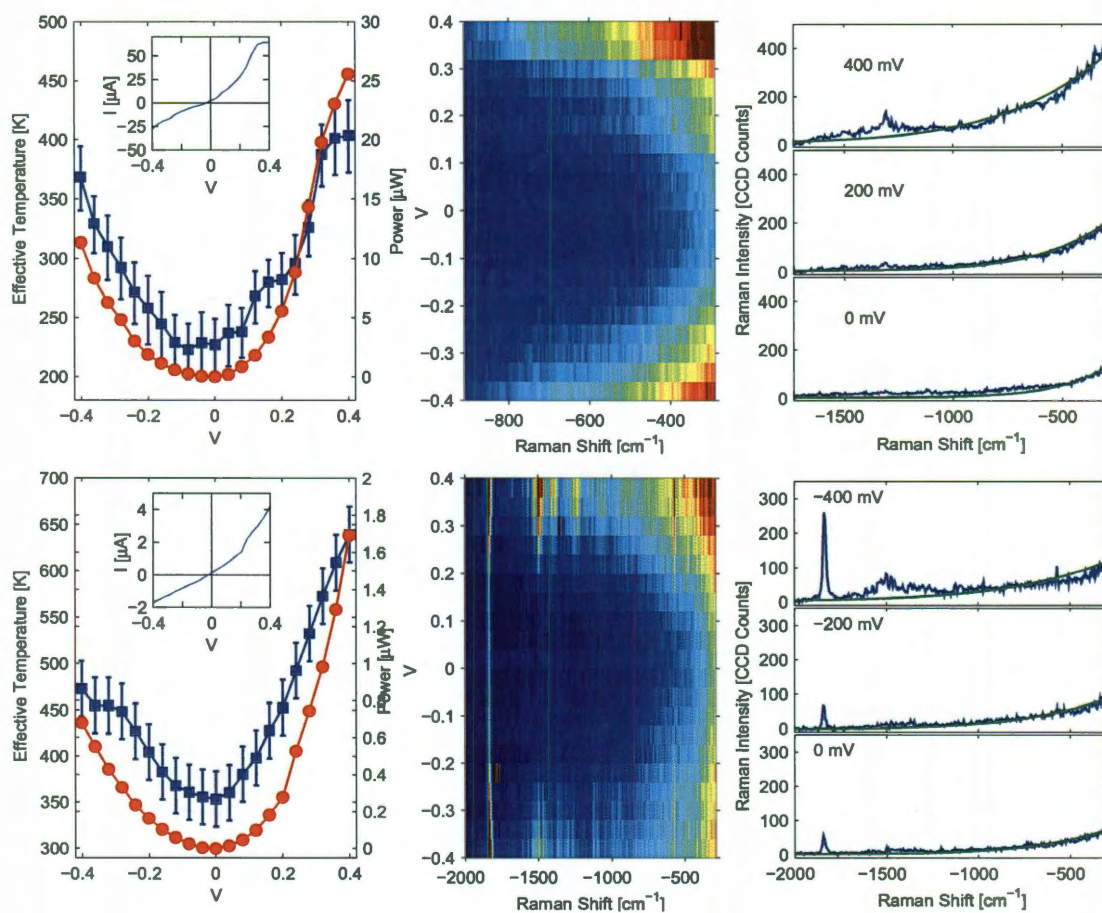
Figure 7.6 : A&D)Effective temperature(blue) and dissipated electrical power (red) for two different devices. The device in (D, E, F) is the same device that was analyzed in Figs. 1 and 3. Insets: $I - V$ curves for these devices. Error bars are described in text. B&E) Raman response for these devices. Blue indicates 0 counts and red indicates 350 (A) or 150 (D) counts. C&F) Sample spectra (blue) and best fit given by Equation 2 (green) for a given voltage.
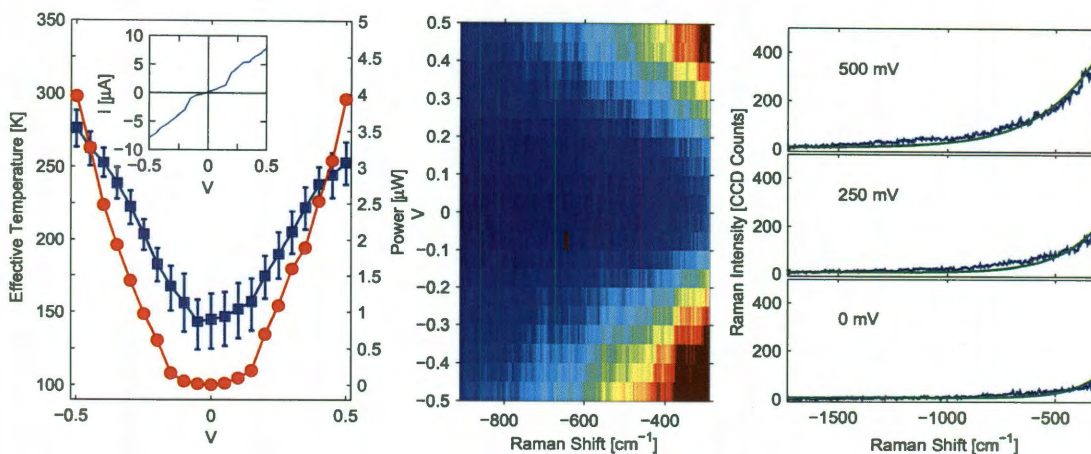
Figure 7.7 : A) Effective electronic temperature(blue) and dissipated electrical power (red) for a device with very little vibrational Raman activity. Error bars are described in text. Inset) $I - V$ curves for these devices. B) Raman response for these devices. Blue indicates 0 counts and red indicates 350 counts. C) Sample spectra (blue) and best fit given by Equation 7.2 in main text (green) for a given voltage.

ilar current densities, and signatures of heating in the junction current noise. Investigations in these directions are ongoing.

7.7   Raman Stark Shift

Figure 7.8 provides a closer look at the Raman Stark effect seen in Figure 7.4B A clear shift of 13 cm^{-1} can be observed between zero bias and 0.5 V. All vibrational modes present experience similar shifts. These shifts are reproducible on subsequent voltage sweeps of this junction. An additional example is shown in Fig. 7.9 where again distinct shifts as a function of bias are visible. In this case changes in Raman intensity are also observed as a function of bias possibly indicating that in the presence of a strong electric field the time variation in polariability of the vibration is reduced to zero.
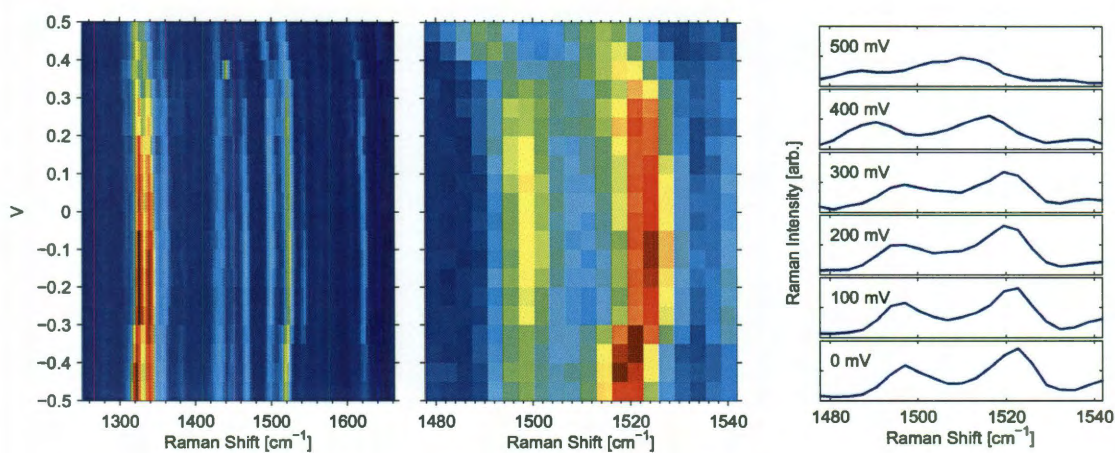
Figure 7.8 : A) Raman response of the same device shown in Figure 7.4A. A shift of about 15 cm^{-1} is present for many spectral lines. Blue indicates 2500 counts and red indicates 10000 counts. B) Zoom in of Raman response for the mode centered at 1523 cm^{-1}.Blue indicates 2500 counts and red indicates 7000 counts. C) Sample spectra for given voltage. All spectra are plotted on the same scale with a base line of 3000 counts substracted. Full amplitude corresponds to 4000 counts. The peak at 1523 cm^{-1} can clearly be seen systematically shifting to lower energy at higher voltages reaching 1510 cm^{-1} at 500 mV.
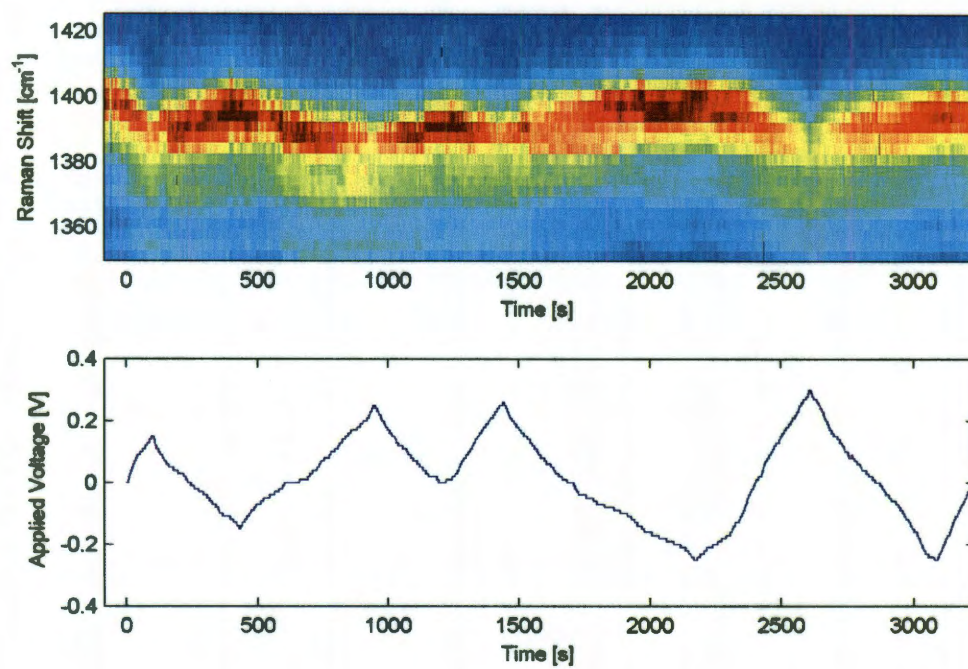
Figure 7.9 : Raman response of an FOPE device over time as the bias is changed. The nominally 1400 cm^{-1} mode is observed to shift in position and intensity with changing bias.

7.8 Conclusion

There are *systematic* uncertainties in the effective vibrational and electronic temperatures (due to the unknown values of A_ν and the lack of a detailed theory of the electronic Raman continuum). However, the *trends* captured in the data (the dependence of the effective temperatures on the bias conditions, for example) are robust. These experiments demonstrate that it is possible to extract highly local information about the effective ionic (vibrational) and electronic temperatures within molecular-scale junctions under electrical bias. The resulting data are among the first direct measurements that will allow specific tests of theoretical treatments[87, 89, 90, 92] of dissipation at the nanoscale. Even in these proof-of-principle measurements, the data contain a wealth of information. It is clear that there can be tremendous mesoscopic variation in electron-vibrational couplings and vibration-bulk relaxation rates. These experiments may open the door to deliberate control and engineering of such effects.

Appendix A

Documentation for Raman Software

A.1 Introduction

This appendix will act as a manual for the operation of the software I developed for our custom built Raman microscope. Additionally there will be a brief discussion of the code in case modifications are required in the future. The software called RamanMicroscope (RM) was developed in C# using Microscope Visual C# 2008 Express Edition and is based upon the .NET 2.0 framework. Although the software is called RamanMicroscope it is important to note that the actual executable program is called "LabVIEW.exe", which allows the RM software to interface with the Jobin Yvon software drivers without purchasing the software development kit (SDK).

A.2 Prerequisites

In order to run correctly RM requires certain hardware to be installed and turned on before running. First the Jobin Yvon iHR320 spectrograph and Synapse CCD must be on and the Jobin Yvon software and drivers already installed. Second the CCD camera must be plugged in and the IC Capture 2.0 and IC Imaging Control 3.0 software installed. Third the PI Nano - Piezo Stage Controller must be on and the required software/drivers installed. Finally it is necessary to have the .NET 2.0 framework installed which is automatically installed with Visual C# 2008 Express Edition.

A second program similar to RM is also provided called RamanProject (RP) that does not require any hardware to run. However, it can not acquire data, only open and display existing data. All RP needs to run is the .NET 2.0 framework, which is already installed on many computers.

A.3 Projects

RM uses the concept of projects to organize and store data. A project organizes spectra into types of spectra (single, time, image, triggered). Each spectrum is given a name although the names do not have to be unique. Unique names are recommended and necessary if using the text file export options. Typically the names are a few characters to describe the spectrum type (i.e. TS for time spectrum) followed by a number indicating the order in which the spectra were taken. The contents of the current project are shown in the Project Viewer which will be discussed later. Projects may also contain text notes which can be helpful for documenting what each spectrum is. Projects are saved in a single XML file. These files are very large and complicated to load into programs like MATLAB, so an option to export spectra in easy-to-parse text files is also provided.

A.4 Spectrum Types

RM can acquire several different types of spectra: single, time, image and triggered spectra. Single spectra consist of a single spectrum acquired at the current laser position. Time spectra consist of a series of spectra acquired with constant time spacing. A time stamp is recorded for each spectrum, allowing the spectra to be synchronized with external measurements. Image spectra consist of a series of spectra acquired at different laser positions on the sample surface. These spectra can be

processed to generate images of particular spectroscopic features as a function of position. Triggered spectra consist of a fixed number of spectra taken every time a TTL pulse is send to the Synapse CCD. Triggered spectra are particularly useful for synchronizing with external measurements.

A.5   Laser Rastering

The RM software can use the piezoelectric stage to raster the laser across a sample. The stage coordinates range from 0 to 200 μm in both the X and Y axes. The beam is centered when set to 100,100. The current stage position is reported in the lower left hand corner of the main window. It is important to note that the stage coordinates do not reflect the actual distance travelled by the beam. The beam shift experienced by the laser is the distance moved by the stage divided by the effective magnification, which at the time of this writing is 12.5×, indicating the largest scan possible is 16 × 16 μm. The laser rastering design is based on reference [107].

A.6   Initialization

Upon starting the RM program the hardware is initialized. First the CCD and Spectrograph are initialized then the piezo stage and finally the CCD camera. The user is required to select the correct stage during the initialization process. After initializing the hardware the main program window is opened which contains several additional windows. These windows include the project viewer, spectrum acquisition settings, CCD camera display, hardware spectrum viewer and spectrometer settings. At this point the CCD camera will display a live image and the spectrometer settings will reflect the current status of the spectrometer. Additionally the piezo stage will be centered at 100,100.

A.7 Main Window

The main window contains all the other windows and is shown in Fig. A.1. The main window provides a menu to access several important features of RM. The `File` menu has options to create new projects, load existing projects (which discards the current project contents), and to save the existing project (Fig. A.2). Saving and loading projects can be a lengthy process so a progress bar will be shown to indicate when saving or loading is occurring and will vanish when the process is complete. The `File` menu as has options to export single, time, image and triggered spectra in an easy to read text format. When exporting the user selects a destination folder to export to and all spectra of the desired type are saved in that folder with the name of the spectra as the filename. The files are saved as `.txt` files. If the same name is used twice the first spectrum will be overwritten.

The `Add` menu allows the user to add a text note to the project (Fig. A.3). The `View` menu is used to reopen the project viewer, CCD camera display, spectrum acquisition settings, or spectrometer settings in the even they are closed. The `Window` menu has an option to close all open spectra windows.

A.8 Project Viewer

The project viewer shows the contents of the current project (Fig. A.4). This includes single, time, image, and triggered spectra as well as any text notes. Spectra can be opened in a spectrum viewer window by double clicking their name. Spectra may be deleted by right clicking their name and selecting `Delete`. Right clicking time and triggered spectra (Fig. A.5) provides and option to make a waterfall plot of the spectrum which is opened in the waterfall plot viewer (Section A.13). Right clicking
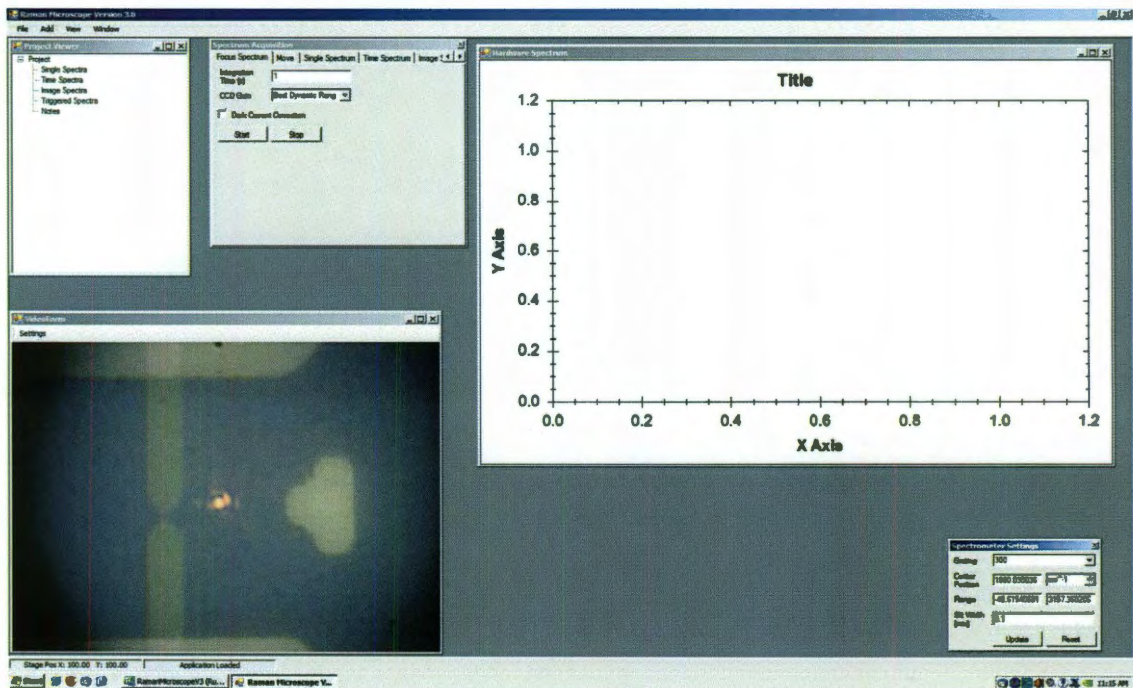
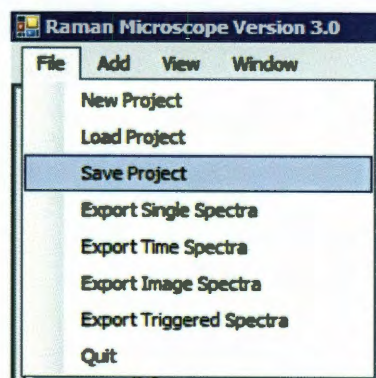Figure A.1 : RM main window after intialization.

Figure A.2 : RM File menu.
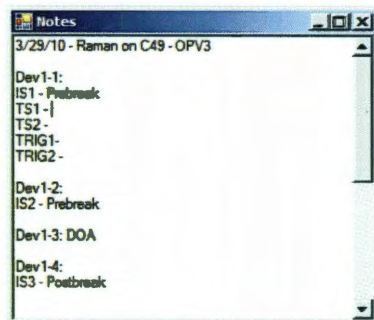
Figure A.3 : Notes are text that can be saved in a project. They are useful for documenting the specifics of each spectrum.

image spectra provides the option of making intensity maps (Fig. A.6) which will be discussed in Section A.14.

A.9 CCD Camera Viewer

A live image from the CCD camera is shown in a window called `VideoForm` (Fig. A.7). If the window is resized the image is not scaled so you will not be able to see the entire image. The `Settings` button does nothing.

A.10 Spectrometer Settings

The spectrometer settings window shows the current spectrometer settings including the `Grating` in use (specified in grooves/mm), `Center Position` of the grating in the current units, current detectable wavelength `Range` and the `Slit Width` of the entrance slit to the spectrometer (Fig. A.8). The units for the center position can be changed between nm, cm^{-1}, and eV. Spectra will be recorded in the units of the spectrometer at the time of acquisition. The center position of the grating (the wavelength that hits the center of the CCD) can be changed by typing in a new value

Figure A.4 : RM Project Viewer. This project has time, image, and triggered spectra. It also has one set of notes.
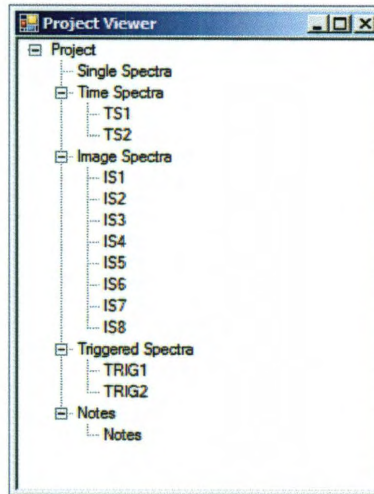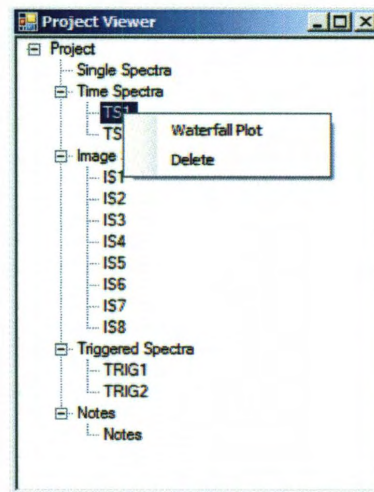

Figure A.5 : Time spectrum menu in the project viewer.
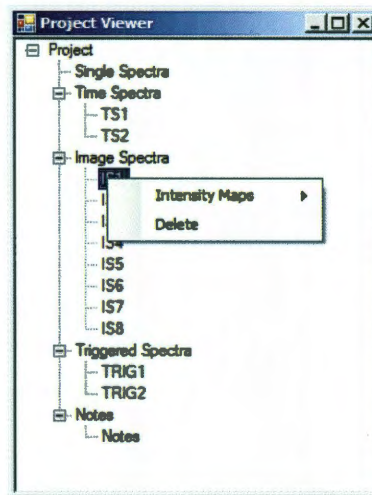
Figure A.6 : Image spectrum menu in the project viewer.

Figure A.7 : CCD camera viewer.
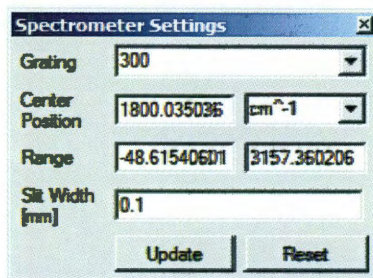
Figure A.8 : Spectrometer settings window.

and clicking the `Update` button. When updating the `Update` button will gray out until the spectrometer has reached the correct position. The range will automatically update to indicate the new detectable wavelength range. The slit width may also be changed in this fashion. If you change the value of center position or slit width but do not want to make the change the `Reset` button will return the displayed values to the hardware's current value.

A.11   Spectrum Acquisition

The spectrum acquisition window has different tabs that allow you to take `Focus Spectrum` (these are like single spectra but not saved), `Move` the stage, and take `Single Spectrum`, `Time Spectrum`, `Image Spectrum`, and `Triggered Spectrum` (Fig. A.9). Stage movements should be in the range of 0 to 200. The `Goto Center` button returns the stage to 100,100. All spectra types allow the `Integration Time` in seconds to be set and the `CCD Gain` used by the detector. Three gains are available `High Light`, `Best Dynamic Range`, and `High Sensitivity`. See the Synapse CCD manual for an explanation of these settings. All spectra types also allow for `Dark Current Subtraction` by checking the appropriate checkbox. When performing dark current

substration, a spectrum is taken with the spectrometer shutter closed and then subtracted from all subsequent spectra. All stored spectra have a `Name` and `Index`. The `Name` and `Index` are appended to one another to give the spectrum a name in the current project. The value of `Index` automatically increases after each spectra but can also be manually set to any value. Every spectrum setting tab also has a `Start` and `Stop` button. The `Start` button begins taking a spectrum of the type given by the tab name. The `Stop` button will stop a spectrum of any type. The current spectral acquisition must be completed before the stop occurs. If a long integration is underway it may take several seconds before the stop occurs. Additionally, when taking triggered spectra a final trigger must be processed after the `Stop` button is pressed.

Time spectra and triggered spectra have additional settings. A fixed `Number of Spectra` to acquire must be set, but the software can be set to `Continue Until Stop Pressed` by checking the appropriate checkbox. This prevents the software from stopping spectral acquisitions once the indicated `Number of Spectra` has been reached. Additionally an option can be set to `Enable Output Triggers` and send TTL pulses to the CCD outputs whenever a spectral acquisition begins.

Image spectra allow the size of the image map to be specified. `Center` position indicates the position of the center of the map. The `Range` is the width of map where the map runs from center-range/2 to center+range/2 on each axis. Be sure when specifying a range that absolute coordinates do not exceed the allowed 0-200 range. `Pixels` indicates the number of discrete steps taken by laser as it rasters over the sample surface.
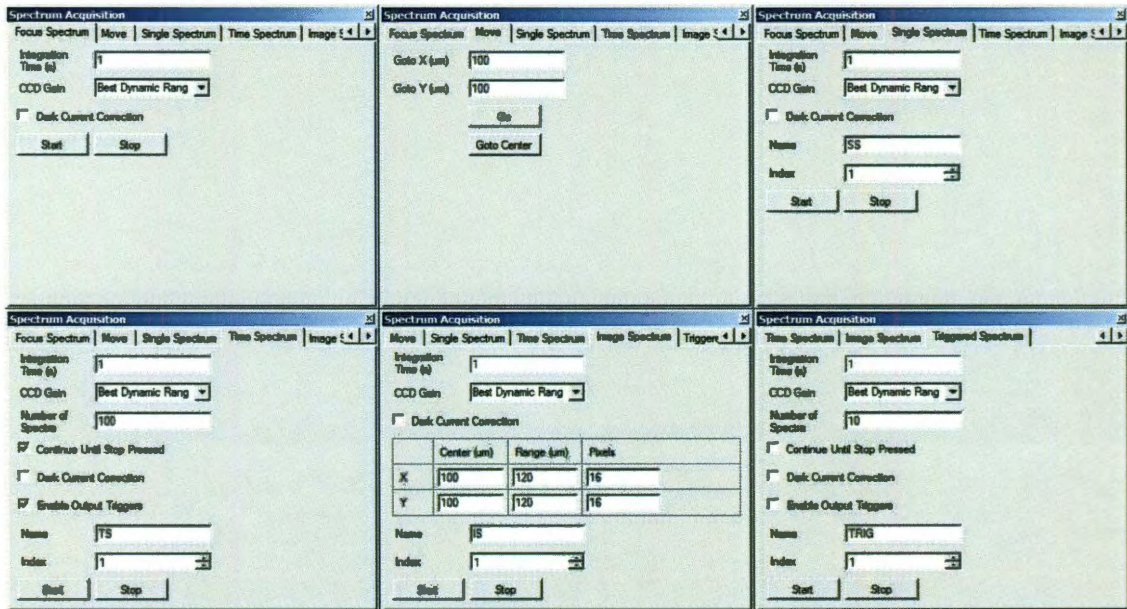
Figure A.9 : Spectrum acquisition settings shown tab by tab.

A.12   Spectrum Viewer

The hardware spectrum window and any open spectrum are displayed in a spectrum viewer (Fig. A.10). The hardware spectrum will always display the last spectral acquisition. The spectrum viewer allows the user to select a region of the spectrum to zoom in on and can also save an image of the spectrum. The X axis label indicates the units of the spectrum. When viewing time or triggered spectra the arrow keys allow the user to scroll through all the acquired spectra with the spectrum number currently being shown indicated in the window title. When viewing an intensity map and the spectrum of an image spectrum at the same time, clicking on a pixel of the intensity map will display the full spectrum in the spectrum viewer with the pixel coordinate (in pixels) displayed in the title.
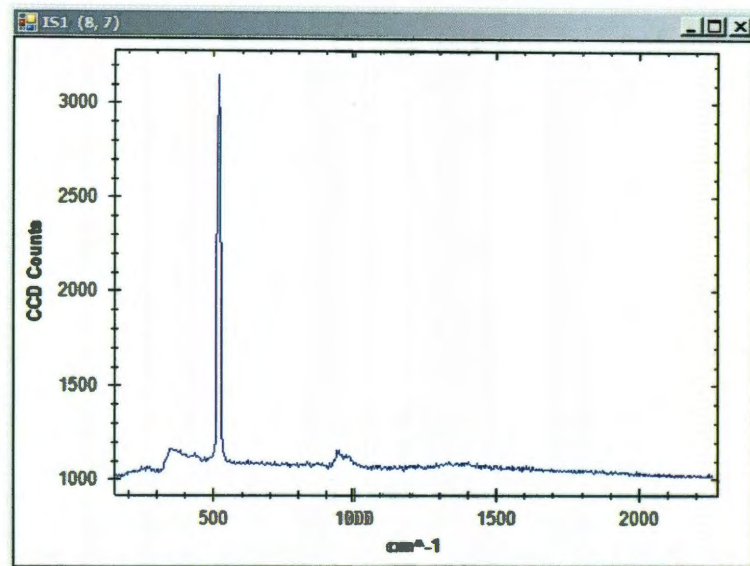
Figure A.10 : Spectrum viewer showing an image spectrum named IS1. The viewer is currently showing the spectrum at pixel (8,7).

A.13 Waterfall plot viewer

The waterfall plot viewer shows waterfall plots of time and triggered spectra. When first displayed the watefall viewer automatically shows the entire X axis and Y axis ranges and sets the color scaling to be from the lowest number of CCD counts to the highest. The X-Axis and Y-Axis boxes show the units of the related axis. The Min and Max range of the X and Y axes as well as the intensity can be changed by the user to better show the region of interest. The Auto buttons automatically rescale the axes to their full range. A waterfall plot can only show the data that was available when it was created. For instance if a waterfall plot of a time spectrum is created while the time spectrum is still being acquired it can only ever show the data up to the point when it was created. To see the newly acquired data a new waterfall plot must be made.
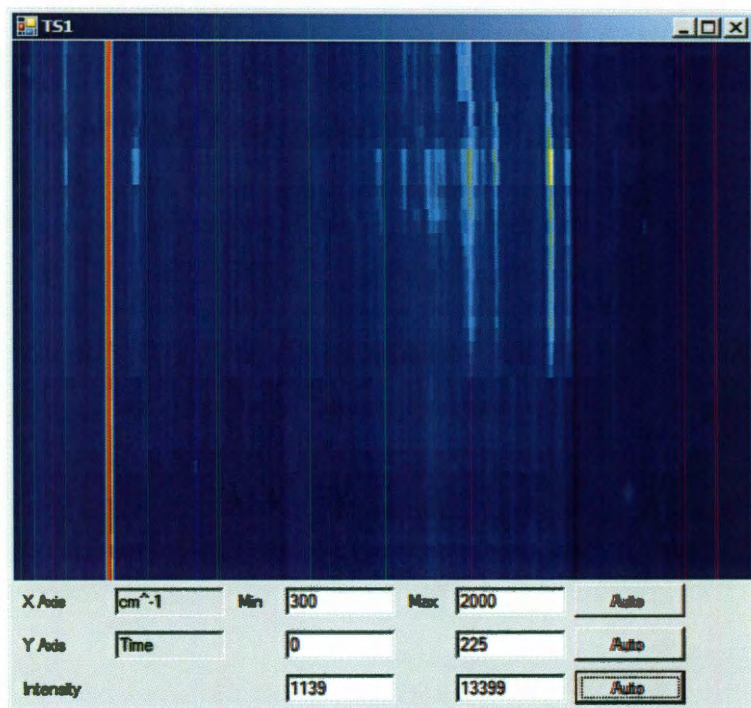
Figure A.11 : Waterfall plot viewer showing time spectrum **TS1**.
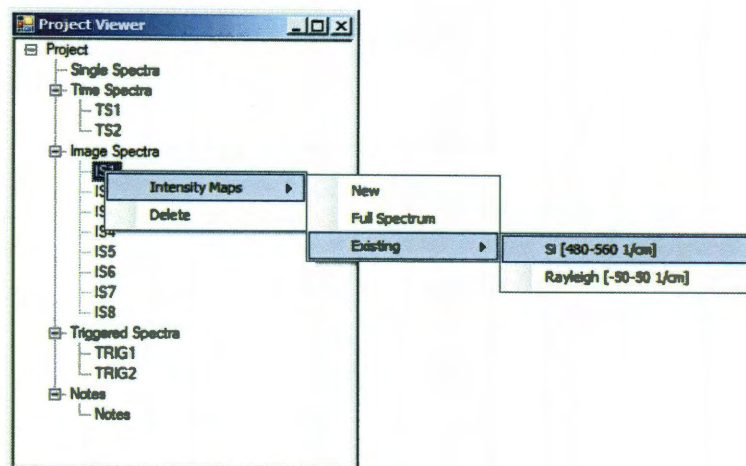
Figure A.12 : Intensity map menu in project viewer.

A.14 Intensity map viewer

The intensity map viewer displays an intensity map of an image map spectrum for a given filter. An intensity map maps out the intensity of a particular wavelength range as a function of position. The intensity for a given pixel is the integral of the start and stop wavelengths minus an optional background. Before viewing an intensity map, a filter must be selected. When you right click an image spectrum in the project viewer and select Intensity Maps you we see a submenu with three options: New, Full Spectrum, Existing (Fig. A.12). New allows you to create a new filter, Full Spectrum makes an intensity map which is a sum of the pixels in a spectrum, and Existing allows you to select a previously created filter. Filters for mapping the Si 520 cm^{-1} peak and Rayleigh line are always available from the existing menu. If you create a new filter is will then appear in the Existing menu for later use.

When creating a new filter the image spectrum filter form is displayed (Fig A.13). You can specify a Name for the filter so it is easy to find in the existing menu later.

Figure A.13 : Image spectrum filter form used to create a new filter.

You must specify the `Start Wavelength` and `Stop Wavelength` in whatever units the image map you will be taking will use. Finally you can specify how many pixels at the start and end of the spectrum to average for baseline subtraction (Called `Baseline Average Start` and `Baseline Average End`). The baseline subtraction takes the average value of the spectrum to the left (Start) and right (End) of the spectrum and then subtracts that amount from the entire spectrum. This is very useful if there is a fluorescent background you wish to exclude. If the number of pixels to use for baseline subtraction is zero then no background removal is done. This is useful if you want to map the intensity of background fluorescence.

Once a filter is created or selected, the intensity map viewer is displayed. It will continually update until the image spectrum is complete.

A.15   Accommodating changes to hardware

Should the need arise to replace some for the hardware of the Raman microscope, changes to the RM software may be necessary. If the computer has to be replaced it should be noted that there is conflict between the Jobin Yvon software and LabVIEW related the security key used by SynerJY (the Jobin Yvon spectrometer software).

To fix the problem a registry key change must be made. Two entries must be added or changed: set

`HKEY_LOCAL_MACHINE\SOFTWARE\National Instruments\Logos\`

`Ports\FirstClientPort` with a value of 8000 and set

`HKEY_LOCAL_MACHINE\SOFTWARE\National Instruments\Logos\`

`Ports\FirstServerPort` with a value of 7000.

If the CCD camera needs to be replaced the same brand should be used. The serial number needed to identify the camera in the RM software is hard coded in the Active-X control in `VideoForm`. You must update the serial number for the camera for it to work. Also it is likely RM will crash if the camera is not present.

If the Spectrograph or CCD detector need to be replaced with identical hardware there should not be a problem. If similar Jobin Yvon software is used minimal changes to `CCDController.cs` or `MonoController.cs` may be required.

If the piezo stage needs to be replaced any PI stage should work with few modifications. If the movement range of the stage is different than 200×200 μm the stage movement code will need to be updated. The relevent files would be `MainForm.cs` and `E454StageController.cs`.

A.16   Modifications to the Software

In general anyone familiar with C# should be able to modify RM without much trouble. Please note that spectral acquisitions are threaded so a basic understanding of threading and delegates is necessary to change the user interface. If new types of spectra are desired one should copy the threading procedure used for time spectra in `MainForm.cs`.

Bibliography

[1] H. Park, A. K. Lim, A. P. Alivisatos, J. Park, and P. L. McEuen, "Fabrication of metallic electrodes with nanometer separation by electromigration," *Appl. Phys. Lett.*, vol. 75, no. 2, pp. 301–3, 1999.

[2] H. Park, J. Park, A. K. L. Lim, E. H. Anderson, A. P. Alivisatos, and P. L. McEuen, "Nanomechanical oscillations in a single c_{60} transistor," *Nature*, vol. 407, pp. 57–60, 2000.

[3] L. H. Yu and D. Natelson, "The kondo effect in c60 single-molecule transistors," *Nano Lett.*, vol. 4, pp. 79–83, 2004.

[4] D. Natelson, L. H. Yu, J. W. Ciszek, Z. K. Keane, and J. M. Tour, "Single-molecule transistors: Electron transfer in the solid state," *Chem. Phys.*, vol. 324, pp. 267–275, 2006.

[5] D. R. Ward, N. K. Grady, C. S. Levin, N. J. Halas, Y. Wu, P. Nordlander, and D. Natelson, "Electromigrated nanoscale gaps for surface-enhanced raman spectroscopy.," *Nano Lett.*, vol. 7, pp. 1396–1400, May 2007.

[6] D. R. Ward, N. J. Halas, J. W. Ciszek, J. M. Tour, Y. Wu, P. Nordlander, and D. Natelson, "Simultaneous measurements of electronic conduction and raman response in molecular junctions.," *Nano Lett.*, vol. 8, pp. 919–924, Mar. 2008.

[7] D. R. Ward, D. A. Corely, J. M. Tour, and D. Natelson, "Vibrational and

electronic heating in molecular nanojunctions." 2010.

[8] D. R. Ward, J. C. Cuevas, F. Hüser, F. Pauly, and D. Natelson, "Optical rectification and field enhancement in a plasmonic nanogap," *Nature Nano.*, 2010.

[9] A. R. Champagne, A. N. Pasupathy, and D. C. Ralph, "Mechanically adjustable and electrically gated single-molecule transistors," *Nano Lett.*, vol. 5, pp. 305–308, 2005.

[10] L. Venkataraman, J. E. Klare, I. W. Tam, C. Nuckolls, M. S. Hybertsen, and M. L. Steigerwals, "Single-molecule circuits with well-defined molecular conductance," *Nano Lett.*, vol. 6, pp. 458–462, 2006.

[11] J. Park, A. N. Pasupathy, J. I. Goldsmith, C. Chang, Y. Yaish, J. R. Petta, M. Rinkowski, J. P. Sethna, H. D. Abru na, P. L. McEuen, and D. C. Ralph, "Coulomb blockade and the kondo effect in single-atom transistors," *Nature*, vol. 417, pp. 722–725, 2002.

[12] W. Liang, M. P. Shores, M. Bockrath, J. R. Long, and H. Park, "Kondo resonance in a single-molecule transistor," *Nature*, vol. 417, pp. 725–729, 2002.

[13] S. Kubatkin, A. Danilov, M. Hjort, J. Cornil, J.-L. Brédas, N. Stuhr-Hansen, P. Hedegård, and T. Bjørnholm, "Single-electron transistor of a single organic molecule with access to several redox states," *Nature*, vol. 425, pp. 698–701, 2003.

[14] A. N. Pasupathy, R. C. Bialczak, J. Martinek, J. E. Grose, L. A. K. Donev, P. L. McEuen, and D. C. Ralph, "The kondo effect in the presence of ferromagnetism," *Science*, vol. 306, pp. 86–89, 2004.

[15] L. H. Yu, K. Z. Keane, J. W. Ciszek, C. L., M. P. Stewart, J. M. Tour, and D. Natelson, "Inelastic electron tunneling via molecular vibrations in single-molecule transistors," *Phys. Rev. Lett.*, vol. 82, p. 266802, 2004.

[16] A. N. Pasupathy, J. Park, C. Chang, A. V. Soldatov, S. Lebedkin, R. C. Bialczak, J. E. Grose, L. A. K. Donev, J. P. Sethna, D. C. Ralph, and P. L. McEuen, "Vibration-assisted electron tunneling in c140 transistors," *Nano Lett.*, vol. 5, pp. 203–207, 2005.

[17] L. H. Yu, Z. K. Keane, J. W. Ciszek, L. Cheng, J. M. Tour, T. Baruah, M. R. Pederson, and D. Natelson, "Kondo resonances and anomalous gate dependence in the electrical conductivity of single-molecule transistors," *Phys. Rev. Lett.*, vol. 95, p. 256803, 2005.

[18] H. B. Heersche, d. Z. Groot, J. A. Folk, v. d. H. S. J. Zant, C. Romeike, M. R. Wegewijs, L. Zobbi, D. Barreca, E. Tondello, and A. Cornia, "Electron transport through single mn_{12} molecular magnets," *Phys. Rev. Lett.*, vol. 96, p. 206801, 2006.

[19] D.-H. Chae, J. F. Berry, S. Jung, F. A. Cotton, C. A. Murillo, and Z. Yao, "Vibrational excitations in single trimetal-molecule transistors," *Nano Lett.*, vol. 6, pp. 165–168, 2006.

[20] A. V. Danilov, S. E. Kubatkin, S. G. Kafanov, K. Flensberg, and T. Bjornholm, "Electron transfer dynamics of bistable single-molecule junctions," *Nano Lett.*, vol. 6, pp. 2184–2190, 2006.

[21] v. d. H. S. J. Zant, E. A. Osorio, M. Poot, and K. O'Neill, "Electromigrated molecular junctions," *Phys. Stat. Sol (B)*, vol. 243, pp. 3408–3412, 2006.

[22] A. V. Danilov, S. E. Kubatkin, S. G. Kafanov, P. Hedegård, N. Stuhr-Hansen, K. Moth-Poulsen, and T. Bjornholm, "Electronic transport in single molecule junctions: Control of the molecule-electrode coupling through intramolecular tunneling barriers," *Nano Lett.*, vol. 8, pp. 1–5, 2008.

[23] N. J. Tao, "Electron transport in molecular junctions," *Nature Nano.*, vol. 1, pp. 173–181, 2006.

[24] M. Galperin, M. A. Ratner, A. Nitzan, and A. Troisi, "Nuclear coupling and polarization in molecular transport junctions: Beyond tunneling to function," *Science*, vol. 319, pp. 1056–1060, 2008.

[25] J. M. Hollas, *Modern Spectroscopy*. Wiley, 2004.

[26] R. C. Maher, L. F. Cohen, J. C. Gallop, E. C. Le Ru, and P. G. Etchegoin, "Temperature-dependent anti-stokes/stokes ratios under surface-enhanced raman scattering conditions," *J. Phys. Chem. B*, vol. 110, pp. 6797–6803, 2006.

[27] S. Link and M. A. El-Sayed, "Size and temperature dependence of the plasmon absorption of colloidal gold nanoparticles," *J. Phys. Chem. B*, vol. 103, pp. 4212–4217, 1999.

[28] A. Otto, I. Mrozek, H. Grabhorn, and W. Akemann, "Surface enhanced raman scattering," *J. Phys. Condens. Matt.*, vol. 4, pp. 1143–1212, 1992.

[29] A. Hartstein, J. R. Kirtley, and J. C. Tsang, "Enhancement of the infrared absorption from molecular monolayers with thin metal overlayers," *Phys. Rev. Lett.*, vol. 45, pp. 201–204, 1980.

[30] E. Fort and S. Gresillon, "Surface enhanced fluorescence," *J. Phys. D. - Appl. Phys.*, vol. 41, p. 013001, 2008.

[31] P. B. Johnson and R. W. Christy, "Optical constants of the nobel metals," *Phys. Rev. B*, vol. 6, pp. 4370–4379, 1972.

[32] M. Fleischmann, P. J. Hendra, and A. J. McQuillan, "Raman spectra of pyridine absorbed at a silver electrode," *J. Chem. Phys. Lett.*, vol. 26, p. 163, 1974.

[33] D. L. Jeanmaire and R. P. V. Duyne, "Surface raman spectroelectrochemistry: Part i. heterocyclic, aromatic, and aliphatic amines adsorbed on the anodized silver electrode," *J. Electroanal. Chem.*, vol. 84, pp. 1–20, 1977.

[34] M. Moskovits, "Surface-enhanced raman spectroscopy: a brief retrospective," *J. Raman Spect.*, vol. 36, pp. 485–496, 2005.

[35] M. Osawa, N. Matsuda, K. Yoshii, and I. Uchida, "Charge transfer resonance raman process in surface-enhanced raman scattering from p-aminothiophenol adsorbed on silver: Herzberg-teller contribution," *J. Phys. Chem.*, vol. 98, pp. 12702–12707, 1994.

[36] J. R. Lombardi and R. L. Birke, "A unified approach to surface-enhanced raman spectroscopy," *J. Phys. Chem. C*, vol. 112, pp. 5605–5617, 2008.

[37] S. Buchanan, E. C. Le Ru, and P. G. Etchegoin, "Plasmon-dispersion corrections and constraints for surface selection rules of single molecule sers," *Phys. Chem. Chem. Phys.*, vol. 11, pp. 7406–7411, 2009.

[38] H.-B. Abel and F. Fischer, "The continuous background of sers from ag colloids in alkali halide crystals," *Phys. Stat. Sol. B*, vol. 167, pp. 741–751, 1991.

[39] S. Mahajan, R. M. Cole, J. D. Speed, S. H. Pelfrey, A. E. Russell, P. N. Bartlett, S. M. Barnett, and J. J. Baumberg, "Understanding the surface-enhanced raman spectroscopy "background"," *J. Phys. Chem. C*, vol. 114, pp. 7242–7250, 2010.

[40] S. Nie and S. R. Emory, "Probing single molecules and single nanoparticles by surface-enhanced raman scattering," *Science*, vol. 275, pp. 1102–1106, 1997.

[41] K. Kneipp, Y. Wang, H. Kneipp, L. T. Perelman, I. Itzkan, R. Dasari, and M. S. Feld, "Single molecule detection using surface-enhanced raman scattering (sers)," *Phys. Rev. Lett.*, vol. 78, pp. 1667–1670, 1997.

[42] H. Xu, E. J. Bjerneld, M. Käll, and L. Börjesson, "Spectroscopy of single hemoglobin molecules by surface enhanced raman scattering," *Phys. Rev. Lett.*, vol. 83, pp. 4357–4360, 1999.

[43] A. M. Michaels, J. Jiang, and L. Brus, "Ag nanocrystal junctions as the site for surface-enhanced raman scattering of single rhodamine 6g molecules," *J. Phys. Chem. B*, vol. 104, pp. 11965–11971, 2000.

[44] D. P. Fromm, A. Sundaramurthy, A. Kinkhabwala, P. J. Schuck, G. S. Kino, and W. E. Moerner, "Exploring the chemical enhancement for surface-enhanced raman scattering with au bowtie nanoantennas," *J. Chem. Phys.*, vol. 124, p. 061101, 2006.

[45] P. G. Etchegoin, E. C. Le Ru, M. Meyer, and K. Kneipp, "Sers assertions addressed," *Physics Today*, vol. 61, pp. 13–15, 2008.

[46] P. C. Andersen, M. L. Jacobson, and K. L. Rowlen, "Flashy silver nanoparticles," *J. Phys. Chem. B*, vol. 108, pp. 2148–2153, 2004.

[47] A. Otto, "What is observed in single molecule sers, and why?," *J. Raman Spectrosc.*, vol. 33, pp. 593–598, 2002.

[48] D. K. Lambert, "Stark effect of adsorbate vibrations," *Sol. State Comm.*, vol. 51, pp. 297–300, 1984.

[49] K. O'Neill, E. A. Osorio, and H. S. J. van der Zant, "Self-breaking in planar few-atom au constrictions for nanometer-spaced electrodes," *Appl. Phys. Lett.*, vol. 90, p. 133109, 2007.

[50] Z. Wang and L. J. Rothberg, "Origins of blinking in single-molecule raman spectroscopy," *J. Phys. Chem*, vol. 109, pp. 3387–3391, 2005.

[51] J. W. Ciszek, Z. K. Keane, L. Cheng, M. P. Stewart, L. H. Yu, D. Natelson, and J. M. Tour, "Neutral complexes of first row transition metals bearing unbound thiocyanates and their assembly on metallic surfaces," *J. Am. Chem. Soc.*, vol. 128, pp. 3179–3189, 2006.

[52] M. R. Beversluis, A. Bouhelier, and L. Novotny, "Continuum generation from single gold nanostructures through near-field mediated intraband transitions," *Phys. Rev. B*, vol. 68, p. 115433, 2003.

[53] A. Kudelski and B. Pettinger, "Sers on carbon chain segments: monitoring locally surface chemistry," *Chem. Phys. Lett.*, vol. 321, pp. 356–362, 2000.

[54] D. Richards, R. G. Milner, F. Huang, and F. Festy, "Tip-enhanced raman microscopy: practicalities and limitations," *J. Raman Spectrosc.*, vol. 34, pp. 663–667, 2003.

[55] P. J. Schuck, D. P. Fromm, A. Sundaramurthy, G. S. Kino, and W. E. Moerner, "Improving the mismatch between light and nanoscale objects with gold bowtie nanoantennas," *Phys. Rev. Lett.*, vol. 94, p. 017402, 2005.

[56] S. Lal, N. K. Grady, G. P. Goodrich, and N. J. Halas, "Profiling the near field of a plasmonic nanoparticle with raman-based molecular rulers," *Nano Lett.*, vol. 6, pp. 2338–2343, 2006.

[57] W. Cai, B. Ren, X. Q. Li, C. X. Shi, F. M. Liu, X. W. Cai, and Z. Q. Tian, "Investigation of surface-enhanced raman scattering from platinum electrodes using a confocal raman microscope: dependence of surface roughening pretreatment," *Surf. Sci.*, vol. 406, pp. 9–22, 1998.

[58] C. Oubre and P. Nordlander, "Finite-difference time-domain studies of the optical properties of nanoshell dimers," *J. Phys. Chem. B*, vol. 109, pp. 10042–10051, 2005.

[59] P. Nordlander and F. Le, "Plasmonic structure and electromagnetic field enhancements in the metallic nanoparticle-film system," *Appl. Phys. B*, vol. 84, pp. 35–41, 2006.

[60] B. H. Hamadani, D. A. Corley, J. W. Ciszek, J. M. Tour, and D. Natelson, "Controlling charge injection in organic field-effect transistors using self-assembled monolayers," *Nano Lett.*, vol. 6, pp. 1303–1306, 2006.

[61] D. R. Strachan, D. E. Smith, M. D. Fischbein, D. E. Johnston, B. S. Guiton, M. Drndi'c, D. A. Bonnell, and A. T. Johnson Jr., "Clean electromigrated nanogaps imaged by transmission electron microscopy," *Nano Lett.*, vol. 6, pp. 441–444, 2006.

[62] H. B. Heersche, G. Lientschnig, K. O'Neill, H. S. J. van der Zant, and H. Zand-bergen, "In situ imaging of electromigration-induced nanogap formation by transmission electron microscopy," *Appl. Phys. Lett.*, vol. 91, p. 072107, 2007.

[63] S. Y. Quek, L. Venkataraman, H. J. Choi, S. G. Louie, M. S. Hybertsen, and J. B. Neaton, "Amine-gold linked single-molecule circuits: Experiment and theory," *Nano Lett.*, vol. 7, pp. 3477–3482, 2007.

[64] A. M. Nowak and R. L. McCreery, "In situ raman spectroscopy of bias-induced structural changes in nitroazobenzene molecular electronic junctions," *J. Am. Chem. Soc.*, vol. 126, pp. 16621–16631, 2004.

[65] A. Jaiswal, K. G. Tavakoli, and S. Zou, "Coupled surface-enhanced raman spectroscopy and electrical conductivity measurements of 1, 4-phenylene diiso-cyanide in molecular electronic junctions," *Anal. Chem.*, vol. 78, pp. 120–124, 2006.

[66] T. Taychatanapat, K. Bolotin, F. Kuemmeth, and D. C. Ralph, "Imaging electromigration during the formation of break junctions," *Nano Lett.*, vol. 7, pp. 652–656, 2007.

[67] T. Brintlinger, Y. Qi, K. Baloch, D. Goldhaber-Gordon, and J. Cumings, "Electron thermal microscopy," *Nano Lett.*, vol. 8, p. 582, 2008.

[68] S. B. Ippolito, S. A. Thorne, M. G. Eraslan, B. B. Goldberg, M. S. Unlu, and Y. Leblebici, "High spatial resolution subsurface thermal emission microscopy," *Appl. Phys. Lett.*, vol. 84, p. 4529, 2004.

[69] S. Dhokkar, B. Serio, P. Lagonotte, and P. Meyruis, "Power transistor near-

infrared microthermography using an intensified ccd camera and frame integration," *Meas. Sci. Technol.*, vol. 18, p. 2696, 2007.

[70] S. Ingvarsson, L. J. Klein, Y.-Y. Au, J. A. Lacey, and H. F. Hamann, "Enhanced thermal emission from individual antenna-like nanoheaters," *Opt. Express*, vol. 15, p. 11249, 2007.

[71] L. J. Klein, H. F. Hamann, Y.-Y. Au, and S. Ingvarsson, "Coherence properties of infrared thermal emission from heated metallic nanowires," *Appl. Phys. Lett.*, vol. 92, p. 213102, 2008.

[72] A. Fursina, S. Lee, R. G. S. Sofin, I. V. Shvets, and N. D., "Nanogaps with very large aspect ratios for electrical measurements," *App. Phys. Lett*, vol. 92, p. 113102, 2008.

[73] D. R. Ward, G. D. Scott, Z. K. Keane, N. J. Halas, and D. Natelson, "Electronic and optical properties of electromigrated molecular junctions," *J. Phys. Condens. Matt.*, vol. 20, p. 374118, Sept. 2008.

[74] J. Jiang, K. Bosnick, M. Maillard, and L. Brus, "Single molecule raman spectroscopy at the junctions of large ag nanocrystals," *J. Phys. Chem. B*, vol. 107, pp. 9964–9972, 2003.

[75] K. Li, M. I. Stockman, and D. J. Bergman, "Self-similar chain of metal nanospheres as an efficient nanolens," *Phys. Rev. Lett.*, vol. 91, p. 227402, 2003.

[76] P. H. Cutler, T. E. Feuchtwang, T. T. Tsong, Y. Kuk, H. Nguyen, and L. A. A., "Proposed use of a scanning-tunneling-microscope tunnel junction for the measurement of a tunneling time," *Phys. Rev. B*, vol. 35, pp. 7774–7775, 1987.

[77] H. Q. Nguyen, P. H. Cutler, T. E. Feuchtwang, Z.-H. Huang, Y. Kuk, P. J. Silverman, A. A. Lucas, and T. E. Sullivan, "Mechanisms of current rectification in an stm tunnel junction and the measurement of an operational tunneling time," *IEEE Trans. Elect. Dev.*, vol. 36, p. 2671, 1989.

[78] A. V. Bragas, S. M. Landi, and O. E. Martínez, "Laser field enhancement at the scanning tunneling microscope junction measured by optical rectification," *Appl. Phys. Lett.*, vol. 72, pp. 2075–2077, 1998.

[79] X. W. Tu, J. H. Lee, and W. Ho, "Atomic-scale rectification at microwave frequency," *J. Chem. Phys.*, vol. 124, p. 021105, 2006.

[80] J. K. Viljas and J. C. Cuevas, "Role of electronic structure in photoassisted transport through atomic-sized contacts," *Phys. Rev. B*, vol. 75, p. 075406, 2007.

[81] D. C. Guhr, D. Rettinger, J. Boneberg, A. Erbe, P. Leiderer, and E. Scheer, "Influence of laser light on electronic transport through atomic-size contacts," *Phys. Rev. Lett.*, vol. 99, p. 086801, 2007.

[82] N. Ittah, G. Noy, I. Yutsis, and Y. Selzer, "Measurement of electronic transport through 1 g_0 gold contacts under laser irradiation," *Nano Lett.*, vol. 9, pp. 1615–1620, 2009.

[83] P. K. Tien and J. P. Gordon, "Multiphoton process observed in the interaction of microwave fields with the tunneling between superconductor films," *Phys. Rev.*, vol. 129, pp. 647–651, 1963.

[84] F. Pauly, J. K. Viljas, U. Huniar, M. Häfner, S. Wohlthat, M. Bürkle, J. C. Cuevas, and G. Schön, "Cluster-based density-functional approach to quan-

tum transport through molecular and atomic contacts," *New J. Phys.*, vol. 10, p. 125019, 2008.

[85] J. Zuloaga, E. Prodan, and P. Nordlander, "Quantum description of the plasmon resonances of a nanoparticle dimer," *Nano Letters*, vol. 9, pp. 887–891, 2009.

[86] L. Mao, Z. Li, B. Wu, and H. Xu, "Effects of quantum tunneling in metal nanogap on surface-enhanced raman scattering," *Appl. Phys. Lett.*, vol. 94, p. 243102, 2009.

[87] Y.-C. Chen, M. Zwolak, and M. Di Ventra, "Local heating in nanoscale conductors," *Nano Lett.*, vol. 3, pp. 1691–1694, 2003.

[88] M. Galperin and A. Nitzan, "Current-induced light emission and light-induced current in molecular-tunneling junctions," *Phys. Rev. Lett.*, vol. 95, p. 206802, 2005.

[89] R. D'Agosta, N. Sai, and M. Di Ventra, "Local electron heating in nanoscale conductors," *Nano Lett.*, vol. 6, pp. 2935–2938, 2006.

[90] A. Pecchia, G. Romano, and A. Di Carlo, "Theory of heat dissipation in molecular electronics," *Phys. Rev. B*, vol. 75, p. 035401, 2007.

[91] Z. Huang, F. Chen, R. D'Agosta, P. A. Bennett, M. Di Ventra, and N. J. Tao, "Local ionic and electron heating in single-molecule junctions," *Nature Nano.*, vol. 2, pp. 698–703, 2007.

[92] M. Galperin, A. Nitzan, and M. R. Ratner, "Heat conduction in molecular transport junctions," *Phys. Rev. B*, vol. 75, p. 155312, 2007.

[93] Z. Ioffe, T. Shamai, A. Ophir, G. Noy, I. Yutsis, K. Kfir, O. Cheshnovsky, and Y. Selzer, "Detection of heating in current-carrying molecular junctions by raman scattering," *Nature Nano.*, vol. 3, pp. 727–732, 2008.

[94] C. M. Galloway, E. C. Le Ru, and P. G. Etchegoin, "Single-molecule vibrational pumping in sers," *Phys. Chem. Chem. Phys.*, vol. 11, pp. 7372–7380, 2009.

[95] A. Otto, W. Akemann, and A. Pucci, "Normal bands in surface-enhanced raman scattering (sers) and their relation to the electron-hole pair excitation background in sers," *Isr. J. Chem.*, vol. 46, pp. 307–315, 2006.

[96] S. Datta, *Electronic Transport in Mesoscopic Systems.* Cambrige, 1995.

[97] B. C. Stipe, M. A. Rezaei, and W. Ho, "Single-molecule vibrational spectroscopy and microscopy," *Science*, vol. 280, pp. 1732–1735, 1998.

[98] M. Galperin, M. A. Ratner, and A. Nitzan, "Raman scattering from nonequilibrium molecular conduction junctions," *Nano Lett.*, vol. 9, pp. 758–762, 2009.

[99] R. H. M. Smit, C. Untiedt, and J. M. van Ruitenbeek, "The high-bias stability of monatomic chains," *Nanotechnology*, vol. 15, pp. S472–S478, 2004.

[100] M. Tsutsui, M. Taniguchi, and T. Kawai, "Local heating in metal-molecule-metal junctions," *Nano Lett.*, vol. 8, pp. 3293–3297, 2008.

[101] M. Oron-Carl and R. Krupke, "Raman spectroscopic evidence for hot-phonon generation in electrically biased carbon nanotubes," *Phys. Rev. Lett.*, vol. 100, p. 127401, 2008.

[102] S. Berciaud, M. Y. Han, L. E. Brus, P. Kim, and T. F. Heinz, "Electron and optical phonon temperatures in electrically biased graphene," *Phys. Rev. Lett.*,

vol. 104, p. 227401, 2010.

[103] A. Zawadowski and M. Cardona, "Theory of raman scattering on normal metals with impurities," *Phys. Rev. B*, vol. 42, pp. 10732–10734, 1990.

[104] O. Tal, M. Kiguchi, W. H. A. Thijssen, D. Djukic, C. Untiedt, R. H. M. Smit, and J. M. van Ruitenbeek, "Molecular signature of highly conductive metal-molecule-metal junctions," *Phys. Rev. B*, vol. 80, p. 085427, 2009.

[105] M. Galperin, A. Nitzan, M. A. Ratner, and D. R. Stewart, "Molecular transport junctions: asymmetry in inelastic tunneling processes," *J. Phys. Chem B*, vol. 109, pp. 8519–8522, 2005.

[106] M. Galperin, A. Nitzan, and M. A. Ratner, "Heat conduction in molecular transport junctions," *Phys. Rev. B*, vol. 75, p. 155312, 2008.

[107] L. Zhang, S. Aite, and Z. Yu, "Unique laser-scanning optical microscope for low-temperature imaging and spectroscopy," *Rev. Sci. Instrum.*, vol. 78, p. 083701, 2007.